Zeitschrift: Helvetica Physica Acta

Band: 61 (1988)

Heft: 6

Vereinsnachrichten: Rapport de la réunion de printemps de la Société Suisse de Physique des 28 et 29 mars 1988 à Windisch

Autor: [s.n.]

Helvetica Physica Acta
Vol. 61 (1988)

0018-0238/88/060801-16$1.50+0.20/0

CELLULAR AUTOMATA APPROACH TO PHYSICAL PROBLEMS

M. Droz* et B. Chopard
Département de Physique Théorique
Université de Genève
CH-1211 Genève 4, Switzerland

Abstract

The main applications of cellular automata (C.A) in physical problems are briefly reviewed. After having defined what a C.A is, some considerations on the motivations to use C.A in physics are given. Several examples of their applications in the fields of hydrodynamics, equilibrium statistical mechanics of systems on a lattice, growth mechanisms, diffusion processes, pattern recognition, models of memory and deterministic dynamics are given. An explicit application to a model of nonequilibruim phase transition is considered in more details. It is shown how the C.A rules are constructed, how to define analytically a mean field approximation for the automaton and how the results of this mean field approximation compare with the exact numerical solution of the model. Finally some general remarks on the prospects and open problems in the field are made.

1. Introduction

Cellular automata (C.A) were introduced in the late forties by J. von Neumann [1] in order to provide a model for the behaviour of complex extended systems. His main interest was in fact to give a reductionistic approach to biological problems. The physicists community was introduced to the C.A through J. Conway's game of "life" [2]. As a result, C.A have been mainly considered as an amusing toy for twenty five years. With the earlier works of S. Wolfram [3] on statistical properties of one dimensional C.A this misleading picture did not change too much; C.A becames a way to get nice drawings. However in the meantime, several interesting developments occured, both theoretically and technically, making C.A an interesting tool to physicists.

---

* Invited talk given at the Spring Meeting of the Swiss Physical Society, Windisch, March 1988
Partially supported by the Swiss National Foundation for Scientific Research

The purpose of this paper is to show that C.A provide indeed an interesting approach to physical problems.

This paper is organized as follows. In Section 2, the definition of a C.A is given with some of its properties. In Section 3, the motivations to use C.A are discussed. In Section 4 several problems for which C.A have been usefully applied are briefly reviewed. Some illustrative examples are discussed in more details. In Section 5, a C.A model of nonequilibruim phase transition is considered and used to illustrate what can be done to solve such a model. A mean field like approximation is derived analytically and its predictions compared with the results of a numerical simulation solving the problem exactly. Conclusions are given in Section 6.

2. Definition of a C.A

Cellular automata have five fundamental defining characteristics [4]:

1. They consist of a discrete lattice of sites.
2. They evolve in discrete time steps.
3. Each site takes on a finite set of possible values.
4. The value of each site evolves according to the same deterministic rule.
5. The rules for the evolution of a site depend only on a local neighbourhood of sites around it.

The condition number 4 can be generalized by allowing probabilistic rule. One then speaks of probabilistic C.A.

Moreover, C.A have the following properties:

-All the sites update their new state simultaneously.
-A cellular automaton is nothing but an array-processor with a few bit rather than a whole floating point variable at each site.
-The results of the computation are exact. There are no rounding approximations.

3. Motivations

In this section, we would like to discuss the motivations to use C.A in physics. Physicists often describe the phenomena they are interested in by (partial, nonlinear) differential equations for time and space dependant fields. Two typical situations can be distinguished. In the first one, the field equation describes a physical process at a

microscopic scale (for example the Schrödinger equation for a particule). In the second one, the differential equation is a coarse-grained description of microscopic processes which can have a discrete character, or can be easily modelized in terms of discrete variables.

The two above situations have something in common. Due to the intrinsic complexity of the differential equations or due to the particular boundaries conditions, one is very often not able to solve the equations analytically and one has to solve them numerically. In order to do that, one artificially discretize the problem by introducing a grid and by replacing the differential operators by their finite difference expressions. Thus, one does not solve anymore the continuous field equations but only a discrete version of them. The continuous solution is obtained by extrapolating the discrete solution between the points of the grid. Moreover, it could be very difficult to control the rounding errors introduced.

In view of the above remarks, it is legitimate to ask if it would not be better to start directely with an discretized model. The C.A approach try to perform this program. Note that several microscopic discretized models could reproduce similar coarse-grained equations. One would then choose the simplest model reproducing the desired macroscopic behaviour. This aspect of "two levels of reality" [6] will be now illustrated on an example.

An example: Fluid dynamics

At the macroscopic level, the fluid is described by a nonlinear partial differential equation for the velocity field (Navier-Stokes equation).

$$\partial_t \vec{u} + [\vec{u} \cdot \nabla \vec{u}] = -\frac{1}{\rho} \cdot \nabla p + \nu \triangle \vec{u} + [\zeta + \frac{\eta}{3}] \nabla \nabla \vec{u}$$

This equation is difficult to solve due to: its nonlinear character, the possibles instabilities and the boundaries conditions (even in the "linear approximation" it is usually impossible to have an analytic solution).

At the microscopic level, the system is described by the Hamilton's equations for N interacting particles. The dynamics is reversible. The properties of the fluid can be obtained by integrating (numerically) the equations of motion. The so-called "molecular dynamics" method performs this program. The difficulties are then the following:
-The dynamics is complicated: at most a few thousands particles can be study.
-This takes a very long computing time,even on a mainframe.

We can then ask ourselves how important are the "details" of the microscopic model in order to reproduce a correct macroscopic behaviour? Otherwise stated, is it possible to define a "fictitious microscopic model" such that:

-It has an as simple as possible microscopic dynamics (not necessarily Hamiltonian).
-It reproduces the Navier-Stokes equation at the macroscopic level.
-It leads to very fast numerical algorithms which are easily implementable (boundary conditions,...).

We shall now show how such a program can be realized in the case of a two dimensional fluid by reviewing briefly the so-called HPP Model (Hardi, Pomeau, Pazzis) [7]. The characteristics of this model are the following:

-The particles (mass m=1), move on a square lattice.
-They have a velocity v=1 pointing towards one of the four directions imposed by the lattice.
-The time is discretized and during one time unit, the particles travel one lattice constant.
-It is forbidden to have simultaneously two or more particles at a given site travelling in the same direction.
-Only two-particle collisions are allowed according to the rules given on the Fig 1.

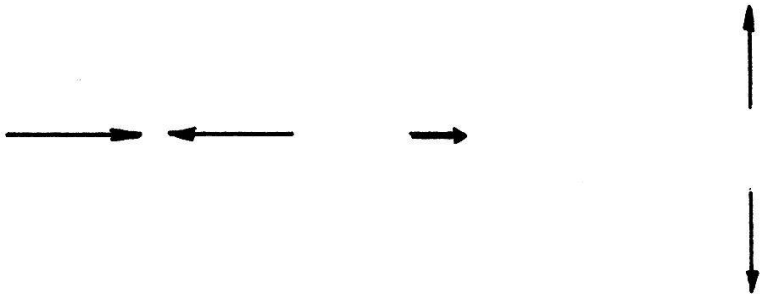

Note that the particle number, the impulsion and the energy are conserved during the collisions. Moreover, the dynamics is reversible. The microscopic dynamics being defined, one can now derive the macroscopic hydrodynamical equations. They are obtained by using the usual procedure of nonequilibrium statistical mechanics, i.e by deriving and solving the Boltzmann's equation and then deriving the hydrodynamical equations [9]. It turns out that this simple model has some pathologies, namely, the impulsion tensor is anisotropic and spurious conservation laws are introduced. However, these drawbacks can be cured by working on a hexagonal lattice (FHP model [9]) and by adding three particle collisions to remove the spurious conservation laws. Boundaries conditions can be taken care of very easily by changing the rules at the boundaries.

Thus, one sees that starting with a very simple microscopic dynamics, one can reproduces, (in the limit of small Mach numbers), the Navier-Stokes equation at the macroscopic scale [10].

The approach used in the above example, to simulate a differential equation by a set of C.A rules can be applied to many physical problems and several other examples will be described in the following sections.

4. Some applications of C.A to physical problems.

The goal of this section is not to give an exhaustive list of all the applications of the C.A to physical problems but rather to concentrate on some of the most significative ones.

a). Hydrodynamics: this is one of the most succesful application. The basic ideas have been given in section 3 for the so-called HPP or FHP models. Several extensions of these models have been made allowing to study flows at higher Reynolds numbers both in two and three dimensions [10]. Multi-speed models have been considered [8,11], in order to introduce thermal effects. Properties of a nonequilibrium fluids and, in particular, the nonequilibrium correlation functions were measured [12]. Modelizations of problems of magnetohydrodynamic have been also proposed [13, 14]. A critical discussion of the advantages and inconvenient of this approach relatively to the traditional one is given by Orsag et al. [15].

b). Equilibrium lattice models: there is a general equivalence between d-dimensional probabilistic cellular automata (P.C.A) and $(d+1)$-dimensional spin models on a lattice. The idea behind this equivalence is the following. One considers the successive states of the d-dimensional P.C.A as the successive layers of a $(d+1)$ dimensional lattice, the $(d+1)^{th}$ dimension being the time. The local character (in space and time) of the rule of the C.A allows to define a local hamiltonian on this new lattice. The probability measure over the space-time histories of the P.C.A can be seen as the Boltzmann weight of the equilibrium spin model. The formal equivalence between these two systems has been studied in details by Rujan [16] and Georges et al. [17]; the equivalences are given in Table 1. Note that for a given P.C.A, the corresponding spin system will generally have multi-spin terms and that the coupling constants will not be independent but constrained by some relations. The deterministic limit of a P.C.A is of particular interest in the sense that it corresponds to the zero temperature limit of the spin model [17]. Thus each particular time evolution of a deterministic C.A corresponds to a different ground-state of the spin model. For example, the ground-states of a two-dimensional triangular Ising model (a fully frustrated system) can be found with an appropriated P.C.A [16].

c). Growth mechanisms: several types of growth mechanisms can be simulated using C.A. A first class concerns the growth mechanisms driven by surface tension . A typical example is the spinodale decomposition [18]. One quenches a system below its coexistence curve and looks how the unstable state evolves towards equilibrium. In the late stage regime and for an evolution which does not conserve the order parameter , the dynamics of the interfaces between the different phases is driven by the local curvature of the "droplets". The "droplets" tend to become flatter (Allen-Cahn) [18].

Table 1.

D-DIMENSIONAL PCA	(D+1)-DIMENSIONAL SPIN MODEL
-Space-time configurations $[s_{i,t}]$	-Spin configurations $[s_{i,t}]$
-Local conditional probability: $P[\{s'_{t+1}\};\{s_t\}]$	-Normalised Boltzmann weight: $\lambda^{-1}W[\{s'\};\{s\}]$
- Normalisation condition : $\sum_{\{s'\}} P\left(\{s'\};\{s\}\right) = 1$	- "Disorder condition " on coupling constants $\sum_{\{s'\}} W\left(\{s'\};\{s\}\right) = \lambda$ independent of s
- Evolution operator	- Row-to-row transfer matrix
- Initial configuration	-Boundary conditions
- Probability for a history $P[\{s_{i,t}\}]$	-Gibbs weight $Z^{-1}exp-\beta H(s_{i,t})$
-Average over histories	-Thermodynamical average
-Transient phenomena	-Surface effects
-Deterministic limits	-Zero temperature limits
-Deterministic histories	-Ground states

In a cellular automata approach, each cell has two possible states corresponding to the two equilibrium phases. The evolution rule [19] is such that each cell "feels" the curvature in its vicinity. "Bays" are filled and "capes" are eroded. On the macroscopic scale, the detailed mechanims is blurred away and one gets a good model of growth driven by surface tension.

Another type of growth mecanisms to which C.A has been applied is the kinetic of the austenitic-martensitic transformation in alloys [20]. At high temperature the alloy is in an austenitic phase and, below the transition temperature, different variants of the new martensitic phase develop. An typical pattern is made of several needles each of them being constituted by a different variant. This pattern growths until a metastable state, with very long lifetime, is reached. On heating up the alloy, one observes an important hysteresis; the austenitic phase is recovered at a higher transition temperature. The C.A simulation reproduces qualitatively well all the features observed at a mesoscopic or macroscopic scale.

Finally, C.A can be used to simulate several kinetic growth processes like diffusion limited agregation for example.

d). **Diffusion processes:** simple C.A algorithms can be devised to simulate the Brownian motion of particles and thus the process of normal diffusion. This approach allows also to study the fractal properties of the "diffusion front" [21]. Generalization of the above rules to the case of diffusion in an inhomogeneous medium can be made [22] and allows the study of the anomalous diffusion.

e). **Pattern recognition:** C.A approach is well suited to the problem of pattern recognition [23, 24, 25]. Indeed, it is easy to digitalized a picture on a lattice. The states of the cells describe the colors of the cell or the "degrees of gray" in a black and white picture. Several algorithms can be devised to perform different operations such as "noise cleaning", skeletonization, or pattern finding and counting. Such algorithms are widely used in differents fields [23]. For example, in biomedical imagery, one is interested in the identification and counting of particular nuclei in pictures of tissue sections.

f). **Models of memory:** in the rapidly expending field of neural networks [26], new models of learning and retrieval algorithms based on an automata-like structure have been proposed recently (see [27] for a review). These models differs from the "free energy landscape" ones in many respects. In the automata-like models, learning is understood as a time dependant process.

g). **Deterministic dynamics:** numerical simulation of spin systems on a lattice is a widely used tool to investigate various problems in equilibrium or nonequilibrium statistical mechanics. The traditional method used for these simulations is the canonical Monte-Carlo method [28]. The evolution of the system is given by an appropriated master equation ensuring that, in the infinite time limit, the desired equilibrium state will be reached by the system. In the simulation of this stochastic dynamics one shoud use random numbers generator; the spins can be updated in a sequential or parallel way. A so-called microcanonical Monte-Carlo method has be proposed recently [29,30].

One considers a deteministic evolution at fixed energy. This evolution can be written in the form of C.A rules. It turns out that this is the fastest method available to simulate spin systems. For example, this method allows to update 6.7 10^8 Ising spin per second on a CRAY XMP computer [31].

5. Model of nonequilibrium phase transition.

The purpose of this section is to show on a realistic problem how one constructs the C.A rules and what can be done once the rules are given. A mean field like approximation will be discussed and its predictions compared with the exact numerical results for the model.

a). The Model.

The surface reaction model that we consider is similar to the one proposed recently by Ziff et al. [32]. Differences between the two models will show up through the modelization in terms of C.A. These reaction models are based upon some of the known steps of the reaction $A - B_2$ on a catalyst surface (for example $CO - O_2$). The basic steps in heterogeneous catalysis are the following :
i) A gas mixture with concentrations X_{B_2} of B_2 and $X_A = (1 - X_{B_2})$ of A sits above the surface and can be adsorbed. The surface can be divided in elementary cells. Each cell can absorb one atom only.
ii) The B species can only be adsorbed in the atomic form. A molecule B_2 approaching an empty cell will be dissociated into two B atoms only if another cell adjacent to the first one is empty. The two first steps correspond to the reactions

$$A \rightarrow A(\text{ads}) \quad B_2 \rightarrow 2B(\text{ads})$$

iii) If two nearest neighbour cells are occupied by different species they chemically react according to the reaction

$$A(\text{ads}) + B(\text{ads}) \rightarrow AB$$

and the product of the reaction is desorbed. This final desorption step is necessary for the product to be recovered and for the catalyst to be regenerated. However, the gas above the surface is assumed to be continually replenished by fresh material. Thus its composition is constant during the whole evolution.

Note that this model neglects several features which may be present in a real situation (see Chopard and Droz [33] for a more detailed discussion).

b). Cellular automata modelization.

In view of the above description, it seems natural to represent the problem in term of a two-dimensional cellular automaton.

The cells of the automaton correspond to the elementary cells of the catalyst. Each cell j can be in four different states $|\psi_j\rangle = |0\rangle$, $|A\rangle$, $|B\rangle$ or $|C\rangle$.

$|0\rangle$ corresponds to an empty cell, $|A\rangle$ to a cell occupied by an atom A, $|B\rangle$ to a cell occupied by an atom B. The state $|C\rangle$ describes the conditional occupation of the cell by an atom B. Conditional means that during the next evolution step of the automaton, $|C\rangle$ will become $|B\rangle$ or $|0\rangle$ depending upon the fact that a nearest neighbour cell is empty and ready to receive the second B atom of the molecule B_2. This conditional state is necessary to describe the dissociation of the B_2 molecules on the surface.

The time evolution of the CA is given by the following set of rules, fixing the state of the cell j at time $t+1$, $|\psi_j\rangle(t+1)$, as a function of the state of the cell j and its nearest neighbors (Von Neumann neighborhood) at time t :

R1 : If $|\psi_j\rangle(t) = |0\rangle$ then

$$|\psi_j\rangle(t+1) = \begin{cases} |A\rangle & \text{with probability } X_A \\ |C\rangle & \text{with probability } (1 - X_A) \end{cases}$$

R2 : If $|\psi_j\rangle(t) = |A\rangle$ then

$$|\psi_j\rangle(t+1) = \begin{cases} |0\rangle & \text{if at least one of the nearest neighbour cell} \\ & \text{of } j \text{ was in the state } |B\rangle \text{ at time } t \\ |A\rangle & \text{otherwise} \end{cases}$$

R3 : If $|\psi_j\rangle(t) = |B\rangle$ then

$$|\psi_j\rangle(t+1) = \begin{cases} |0\rangle & \text{if at least one of the nearest neighbour cell} \\ & \text{of } j \text{ was in the state } |A\rangle \text{ at time } t \\ |B\rangle & \text{otherwise} \end{cases}$$

R4 : If $|\psi_j\rangle(t) = |C\rangle$ then

$$|\psi_j\rangle(t+1) = \begin{cases} |0\rangle & \text{if none of the nearest neighbors was} \\ & \text{in the state } |C\rangle \text{ at time } t \\ |B\rangle & \text{otherwise} \end{cases}$$

This rule expresses the fact that the atoms of B_2 can be adsorbed only if they had been dissociated on two adjacent cells, that is if at least two adjacent cells were empty at time $t-1$.

Rules R1, R4 describe the adsorbtion-dissociation mechanism while rules R2, R3 describe the reaction desorption process. As discussed by Chopard and Droz [33] the

above rules do not reproduced exactly the physics described above but retain the main features.

As a function of the concentration X_A of the gas, different stationary states of the catalysis surface can be foreseen. If X_A is large the surface will completely be covered by the A atoms after some time. The small fraction of B atoms originally adsorbed will rapidly be eliminated through the desorption of AB. The stationary state will consist of a "poisoned" surface with pure A. If X_A is small we have the opposite situation and the stationary state will be "poisoned" with pure B. Obviously, once the surface is poisoned by a species, the reaction rate for the creation of AB is zero.

For an intermediate value of X_A, a more interesting situation can occur in which the stationary state is a mixed state composed of a fraction X_A^a of atoms A, a fraction X_B^a of atoms B and a fraction X_o^a of empty cells. The adsorption-dissociation mechanism compensates for the desorption process. The reaction rate is obviously finite in this intermediate region.

It is obviously very difficult to solve this model analytically. The only hope is to treat the problem in some approximation.

c). Mean field like approximation.

In the mean field approach, one attaches to a given cell at a given time a set of probabilities p_A, p_B, p_C and p_0 describing the probabilities that the cell is respectively in the states $|A\rangle$,$|B\rangle$, $|C\rangle$ or $|0\rangle$. Otherwise stated, after each evolution step, the automaton is "stirred" in such a way that the particular configuration is forgotten and replaced by an averaged configuration. The rules of the C.A lead to the following evolution rules for these probabilities:

$$p_A(t+1) = X_A p_0(t) + p_A(t)[1 - p_B(t)]^4$$

$$p_B(t+1) = p_B(t)[1 - p_A(t)]^4 + p_C(t)[1 - (1 - p_C(t))^4]$$

$$p_C(t+1) = p_0(t)(1 - X_A)$$

$$p_0(t+1) = p_A(t)[1 - (1 - p_B(t))^4] + p_B(t)[1 - (1 - p_A(t))^4] + p_C(t)[1 - p_C(t)]^4$$

In order to find the stationary states, one searches the fixed points of this set of equations. The resulting phase diagram is shown on figure 1. At $X_{A1} = 0.548$, one finds a first order phase transition. This transition can be called first order because the quantity $\psi_1 \equiv X_A^a(X_{A1}) - X_A^a(X_A)$, which can be taken as the order parameters, is discontinuous at the transition. At $X_A = 0$, one finds a second order phase transition, X^a increasing smoothly with X_A^a. However, in the domain $0.48 \leq c \leq 0.548$, one does not have a fixed point, but rather a limit cycle. This fact is depicted by a dotted line

on the phase diagram of the C.A. These results could be compared to the ones obtained by solving exactely the model on a special C.A machine.

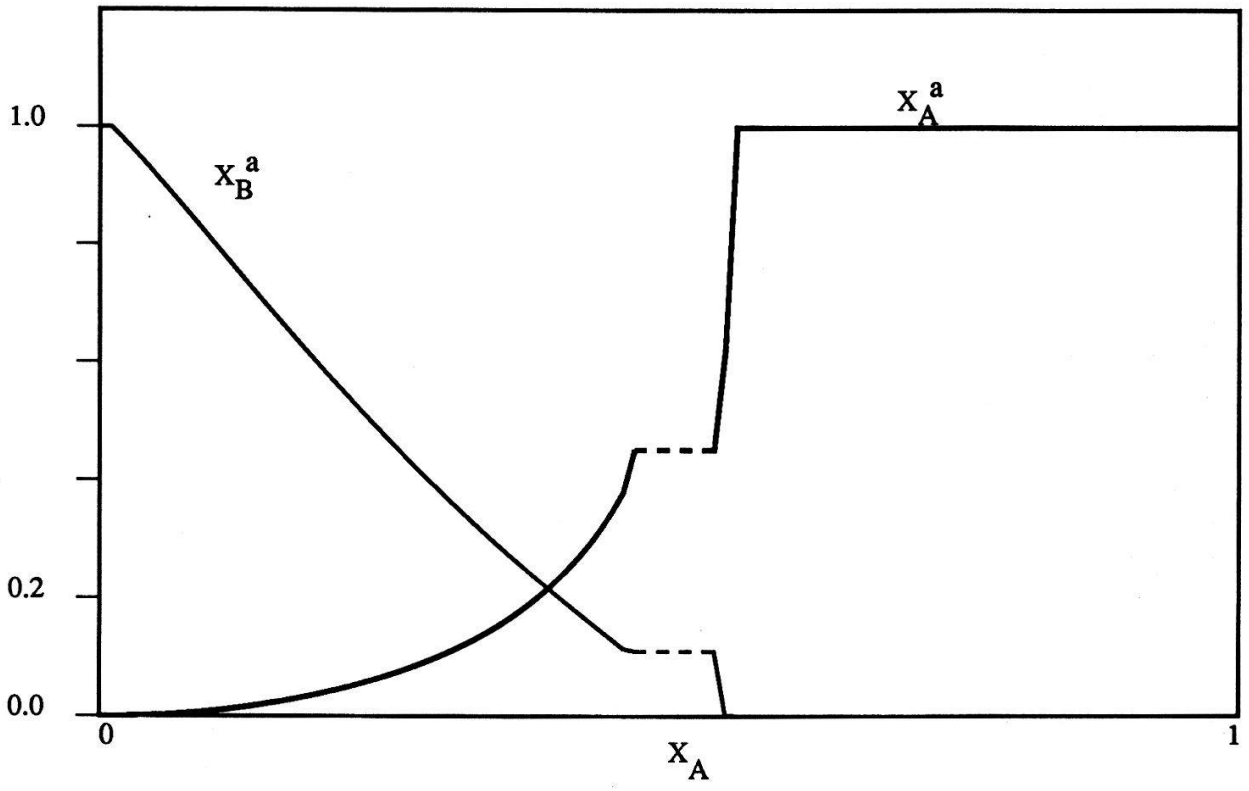

Fig. 1

d). Results of the numerical simulation.

The resulting phase diagram obtained by numerical simulation [33], is shown on fig 2. For $X_A \geq 0.6515 \pm 0,0004 = X_{A1}$ the stationary state is "poisoned" with A. For $X_A \leq 0,5761 \pm 0,0004 = X_{A2}$ the stationary state is poisoned with B. At X_{A1} and X_{A2} one has two nonequilibrium second order phase transitions in the sense that, in the mixed phase, the coverage concentrations vary continuously as a function of X_A at the transitions.

One sees that the exact and the mean field solutions of this model are quite different. This is not very surprising since we expect that the fluctuations play an important role in two dimensions. This shows also the difficulty to find a good analytical approach for such a C.A model.

We have also determined how the coverage fraction X_A^a was going to zero (or one) near the transition points. The distances from the critical points are determined respectively by the parameters $\varepsilon_1 = (X_{A1} - X_A)/X_{A1}$, and $\varepsilon_2 = (X_A - X_{A2})/X_{A2}$.

Fitting the datas in the range $8 \cdot 10^{-4} < \varepsilon_1 < 5 \cdot 10^{-3}$ one finds that

$$\psi_1 \equiv X_A^a(X_{A1}) - X_A^a(X_A) \sim \varepsilon_1^{\beta_1}$$

with $\beta_1 = 0.55 \pm 0.05$.

β_1 is then the stationary critical exponent for the order parameter.

Fig. 2

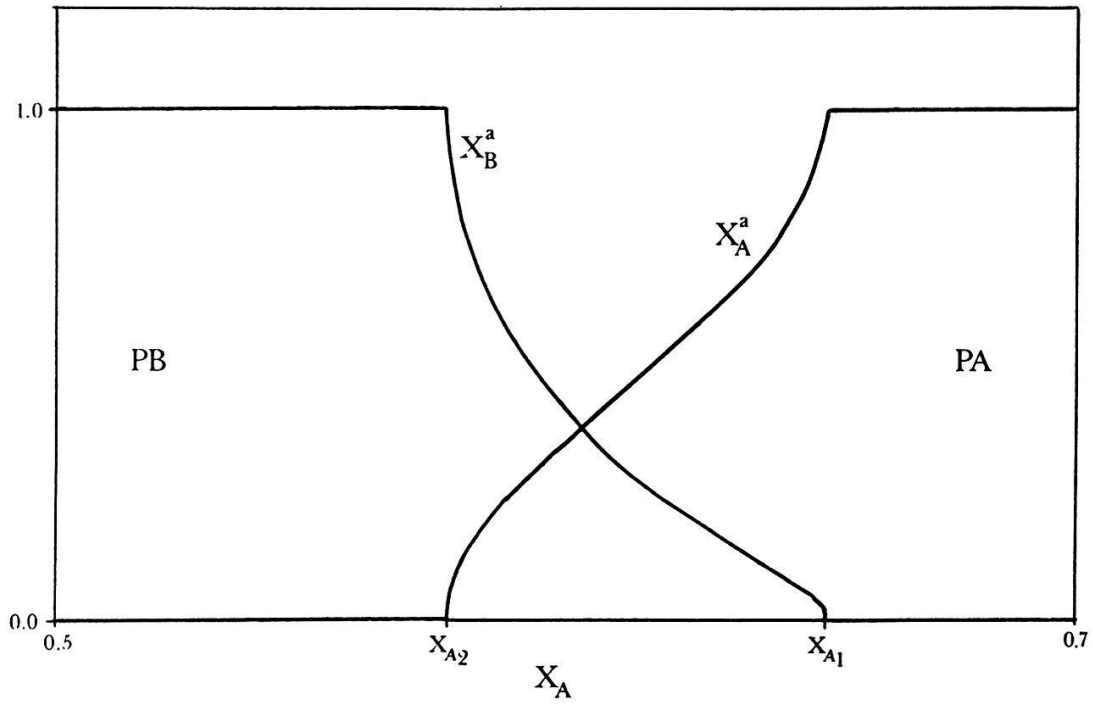

For the second transition, associated to the order parameter ψ_2, one has :

$$\psi_2 \equiv X_A^a(X_A) - X_A^a(X_{A2}) \sim \varepsilon_2^{\beta_2}$$

with

$$\beta_2 = 0,45 \pm 0,05 \quad \text{for} \quad 2 \cdot 10^{-3} < \varepsilon_2 < 10^{-2}.$$

Although the determination of these exponents is not very precise (the precision could be improved by averaging over more samples), the two values obtained are compatible with the values obtained by Meakin-Scalapino [34], for the model of Ziff et al.

Interesting information can also be obtained concerning the dynamics. In equilibrium statistical mechanics, it is known that a system initialy in a nonequilibrium state

will decay towards its equilibrium one, usually exponentially. The decay is characterized by a relaxation time τ. When approaching a second order phase transition, this relaxation time diverges (critical slowing down) like :

$$\tau \sim \varepsilon^{-\Delta}$$

where ε is the reduced temperature, i.e. the distance from the critical point and Δ the dynamical critical exponent.

A similar situation is present in nonequilibrium phase transition. Our cellular automaton model allows us to compute the non equilibrium dynamical critical exponent Δ. The numerical procedure adopted is the following. For a fixed value of X_A, one computes $X_A^a(t)$ or $X_B^a(t)$ depending of the critical point considered. Then the datas are fitted with the following decay law :

$$X_\alpha^a(t) = [X_\alpha^a(0) - X_\alpha^a(\infty)] \exp[-t/\tau(X_A)] + X_\alpha^a(\infty)$$

with $\alpha = A$ or B.

Datas are averaged over 10 samples in order to reduce the statistical errors. One observes a crossover between two different regimes : an early time one characterized by a rapid relaxation and a long time one characterized by the relaxation time $\tau(X_A)$.

Near the transition points, the relaxation times are fitted with the following law :

$$\tau_j(X_A) \sim \varepsilon_j^{-\Delta_j}$$

where $j = 1, 2$ labels the two transitions.

The values obtained for Δ_j are the following. When approaching the transitions from the "disordered" phase, i.e. the poisoned ones one finds, for $9 \cdot 10^{-4} < \varepsilon_{1,2} < 3 \cdot 10^{-2}$:

$$\Delta_1 = 0,98 \pm 0,08 \quad \Delta_2 = 1,03 \pm 0.10.$$

When approaching the transitions from the "ordered" phase, i.e. non poisoned, one finds :

$$\Delta_1 = 1,02 \pm 0,15 \quad \Delta_2 = 0,84 \pm 0,15$$

Both values are compatible with the mean field prediction for usual nonequilibruim second order phase transitions [35].

6. Conclusions.

The C.A are simple discrete dynamical systems that exhibit very complicated behaviour arising from the cooperative effects of many parts, each following a simple rule. Theoretically, many basic questions remains open [36] and, due to their great mathematical complexity, most of these questions will remain open for a long time.

However, has we have seen in the above examples, C.A offer a powerful tool to modelize physical systems. The fast development of special purpose processors, tailored to exploit the full parallelisme of the algorithms, will allows to treat many more difficults problems in a near future.

Moreover, independently of the numerical aspect, the C.A approach poses challenging questions to the physicists, both from the point of view of the modelization of physical problems in terms of discrete dynamics as well as in showing the equivalence between the microscopic models and the physics at the macroscopic level.

Finally, the avaibility of special C.A processors with interactive capabilities and graphic display [37], gives a wonderful pedagogical tool to teach physics in an attractive way.

Références

[1] J. von Neumann "Theory of Self-Reproducing Automata", A. Burks, edt, University of Illinois Press (1966).

[2] M.Gardner, Sc. Am. 223, 120 (1970).

[3] S. Wolfram Rev. Mod. Phys. 55, 601 (1983)

[4] S. Wolfram, Physica D10, 12 (1984)

[5] T. Tofolli, Physica D10, 117 (1984)

[6] L.Kadanoff, Physics Today 39 (9), 7 (1986)

[7] J. Hardi, Y. Pomeau and O. de Pazzis, J. Math. Phys, 14, 1746 (1973)

[8] B. Chopard, M. Droz, Phys. Lett. A126, 476 (1988)

[9] U. Frisch, B. Hasslacher and Y. Pomeau, Phys.Rev.Lett., 56, 1505 (1986).

[10] U. Frish, D. d'Humière, B. Hasslacher, P. Lallemand, Y. Pomeau and J.-P. Rivet, in "Modern Approach to Large Non-linear Systems" to appear in J. Stat. Phys.(1987).

[11] B. Chopard, M. Droz, Proceedings of the conference "Chaos and Complexity", Torino 1987, edt. by World Scientific 1988, to appear.

[12] B. Chopard, M. Droz, this meeting, H.P.A 1988 , to appear.

[13] H. Chen, W.H. Matthaws, Phys. Rev. Lett. 58, 1845 (1987)

[14] D. Montgomery, G.D. Doolen, Phys. Lett. A120, 229 (1987)

[15] S.A. Orsag, V. Yakhot, Phys. Rev. Lett. 56, 1691 (1986)

[16] P.Rujan, Jour. Stat. Phys. 49, 139 (1987)

[17] A. Georges, P. Le Doussal, preprint (1987)

[18] J.D. Gunton, M. Droz "Introduction to the theory of metastable and unstable states", Lecture Notes in Physics 183, Springer-Verlag, Berlin, (1983)

[19] G. Vichniac, in "Disordered Systems and biological Organization , Bienenstock et al. eds., Springer-Verlag (1986).

[20] M. Droz, D. Maeder, Proceedings ICOMAT-86, The Japan Institute of Metals, eds (1986).

[21] B. Chopard, M.Kolb, M. Droz, (in preparation)

[22] B. Chopard, M. Droz, (in preparation)

[23] K. Preston, M.J.D. Duff, "Modern Cellular Automata, Theory and Applications", MIT Press, (1984).

[24] S. Levialdi, in "The Characteristics of Parallel Algorithms", MIT Press, 191, (1987).

[25] T. Tofolli, preprint (1987).

[26] T. Kohonen, "Self organization and Associative Memory", Springer Verlag, (1984).

[27] P.Rujan, in worshop on "Systems with learning and memory abilities", Paris (1987).

[28] K. Binder, "Monte-Carlo Methods in Statistical Physics", Springer-Verlag Berlin, (1987).

[29] M. Creutz, Ann. Phys. (N-Y), 67, 62 (1986).

[30] Y. Pomeau, J. Phys. A17, L415 (1984).

[31] H.J. Hermann, J. Stat. Phys. 45, 145 (1986).

[32] R.M. Ziff, E. Gulari and Y. Brashard, Phys. Rev. Lett. 56, 2553 (1986).

[33] B. Chopard, M. Droz, J. Phys. 21, 205 (1988).

[34] P. Meaking and D.J. Scalapino, J. Chem. Phys. 87, 731 (1987).

[35] R. Dickman Phys. Rev. 34A, 4246, (1986).

[36] S. Wolfram, Phys. Scripta, T9, 170, (1985).

[37] T. Toffoli, N. Margolus, "Cellular Automata Machines", MIT Press (1987).

Helvetica Physica Acta
Vol. 61 (1988)
0018-0238/88/060817-12$1.50+0.20/0

REUNION DE PRINTEMPS DE LA SOCIETE SUISSE DE PHYSIQUE

DES 28 ET 29 MARS 1988 A WINDISCH

*E = Exposé de 4 pages

Matière condensée

Photoemissionsmessungen mit Synchrotronstrahlung an flüssigem Tl, Pb, Bi und Sn

A. Pflugi, G. Indlekofer, P. Oelhafen und H.-J. Güntherodt,
Institut für Physik der Universität Basel, Klingelbergstr. 82,
4056 Basel
D. Chauveau, C. Guillot und J. Lecante, LURE, F-91405 Orsay

*E

Optische und magnetooptische Messungen an ferromagnetischen UCuP2, UCuAs2 und UCu2P2 Einkristallen

P. Fumagalli, J. Schoenes und H. Rüegsegger
Lab. für Festkörperphysik, ETH-Zürich
D. Kaczorowski, Inst. for Low Temperature and Structure
Research, Polish Academy of Sciences, Wroclaw, Poland

*E

Transporteigenschaften vom System UPt - UIr

H. Brändle, J. Schoenes und F. Hulliger
Festkörperphysik, ETH-Zürich

Yb-Al Systeme: eine Fallstudie mit Rumpfniveau-Photoemission

T. Greber, F. Hulliger, Lab. für Festkörperphysik, ETH Zürich,
CH-8093 Zürich
L. Schlapbach, Institut de Physique, Université de Fribourg,
CH-1700 Fribourg

Unterschiedliche Valenz der Yb-Hydride gemessen mit 3d-Photoemission

St. Büchler, R. Monnier, L. Schlapbach* und L. Degiorgi
Laboratorium f. Festkörperphysik, ETHZ, 8093 Zürich
*und Institut de Physique, Université de Fribourg, 1700 Fribourg

Auftreten magnetischer Korrelationen in $CeAl_3$ unterhalb von 2K

S. Barth, F.N. Gygax, B. Hitti, E. Lippelt, A. Schenck, IMP,
ETHZ, c/o PSI, CH-5234 Villigen;
H.R.Ott, Lab. für Festkörperphysik, ETHZ, CH-8093 Zürich;
C. Baines, B. van den Brandt, T. Konter, S. Mango, PSI,
CH-5234 Villigen

μ+ SR Studies in the chevrel phase superconductors

P. Birrer, S. Barth, F.N. Gygax, B. Hitti, E. Lippelt, A. Schenck, IMP ETHZ, c/o PSI, CH-5234 Villigen; D. Cattani, J. Bors, M. Decroux, O. Fischer, Dép. de Phys. de la Mat. Cond., Université de Genève, CH-1211 Genève 4

μ+-Knightshift Messungen an $Bi_{1-x}Sb_x$Einkristallen

E. Lippelt, S. Barth, P. Birrer, F.N. Gygax, B. Hitti, und A. Schenck, IMP, ETHZ, c/o PSI CH-5234 Villigen

Kritisches Verhalten des Antiferromagneten NdAlGa

O. Elsenhans, A. Furrer, Labor für Neutronenstreuung, ETH-Zürich, CH-5303 Würenlingen; E. Walker, Département de physique de la matière condensée, Université de Genève, CH-1205 Genève; K.N. Clausen, Riso National Laboratory, DK-4000 Roskilde

3D-Antiferromagnetic Ordering in the Linear Chain, System Tb_2Cl_3

B. Schmid, P. Fischer, R. Kremer* und A. Simon*
Labor für Neutronenstreuung, ETH Zürich, 5303 Würenlingen
*Max-Planck-Institut für Festkörperforschung, Stuttgart, BRD

Investigation of Electrical Properties of Organic TMBEDT-TTF Salts

M.M. Freund, J.L. Olsen, J.D. Dunitz* and B. Hilti**
Lab. für Festkörperphysik, ETH-Hönggerberg, CH-8093 Zürich
*Laboratorium für Organische Chemie, ETH-Zürich, CH-8092 Zürich
**Ciba-Geigy AG, FO24 Rosental R-1695, Basel

*E
Deviations from Matthiessen's Rule in the presence of dislocations in thin Al foils

J. Romero and R. Huguenin
Institut de Physique Expérimentale, Université de Lausanne, CH-1015 Lausanne

Low-temperature thermal conductivity of UCu_5

A. Bernasconi*, H.R.Ott*, Z.Fisk°
*Laboratorium für Festkörperphysik, ETH-Hönggerberg, CH-8093 Zürich
°Los Alamos National Laboratory, Los Alamos, New Mexico 87545, USA

*E
Boundary thermal conductances in superfluid helium deduced from normal phase propagating velocities along superconduct. wires

J. Casas and L. Rinderer
Institut de Physique Expérimentale, Université de Lausanne, CH-1015 Lausanne

NMR-Untersuchung der Ionendynamik im Superionenleiter $LiNaSO_4$

K.-D. Junke, J. Roos, M. Mali und D. Brinkmann
Physik-Institut, Univ. Zürich, Schönberggasse 9, CH-8001 Zürich

Intersubband Absorption in GaAs/AlGaAs Quantum Wells between 4.2K and Room Temperature

M. Berz, P. von Allmen, G. Petrocelli and F.-K. Reinhart
Institut de Micro- et Optoélectronique, EPF CH-1015 Lausanne
G. Harbeke, PSI c/o RCA Laboratories, Zurich, Switzerland

*E
High sensitive and fast photodetectors at 820 nm

M. Zirngibl, R. Sachot, A. Hofmann, W. Baer, M. Ilegems
Institut de micro- et optoélectronique EPF CH-1015 Lausanne

*E
Measurement and 1D-simulation of high electron mobility transistor

D. Théron, F. Lasagna, H.J. Bühlmann, M. Py, M. Ilegems
Institut de micro- et optoélectronique, EPFL-Ecublens, 1015 Lausanne

Strukturbestimmung des α_3-Zustandes von CO auf Fe(001) mit Photoelektronendiffraktion

J. Osterwalder**, R. Saiki, G.S. Herman, M. Yamada*, und C.S. Fadley, Chemistry Department, University of Hawaii, Honolulu, HI 96822
**Physikinstitut, Universität Fribourg
* Optoelectronics Techn. Res. Corp., Tsukuba, Japan

Spinpolarisierte Photoelektronendiffraktion an MnO(001)

J. Osterwalder*, B. Hermsmeier, D.J. Friedman, B. Sinkovic**, T. Tran und C.S. Fadley, Chemistry Department, University of Hawaii, Honolulu, HI 96822
* Physikinstitut, Universität Fribourg
**AT&T Bell Laboratories

Deposition of amorphous hydrogenated carbon films (a-C:H) on Ge(100): a reactive interface

D. Ugolini and P. Oelhafen, Institut für Physik der Universität Basel, Klingelbergstrasse 82, CH-4056 Basel

Photoemission an freien, kleinen Nickel- und Platinteilchen

M. Ammann, H. Burtscher, U. Müller, A. Schmidt-Ott;
Laboratorium für Festkörperphysik, ETH Zürich.

*E
Influence de l'énergie des ions et de la température de l'objet lors de l'amincissement par bombardement ionique de GaAs

R. Spycher et P.A. Buffat
EPFL, Inst. de Microscopie Electronique, CH-1015 Lausanne

Propriétés électroniques de surfaces et d'interfaces: une étude de RMN

J.P. Bucher*, J.J. van der Klink*, J. Buttet* et M. Graetzel+
*Institut de Physique Expérimentale, EPFL, 1015 Lausanne
+Institut de Chimie Physique, EPFL, 1015 Lausanne

Nichtlineare Wellen als Oberflächenstrukturen von superfluidem Helium II

P.W. Egolf, J.L. Olsen
Laboratorium für Festkörperphysik, ETH, Hönggerberg, 8093 Zürich

Influence des défauts de structure sur la transformation du cobalt

A. Munier, J.E. Bidaux, C. Esnouf, R. Schaller
Institut de génie atomique, EPFL, CH-1015 Lausanne

Snoek-Köster Peak in Cold Worked Niobium

D'Anna Gianfranco, Institut de Génie Atomique, Ecole Polytechnique Fédérale de Lausanne, CH-1015 Lausanne

Precipitation in Fe(Cu) studied by Muon Spin Rotation Spectroscopy

G. Solt, W.B. Waeber, U. Zimmermann and Ph. Tipping,
Paul Scherrer Institute, CH-5303 Würenlingen
A. Schenck, F.N. Gygax and B. Hitti,
Institute for Intermediate Energy Physics, ETH Zürich,
c/o PSI CH-5234 Villigen
P.A. Beaven, Research Centre GKSS, D-2054 Geesthacht, Germany

Positronen-Annihilation in Neutronenbestrahlten Fe-Cu-Legierungen und ferritischen Stählen: Ausheilkinetik und Vergleich mit Härte

U.Zimmermann(1), K.Ghazi-Wakili(2) und Ph. Tipping(1)
(1) Paul Scherrer Institut, CH-5303 Würenlingen
(2) Laboratorium für Festkörperphysik, ETH, CH-8093 Zürich

Neutronenuntersuchung zur Kristallstruktur von $Cs_3RE_2Br_9$; (RE=Tb,Dy,Ho,Er,Yb)

A. Dönni*, A. Furrer*, H.U. Güdel**
* Labor für Neutronenstreuung, ETH-Zürich, 5303 Würenlingen
**Institut für Anorganische Chemie, Universität Bern, 3000 Bern

*E
The Supercooling of Metal Droplets with High Melting Point

V. Soares, E. Meyer* and L. Rinderer
Institut de Physique Expérimentale, Université de Lausanne, CH-1015 Lausanne
*Permanent address: Instituto de Fisica-UFRJ, RJ-21945, Brazil

Tensile properties analysis of 600 MeV Proton Irradiated Al

D.Gavillet, M. Victoria; PIREX, PSI, 5303 Würenlingen
R. Gotthardt, J.L. Martin; IGA EPFL, 1015 Lausanne

Decomposition Pressure of 0_2 over $YBa_2Cu_30_{7-x}$ and Investigations of High Pressure Crystallisation

J. Karpinski, E. Kaldis, Laboratorium für Festkörperphysik
ETH Zürich

Supraleitende Glaseigenschaften von Y $Ba_2Cu_3O_{7-\delta}$: Myon-Spin-Rotation (μSR)-Experimente

B. Pümpin, H. Keller, W. Kündig, W. Odermatt, B.D. Patterson, J.W. Schneider and H. Simmler, Physik-Institut der Universität Zürich, Schönberggasse 9, CH-8001 Zürich
K.A. Müller, J.G. Bednorz, K.W. Blazey, C. Rossel and I.Morgenstern, IBM Research Division, Zürich Research Laboratory, CH-8803 Rüschlikon
I.M. Savic, Faculty of Natural and Mathematical Sciences, 11000 Belgrade, Yugoslavia

A μ+SR Study of the magnetic properties of $La_{1.85}Sr_{0.15}Cu0_4$

B. Hitti, S. Barth, P. Birrer, F.N. Gygax, E. Lippelt,
A. Schenck, IMP, ETHZ c/o PSI CH-5234 Villigen;
D. Cattani, J. Cors, M. Decroux, O. Fischer, Dep. de Physique de la Mat. Cond., Université de Genève, CH-1211 Genève 4

Zuordnung der Cu-NQR-Frequenzen und Cu-Relaxation im Supraleiter $YBa_2Cu_30_{7-x}$

M. Mali, J. Roos und D. Brinkmann
Physik-Institut, Univ. Zürich, Schönberggasse 9, 8001 Zürich

Charakterisierung mittels NQR von unterschiedlich hergestellten Proben des Supraleiters $YBa_2Cu_30_{7-x}$

H. Zimmermann, D. Brinkmann, M. Mali und J. Roos
Physik-Institut, Univ. Zürich, Schönberggasse 9, 8001 Zürich;
F. Greuter und P. Kluge-Weiss
ASEA-BBC-Forschungszentrum, 5405 Baden

Magnetisierung und kritische Stromdichten bei $Yba_2Cu_30_7$ Hochtemperatursupraleitern

K. Kwasnitza, V. Plozner, M. Waldmann, E. Widmer
Paul-Scherrer Institut, CH-5234 Villigen

Coherent and incoherent order of holmium 4f-Moments in the 90k Superconductor $HoBa_2Cu_30_7$ below 300 mK

F.N.Gygax, P. Birrer, B. Hitti, E. Lippelt and A. Schenck
Institute for Intermediate Energy Physics, ETHZ,
Ch-5234 Villigen
S. Barth, F. Hulliger and H.R. Ott, Laboratory for Solid State Physics, ETH-Hönggerberg, CH-8093 Zürich

Antiferromagnetische Fernordnung in HT_c-Supraleitern $RBa_2Cu_30_{7-x}$

P. Fischer a), K. Kakurai b), M. Steiner b), K.N. Clausen c), B. Lebech c), F. Hulliger a), H.R. Ott a), P. Brüesch d), F. Unternährer d) und F. Stucki d)
(a) ETHZ, (b) HMI Berlin, (c) Riso Nat. Lab., (d) Asea-BBC

*E
Synthesis of Y-Ba-Cu-O Thin Films by RF Magnetron Sputtering

M. Akinaga*, D. Abukay and L. Rinderer
Institut de Physique Expérimentale, Université de Lausanne, CH-1015 Lausanne
*permanent address: Department of Physics, Fukuoka University of Education, Fukuoka 811-41, Japan

*E
The Resistivity of Y-Ba-Cu-O Thin Films in the Magnetic Field

D. Abukay, M. Akinaga* and L. Rinderer
Institut de Physique Expérimentale, Université de Lausanne, Ch-1015 Lausanne
*Permanent address: Department of Physics, Fukuoka University of Education, Fukuoka 811-41, Japan

Physique appliquée

Laser-photoakustische Studien an Oberflächenfilmen

M.W. Sigrist, D. Scherrer und W. Riede
Institut für Quantenelektronik, ETH Hönggerberg, CH-8093 Zürich

Kontinuierliche Detektion von Luftfremdstoffen mit einem mobilen CO_2 Laserphotoakustischen Messystem

P.L. Meyer, St. Bernegger und M.W. Sigrist
Institut für Quantenelektronik, ETH Hönggerberg, CH-8093 Zürich

Selektiver Nachweis von Schadstoffen in Fahrzeugabgasen mittels Laserphotoakustischer Spektroskopie

St. Bernegger, P.L.Meyer und M.W. Sigrist
Institut für Quantenelektronik, ETH Hönggerberg, CH-8093 Zürich

Measurement of the Spectral Thermal Emission from Technical Infrared Radiators

A. Leupin, H. Vetsch und F.K. Kneubühl
Institute of Quantum Electronics, ETH Hönggerberg, 8093 Zurich

*E

Spektroskopische Charakterisierung von Gleichgewichts-abweichungen in einem induktiv gekoppelten Plasma

S. Nowak* und J.A.. van der Mullen
Techn. Universität Eindhoven, Postf.513, NL-5600 MB Eindhoven
*Physikinstitut der Universität, Pérolles, CH-1700 Freiburg

Quantitative Bestimmung von Site-Energieverteilungs-Aenderungen in Glasmatrizen mit Hilfe von Photophysikalischem Lochbrennen

D. Glatz, J. Fünfschilling, I. Zschokke-Gränacher
Institut für Physik, Universität Basel, Klingelbergstr.82,
CH-4056 Basel

Spektrales Verhalten eines $YALO_3$:Er Lasers unter selektiver optischer Anregung

J. Frauchiger, W. Lüthy, P. Albers und H.P. Weber
Inst.f.angewandte Physik, Universität Bern, CH-3012 Bern

Niedrige Schwelle und hohe Repetitionsrate eines 3μm $Er^{3+}Cr^{3+}$;YSGG Lasers

P. Albers, S. Schnell, J. Frauchiger, W. Lüthy, H.P. Weber
Inst.f.angewandte Physik, Universität Bern, CH-3012 Bern
V.G. Ostroumov, A.F.Umyskov, I.A.Shcherbakov
Inst. of General Physics, Vavilov Street 38, 117942 Moscow USSR

Modes of DFB Gaslasers with Axially Periodic Oversized Waveguides of Circular Cross-Section

Cui Dafu*, J. Arnesson, S. Gnepf and F.K. Kneubühl
Inst. of Quantum Electronics, ETH Hoenggerberg, CH-8093 Zurich
*on leave from Academy of Sciences, Beijing, PRC

Modes of Helical-Feedback Gas Lasers with Oversized Helical Waveguides

J. Arnesson, Cui Dafu*, S. Gnepf and F.K. Kneubühl
Inst. of Quantum Electronics, ETH Hoenggerberg, CH-8093 Zurich
*on leave from Academy of Sciences, Beijing, PRC

Thermische Ausdehnung als neuer Mechanismus für optische Bistabilität von Fabry-Perot-Resonatoren

P. Pirani und W. Lukosz
Professur für Optik, ETH, 8093 Zürich

Optische Bistabilität mit Oberflächenplasmonen

P. Pirani und W. Lukosz
Professur für Optik, ETH, 8093 Zürich

Externe Gitterkoppler auf planaren Wellenleitern als integriert-optisch bistabile Elemente

V. Briguet, J. Kramer und W. Lukosz
Professur für Optik, ETH, 8093 Zürich

Selbst-Pulsationen beim Prismen-Einkoppeln in planare Wellenleiter: Theory und Experiment

V. Briguet und W. Lukosz
Professur für Optik, ETH, 8093 Zürich

Einfluss des Düsenmaterials auf den Druckaufbau in SF_6-Schalter

R. Meier, H.J. Schötzau und F.K. Kneubühl
Inst. für Quantenelektronik, ETH Hönggerberg, CH-8093 Zürich

Temperaturzerfall eines SF_6 Plasmas

H.J. Schötzau, R. Meier und F.K. Kneubühl
Inst.f.Quantenelektronik, ETH Hönggerberg, CH-8093 Zürich

Spektroskopie an einem RF-angeregten CO_2-Laser Plasma bei extrem kleinen Elektrodenabständen

W. Leuthard, F.K. Kneubühl und H.J. Schötzau
Inst. für Quantenelektronik, ETH Hönggerberg, CH-8093 Zürich

*E
Epitaktische BaF_2SrF_2-CaF_2 Stapel auf Si(111) und Si(100)

S. Blunier, H. Zogg, H. Weibel, AFIF, ETH Hönggerberg,
CH-8093-Zürich

An Integrated Mach-Zehnder Inferferometer With Ga/As/AlGaAs Rib-waveguides And ITO Electrodes

Ch. Wuethrich, J. Faist, D. Pavuna et F.-K. Reinhart
Institut de Micro- et Optoélectronique, EPFL, CH-1015 Lausanne

Thermalisation des électrons dans la lueur négative

P. Kocian, EPF, Institut de Physique Appliquée, CH-1015 Lausanne

*E
Operating Principle of Magnetotransistors

H.P. Baltes, A. Nathan, W. Allegretto
University of Alberta, Edmonton, Canada, T6G 2G7

*E
Use of Polysilicon in Microsensors

H.P. Baltes, M. Parameswaran, M. Buchbinder
University of Alberta, Edmonton, Canada, T6G 2G7

*E
Messung kleiner Temperaturdifferenzen in einem Gas mittels Ultraschall

O. Oehler, J. Wieland und S. Friedrich
Institut für Quantenelektronik, ETH Hönggerberg, CH-8093 Zürich

Microscope acoustique à balayage (SAM) utilisant des ondes continues

A. Kulik, G. Gremaud, Ecole Polytechnique Fédérale de Lausanne, Institut de Génie Atomique, CH-1015 Lausanne

*E

Mittleres Mensch-Maximalalter t_{max}=103.2J, und Tod in physikal. Sicht

J.T.Muheim, M. Kredl (*)
Universität (*) und ETHZ, Hönggerberg, CH-8093 Zürich

Dynamic Evolution of the Source Volumes of Gradual and Impulsive Solar Flare Emissions

F. Goetz, (NASA/GSFC), M.E.BRUNER (Lockheed Res. Lab. Palo Alto CA 94304 USA), C.J. CRANNELL (NASA/GSFC Greenbelt MD 20771 USA), A.MAGUN (I.A.P. University of Bern CH), D.L. McKENZIE (Aerospace Corp. Los Angeles CA 90009 USA)

Infrarotastronomie mit Stratosphärenballonen

A. Holenstein, C. Degiacomi, F.K. Kneubühl and D. Huguenin*
Institut für Quantenelektronik, ETH Hönggerberg, CH-8093 Zürich,
*Observatorium Genf

Photoemission an Verbrennungsaerosolen

O. Carnal, H. Burtscher, A. Schmidt-Ott
Laboratorium für Festkörperphysik, ETH Zürich

Physique théorique

*E
Non-equilibrium correlation functions in a cellular automata model of a fluid

Bastien Chopard and Michel Droz
Département de Physique Théorique, Université de Genève, CH-1211 Genève 4

*E
Physikalische Experimente mit Poincaréabbildungen

M. Kuchler, R. Georgii, W. Stelzel, A. Hübler, E. Lüscher, Physikdepartment, Tech. Universität München, D-8046 Garching

Combinatorial Optimization and Statistical Mechanics: The Football Pool Problem

J. Bernasconi, ASEA Brown Boveri Corporate Research, CH-5405 Baden

*E
Creation and anihilation operators for the Hydrogen atom and related potentials

H.R. Jauslin
Dpt. Physique Théorique, Université de Genève

Current saturation without dissipation: quantum coherence in small metal rings

G. Blatter and D.A. Browne, ASEA Brown Boveri Corporate Research, CH-5405 Baden and
LASSP, Clark Hall, Cornell University, Ithaca NY 14853-2501

Symmetry classification of icosahedral quasicrystals

J. Rhyner, Asea Brown Boveri Corporate Research CH-5405 Baden and Theoretische Physik, CH-8093 ETH-Hönggerberg
L.S. Levitov, Landau Institute for Theoretical Physics, USSR Academy of Sciences, Moscow, USSR

*E
Space groups for quasicrystals with (2+1)-reducible point group

Franz Gähler, Département de Physique Théorique, Université de Genève, 24 Quai Ernest Ansermet, CH-1211 Genève 4, Switzerland

Helvetica Physica Acta
Vol. 61 (1988)

0018-0238/88/060829-04$1.50+0.20/0

OPTICAL AND MAGNETO-OPTICAL PROPERTIES OF FERROMAGNETIC $UCuP_2$, $UCuAs_2$ AND UCu_2P_2 SINGLE CRYSTALS

P. Fumagalli, J. Schoenes and H. Rüegsegger, Laboratorium für Festkörperphysik, ETH Zürich, CH - 8093 Zürich, Switzerland
D. Kaczorowski, Institute for Low Temperature and Structure Research, Polish Academy of Sciences, 50-950 Wrocław, P.O. Box 937, Poland

Optical reflectivity and magneto-optical Kerr effect measurements have been performed over a wide energy range. These ternary uranium pnictogen compounds are shown to be metallic with rather few free carriers. In all compounds a intra uranium f → d transition could be resolved with transition energies of 0.55, 0.51 and 0.64 eV for $UCuP_2$, $UCuAs_2$ and UCu_2P_2, respectively. Furthermore,we could give evidence for an increase in f-state localisation in the series $UCuP_2$ → $UCuAs_2$ → UCu_2P_2.

Recently Zołnierek et al. [1,2] and Stępień-Damm et al. [3] reported first structure determination and magnetic studies of ternary uranium transition metal pnictides, which have not been studied so far except for UNi_2P_2 [4]. The U-Cu-ternaries are without exception ferromagnetic, while the U-Ni-ternaries are all antiferromagnetic. All these compounds crystallise in a high symmetry. UCu_2P_2 has a hexagonal structure with space group $P\bar{3}m1$ and $UCuAs_2$ and $UCuP_2$ have a tetragonal structure with space group P4/nmm and I4/mmm, respectively [1]. Ordering temperatures and magnetic moments of 76 K and 0.98 μ_B ($UCuP_2$), 131 K and 1.27 μ_B ($UCuAs_2$) and 216 K and 1.78 μ_B (UCu_2P_2) have been measured [5]. Our samples are single crystals, which have been synthesised at Wrocław, Poland, using a chemical transport method with iodine as transport agent [2,3]. The optical and magneto-optical measurements have been performed on natural grown ($UCuP_2$, $UCuAs_2$) or cleaved (UCu_2P_2) surfaces perpendicular to the c-axis. The experimental set-up is described elsewhere [6].

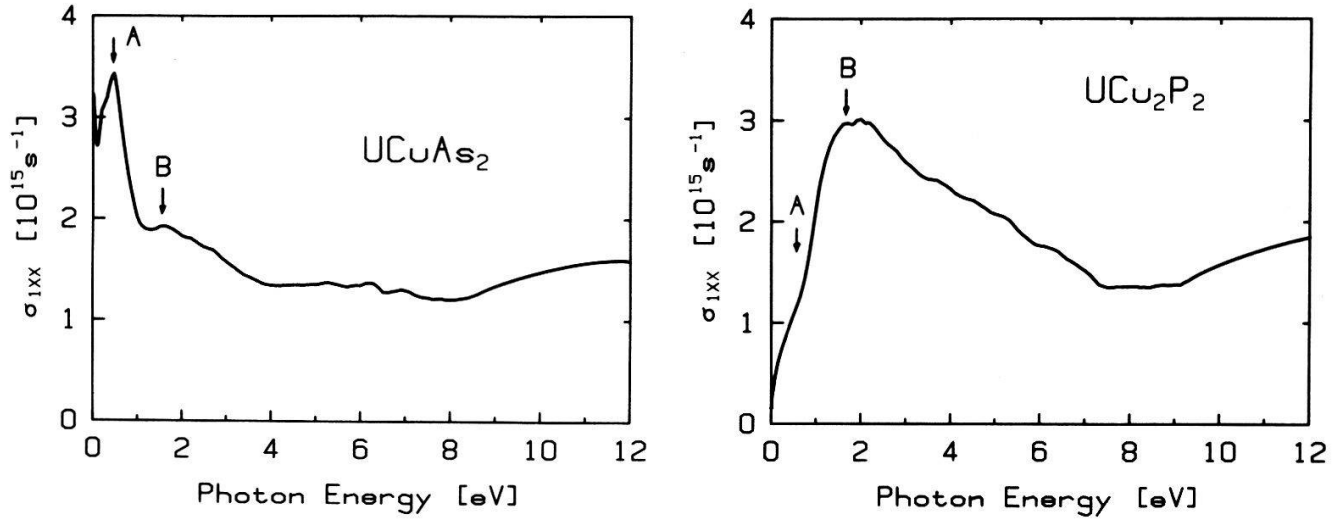

Fig. 1. The optical conductivity at room temperature of $UCuAs_2$ (left) and UCu_2P_2 (right) as calculated from the reflectivity measurements.

Here we report first measurements of the optical reflectivity from 0.03 to 12 eV at room temperature and of the complex magneto-optical Kerr effect from 0.6 to 5 eV at 10 K and 4 T on $UCuAs_2$ and UCu_2P_2 single crystals. Similar investigations on $UCuP_2$ have been published recently [7]. All compounds are found to be metals with rather few free carriers. A plasma edge is hardly discernible in $UCuAs_2$. At higher energies some small structures arising from interband transitions are visible. From the reflectivity measurements we have calculated the optical conductivity and the dielectric function using the Kramers-Kronig relation. The real part σ_{1xx} of the optical conductivity (fig. 1) is dominated for these compounds by interband transitions, giving rise in $UCuAs_2$ to a sharp peak, labelled A, at 0.51 eV and some smaller structures around 2 and 6 eV. In UCu_2P_2 interband transitions manifest themselves in a small shoulder A at 0.7 eV, a broad peak B at 2 eV and several small structures between 4 and 6 eV. Corresponding peaks are found in $UCuP_2$ at 0.55 eV and at 2.0 eV [7]. A fit of σ_{1xx} with Lorentzians reveals for peak A a decreasing oscillator strength along the series $UCuP_2 \rightarrow UCuAs_2 \rightarrow UCu_2P_2$. Together with an increase of the ordered magnetic moment, this can be interpreted as an increasing localisation of the uranium-f states going from $UCuP_2$ to $UCuAs_2$ and to UCu_2P_2. This correlation between the oscillator strength of $f \rightarrow d$ (and also $d \rightarrow f$) transitions and the localisation of the f states has been established in a study of many f-systems [8]. For $UCuAs_2$ we were able to fit the free electron part in σ_{1xx}, revealing a value of

1.73 eV for the unscreened plasma frequency and a damping of 0.11 eV. This corresponds to 0.16 electrons per formula unit, setting the effective mass equal to the free electron mass.

The magneto-optical Kerr effect shows for UCu_2P_2 a high maximum rotation of 3.5 deg at 0.75 eV. The Kerr ellipticity reaches a value of 2 deg at 1 eV. The Kerr rotation of $UCuAs_2$ exhibits a maximum value of 1.75 deg at 1.2 eV, while the maximum Kerr ellipticity was measured to be 1.1 deg at 2.3 eV. Using the Kerr rotation and the Kerr ellipticity, we have calculated the real part σ_{1xy} and the imaginary part σ_{2xy} of the off-diagonal conductivity (fig. 2). The extrapolation (solid line) to zero energy was obtained by Kramers-Kronig transforming a chosen extrapolation for σ_{1xy}, say, to give the best agreement with the experimental curve σ_{2xy}, and vice versa. One observes a structure with diamagnetic line shape in both compounds corresponding to peak A in σ_{1xx} and a structure with paramagnetic line shape corresponding to peak B. Because of its line shape and its large oscillator strength in σ_{2xy} we assign structure A to an intra uranium f → d transition. Normalising the total weight $\langle\sigma_{2xy}\rangle = {}_0\int^{\infty}|\sigma_{2xy}|d\omega$ of transition

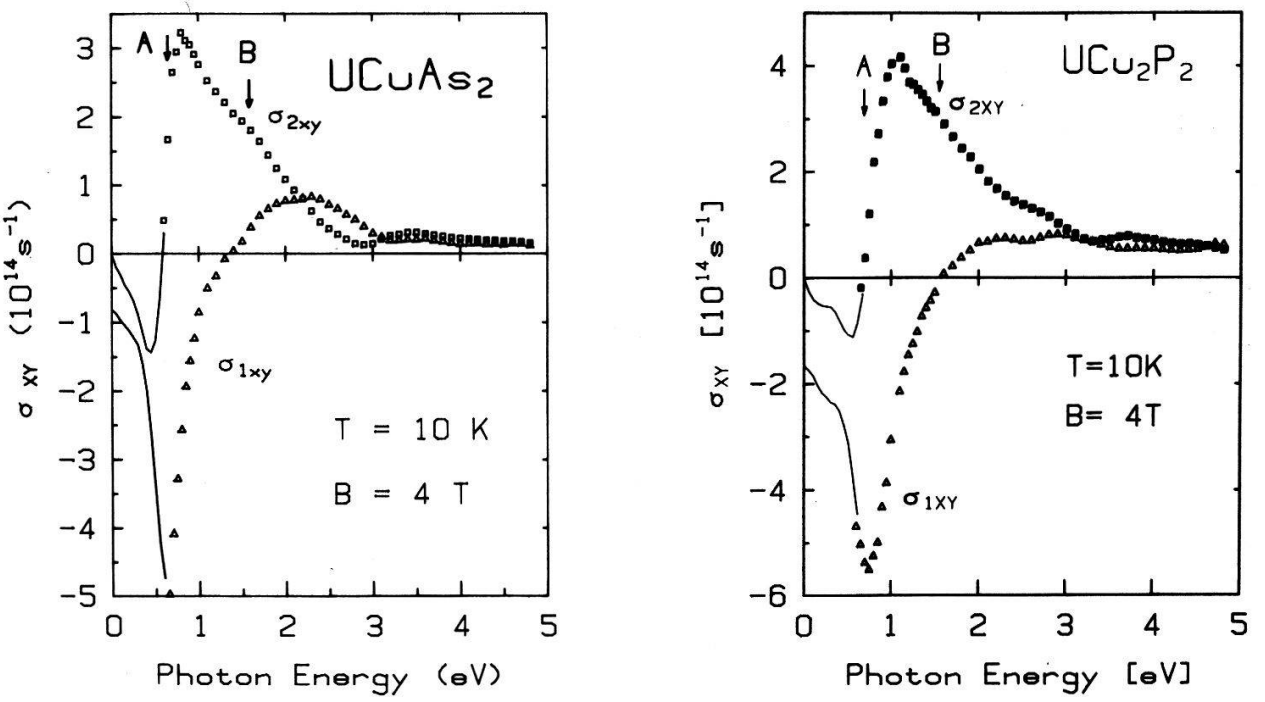

Fig. 2. The complex off-diagonal conductivity at 10 K and 4 T of $UCuAs_2$ (left) and UCu_2P_2 (right) as calculated from the complex Kerr effect and the optical constants.

A with its oscillator strength $\langle\sigma_{1xx}\rangle = \int_0^\infty \sigma_{1xx}\, d\omega$ and with the ordered magnetic moment μ_{ord} one gets for the three compounds the same value within ±15%. This means, that this transition is proportional to $\langle\sigma_{1xx}\rangle$ and to μ_{ord}, corroborating our assignment of this structure to the same kind of f → d transition in the three compounds. Structure B we tentatively assign to a (pd) → f transition, because of its paramagnetic line shape and its rather large oscillator strength in σ_{1xx}.

[1] Z. Zołnierek, D. Kaczorowski and R. Troć, J. Less-Common Metals 121, 193 (1986)

[2] Z. Zołnierek, H. Noël and D. Kaczorowski, J. Less-Common Metals 128, 265 (1987)

[3] J. Stępień-Damm, D. Kaczorowski and R. Troć, J. Less-Common Metals 132, 15 (1987)

[4] W.K. Hofmann and W. Jeitschko, J. Solid State Chem. 51 (1984)

[5] D. Kaczorowski and R. Troć, 17ème Journées des Actinides (1987)

[6] J. Schoenes, Handbook on the Physics and Chemistry of the Actinides, Vol. 1, edited by A.J. Freeman and G.H. Lander, North Holland, Amsterdam (1984) p. 341

[7] P. Fumagalli and J. Schoenes, Solid State Comm. 65, 173 (1988)

[8] J. Schoenes, Moment Formation in Solids, Plenum Publishing Corporation, New York (1984), p. 237

Helvetica Physica Acta
Vol. 61 (1988)

0018-0238/88/060833-04$1.50+0.20/0

TRANSPORT PROPERTIES OF UIr

H. Brändle, J. Schoenes and F. Hulliger
Laboratorium f. Festkörperphysik, ETH, CH-8093 Zürich, Switzerland

Abstract: Resistivity measurements on polycrystalline UIr, $UIr_{0.5}Pt_{0.5}$ and UPt and Hall measurements on UIr between 3 and 300 K point to itinerant ferromagnetism in these compounds.

UIr and UPt both crystallize in a monoclinic PdBi-like distorted CrB structure (1,2). Both compounds are ferromagnetic with ordering temperatures of 46 K and 27 K, respectively. $UIr_{0.5}Pt_{0.5}$ has a Curie temperature of 64 K. We have carried out measurements of the electrical resistivity on polycrystalline UIr, $UIr_{0.5}Pt_{0.5}$ and UPt using the ac van der Pauw method. The Hall effect was measured on UIr in magnetic fields up to 100 kOe, generated by a split-coil superconducting magnet.

Our resistivity measurements on UIr, $UIr_{0.5}Pt_{0.5}$ and UPt are shown in Fig.1. The residual resistiviy ρ_o of the three compounds are 8.0, 68 and 39 $\mu\Omega$cm, respectively. The value for UPt is slightly higher than the one reported by Frings and Franse (3). The high ρ_o value of the mixed system reflects the statistical distribution of Ir and Pt.

In the magnetically ordered phase the electrical resistivity follows a T^2 law . While in UPt the T^2 dependence is obeyed up to 10 K, the data for UIr follow the T^2 law up to 30 K. In the mixed system, the T^2 dependence is followed up to 42 K, however, some deviations occur below 15 K.

The ordering temperature manifests itself as a pronounced knee in the resistivity curves. The inset of Fig.1 shows the deri-

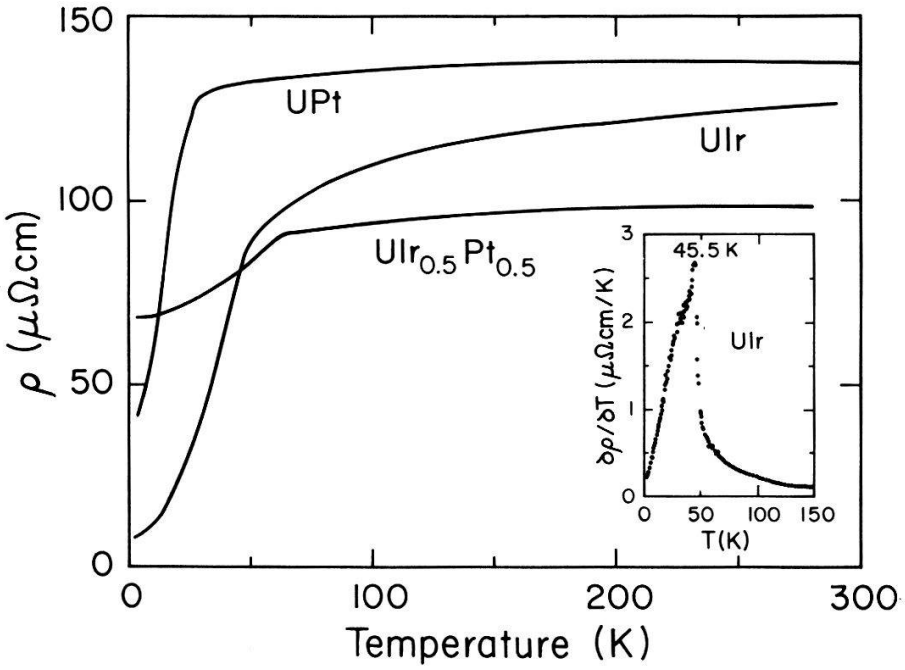

Fig.1: The electrical resistivity as a function of temperature between 3 and 300 K for UIr, $UIr_{0.5}Pt_{0.5}$ and UPt. For UIr the temperature derivative of the resistivity, $\partial\rho/\partial T$, is given in the inset.

vative $\partial\rho/\partial T$ for UIr. The phase transition from the paramagnetic to the ferromagnetic phase is marked by a sharp maximum at 45.5 ± 1 K which is in good agreement with $T_C = 46 \pm 2$ K derived from magnetic measurements (4). In addition we observe a shoulder near 30 K. A similar behaviour also occurs in the derivative $\partial\rho/\partial T$ of UPt and has been associated with a change of the magnetic structure (3).

Above T_C the resistivity of all three compounds shows net deviations from linearity. These are most pronounced in UIr and hinder an unambiguous subtraction of the electron-phonon contribution from the total resistivity. We note that the resistivity curve of UIr is quite similar to that of the heavy electron system UPt_3 (3).

Fig. 2 displays the Hall resistivity of UIr in fields of 20 and 40 kOe. We find a positive Hall coefficient with a maximum

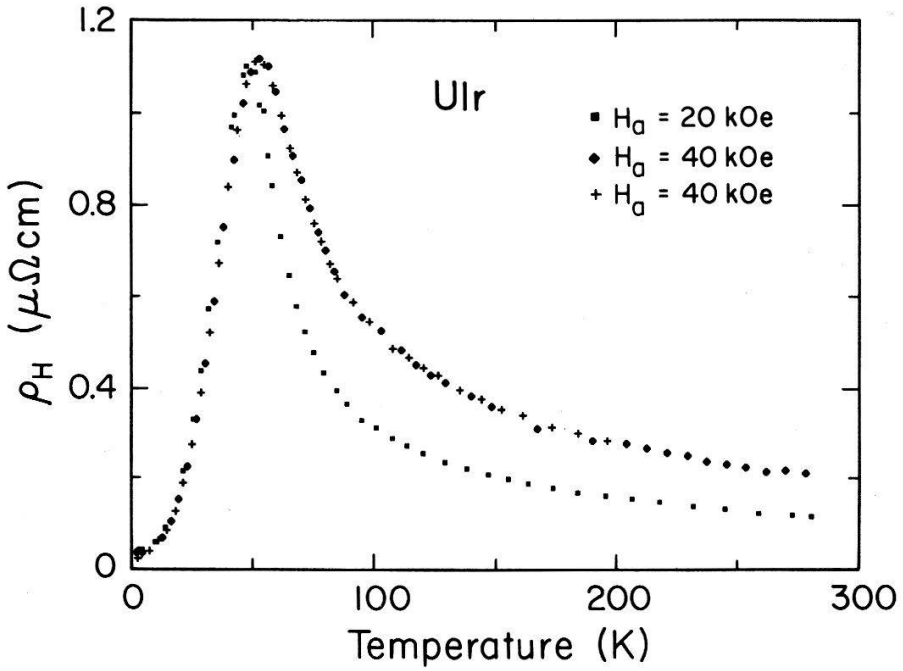

Fig.2: Hall resistivity as a function of temperature between 3 and 300 K for UIr in fields of 20 and 40 kOe.

near 50 K. The weak field dependence of the Hall effect below T_C indicates that the total Hall effect is dominated by the extraordinary part. A fit of the Hall resistivity for $70 < T < 300$ K using the empirical ansatz

$$\rho_H = R_o \cdot B + 4\pi M \cdot R_s \qquad (1)$$

leads to unsatisfactory results, as does a fit setting in eq.(1) $R_s(T) = r_s \cdot \rho_{mag}(T)$.

Below T_C fits at constant temperatures and variable fields, using eq. (1), have been successful for $T \leq 30$ K. A decomposition into the ordinary and extraordinary contributions results in the values listed in Table 1. One notes a negative ordinary Hall coefficient R_o whose absolute value decreases strongly with decreasing temperature. In the simple one-band model of the Hall effect this corresponds to an increase of the conduction electron density from 1 e^-/formula unit at 30 K to about 7.6 e^-/f.u. at 3 K. Although we do not believe that this model should be taken too literally at low temperatures, an increase of the conduction electron concentration with decreasing temperature is in agreement

Table 1: The ordinary (R_o) and the extraordinary (R_s) Hall coefficients, the carrier concentrations n_{UIr} and the ratio R_s/R_o of UIr for various temperatures.

T(K)	$R_s(cm^3/As)$	$R_o(cm^3/As)$	$n_{UIr}(e^-/cm^3)$	R_s/R_o
3	$0.54 \cdot 10^{-2}$	$-3.6 \cdot 10^{-5}$	7.6 ± 0.5	150
20	$2.28 \cdot 10^{-2}$	$-8.9 \cdot 10^{-5}$	2.9 ± 0.4	256
30	$6.69 \cdot 10^{-2}$	$-25.9 \cdot 10^{-5}$	1.0 ± 0.05	258

with similar observations in heavy electron system like UPt_3 when coherence scattering sets in (5).

The extraordinary Hall coefficient R_s, as derived from the fit, scales nicely with the square of the total electrical resistivity, which is in agreement with the side-jump theory (6).

In conclusion we have obtained several indications that UIr and UPt should be described as itinerant ferromagnets. These indications are i) the general behaviour of the resistivity as a function of temperature which is quite similar to that of nickel and iron and ii) the change of the conduction electron concentration in the ferromagnetic phase which points to a change of the bandstructure as a function of temperature.

1) T. Siegrist, Y. Le Page, V. Gramlich, W. Petter, A. Dommann and F. Hulliger, J. Less-Common Met. 125 (1986) 167.
2) A. Dommann and F. Hulliger, Solid State Commun. 65 (1988) 1093.
3) P.H. Frings and J.J.M. Franse, J.Magn.Magn.Mater. 51 (1985) 141.
4) A. Dommann, F. Hulliger, T. Siegrist and P. Fischer, J.Magn.Magn.Mater. 67 (1987) 323.
5) J. Schoenes and J.J.M. Franse, Proc. Int. Conf. on High - T_c Superconductors and Materials and Mechanisms of Superconductivity, Interlaken 1988, to be published in Physica C.
6) A. Fert, Proc. Int. Symposium on Physics of Magnetic Materials, Sendai (Japan) 1987, M. Takahashi, S. Maekawa, Y. Gondo and H. Nosé, eds., World Scientific, Singapore, p. 503.

Helvetica Physica Acta
Vol. 61 (1988)

0018-0238/88/060837-04$1.50+0.20/0

Deviations from Matthiessen's Rule in the presence of dislocations in thin Aluminium foils

J Romero and R Huguenin
Institut de Physique Expérimentale, Université de Lausanne, BSP
1015 Lausanne, Switzerland

High resolution measurements of the electrical resistivity $\rho(T)$ of thin Al foils in presence of dislocations are presented in the temperature range $1.2K \leq T \leq 9K$. The residual resistivity ρ_0 increases and the temperature dependent part of the resisitivity $\Delta\rho(T)$ decrease with increasing dislocation density N. Besides the electron-phonon (e-ph) contribution, $\Delta\rho(T)$ contains a contribution from electron-electron (e-e) scattering. Both show negative deviations from Matthiessen's rule (DMR) at all temperatures as the dislocation density increases.

Introduction

In spite of a considerable amount of theoretical [1], [2] and experimental [3], [4] work on the subject, the scattering of conduction electrons by dislocations is a process not yet well understood. Experimentally dislocations are known to induce negative deviations from the Matthiessen's rule (DMR) in the electrical resistivity of Al [3],[4]. To explain this a theory has been proposed [5] based on small-angle scattering which predicts a decrease of the e-ph term ($\sim T^5$); anisotropy introduced by the dislocations is expected to increase the e-e term proportional to T^2 [5]. Experiments [6] showing these behaviours are few and more evidence is needed to confirm the theory. On the other hand, the existence of a surface dependent T^2-term at high T in the dc resistivity of thin Al foils is now well established [7], [8]. Whether this term is a surface scattering contribution or results from an intrinsic scattering mechanism enhanced by the surface is still an open question. At low temperature this T^2-term could be confused with the e-e scattering which has a smaller magnitude [9] and seems to be surface-dependent [10]. In any case introducing dislocations must reduce the influence of the surface by reducing the electron mean free path. So, irrespective of its origin, the surface-dependent T^2-term must decrease as N increases. To investigate the competitive influence of dislocations on e-e scattering and on surface scattering, we have performed high resolution measurements of the electrical resistivity in the temperature range $1.2K \leq T \leq 9K$ on a progressively deformed thin Al sample where size effects are present.

Experimental procedure

The sample was a thin Al foil of thickness $d=13\ \mu m$ obtained by chemically thinning an initial sample of $d=70\ \mu m$. Its preparation, caracteristics and history

have been already presented [10] with the experimental set up allowing the high resolution measurements of $\rho(T)$. The deformation process was achieved by wrapping the sample around a cleaned insulating stick of 10 mm diameter, then making the sample flat again. This was done sometimes up to 5 times to produce a substantial change in the resistivity. After deformation the sample was kept during 5 days at 60 °C allowing for the release of vacancies and keeping only dislocations in the sample. The geometrical factor was determined at room temperature after each deformation with an accuracy better than 0.1% .

Experimental results and discussion

One effect of deformation is to increase the residual resistivity $\rho_0=\rho(1.2K)$. For our sample ρ_0 has been increased by 20% between the initial and the final state, the amount of the additionnal resisitivity due to dislocation being $\Delta\rho_d=10.133$ pΩm. As the exact ρ_d in the initial sample is difficult to estimate, we will not speake of the dislocation resistivity or the dislocation density, but rather of the variation of N through the increase of ρ_0.

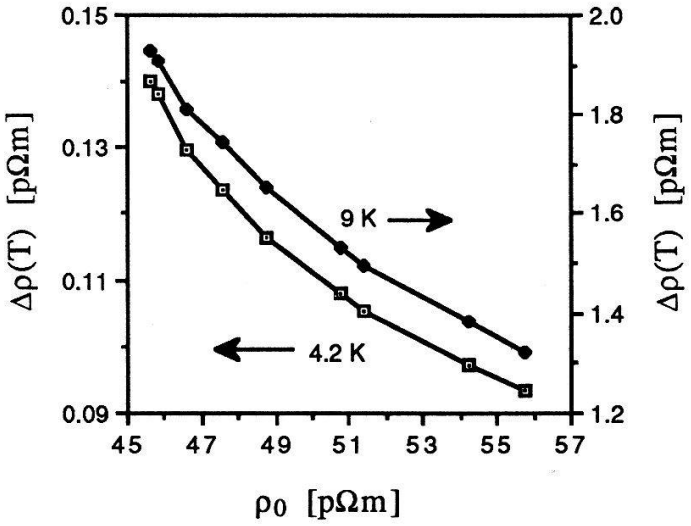

Figure 1. Temperature dependent part of the resistivity at 4.2 K (■) and 9 K (●) plotted versus the residual resistivity ρ_0 increased by deformation.

Another effect of deformation is to change the temperature dependent part of the resistivity $\Delta\rho(T)=\rho(T)-\rho_0$. Figure 1 shows $\Delta\rho(T)$ as a function of ρ_0 for T=4.2K and T=9K. As observed, there is a general decrease of $\Delta\rho(T)$ with increasing deformation or, in other words, a negative deformation-induced deviations from Matthiessen's rule (DIDMR). The same behaviour is also observed at intermediate temperatures between 1.2K and 9K. The relative decrease of the most deformed sample compared to the initial one is 33.2% for T=4.2K and 31.5% for T=9K, the

high resolution allowing to take these figures as significant. These results compare with other experiments [3], which also show a smaller decrease in $\Delta\rho(T)$ with strain for higher T, until it desappears when $\Delta\rho(T)\approx\rho_0$. A quantitative explanation of negative DIDMR has been given in terms of the anisotropy over the Fermi surface of the electron-dislocation scattering relaxation time, which is supposed to be similar to the anisotropy of the relaxation time for e-ph scattering at low temperature [5]. In this theory, the contribution to the resistivity from the non-spherical portions of the Fermi surface (near the intersections with the Brillouin zone boundaries, where the scattering time is smallest) plays an essential role for dislocation scattering, in contrast to scattering with impurities.

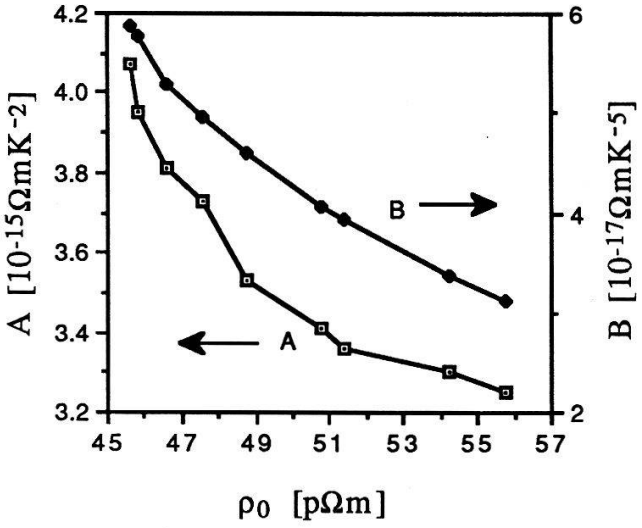

Figure 2. The coefficients A (■) of the T^2-term and B (●) of the T^5-term plotted versus the residual resistivity ρ_0 increased by deformation.

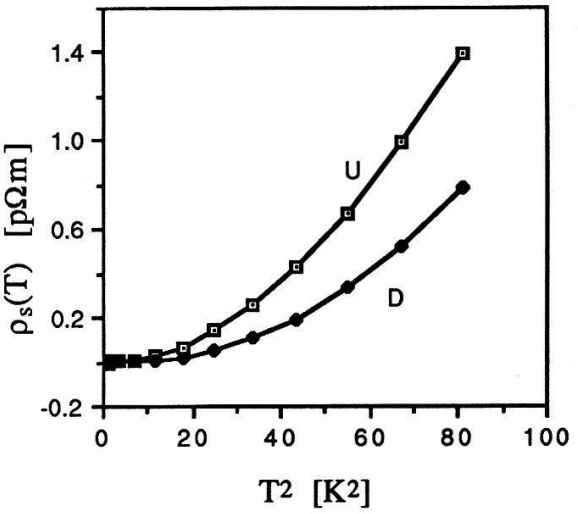

Figure 3. The surface resistivity ρ_s (defined in the text) of the undeformed U (■) and deformed D (●) samples plotted as a function of T^2.

The analysis of $\rho(T)$ for the deformed sample is the same as for the undeformed sample [10], a good fit for $1.2K\leq T\leq 4.2K$ being obtained with $\rho(T)=\rho_0+AT^2+BT^5$. Furthermore, for this sample, $\rho l=1.2 f\Omega m^2$ with a bulk mean free path $l(\infty,1.2K)=156\mu m$. The terms AT^2 and BT^5 have the right order of magnitude to be attributed respectively to e-e and to e-ph scattering, the values of A and B being enhanced by surface scattering. In the present experiment A decreased by 20% and B by 50 % from the initial to the most deformed state. The extrapolated values for the bulk [10] deduced from the undeformed sample were $A=3\pm0.2$ $f\Omega m/K^2$ and $B=0.02\text{-}0.04$ $f\Omega m/K^5$. It is seen in Figure 2 that A and B tend to these values when ρ_0 increases. The surface resistivity $\rho_s(T)=[\rho(T)-\rho(0)]-[\rho_\infty(T)-\rho_\infty(0)]$ is plotted in Figure 3 as a function of T^2. The influence of dislocations on $\rho_s(T)$ is clearly demonstrated : the T^2-behaviour observed in $\rho_s(T)$ at high temperature [8] strongly saturates at low T particularly in the deformed sample. The behaviour of B is well explained by the reduction of the surface contribution and by the

anisotropic model. This agrees with other experiments [6] on bulk samples showing an increase of B by 60% after reduction of N by annealing

The theory predicts in the bulk an increase of A due to dislocations because they are anisotropic scatterers acting similarly to Umklapp-scattering, the only resistive e-e process in the isotropic limit. The observed decrease of A in our experiment is understandable in terms of a reduction of the influence of the surface scattering. Irrespective of the origin of the T^2-term observed in thin foils, increasing N, and so ρ_0, limits the mean free path and consequently the size effects are reduced. In our experiment, where size effects ($d/l(\infty,1.2K)\approx 0.1$) are dominant this apparently overwhelmes the possible increase of the e-e term from anisotropic dislocation scattering.

Conclusions

Negative DIDMR have been observed in the electrical resistivity of thin Al foil between 1.2K and 9K. A T^2-term present in the resistivity ascribed to electron-electron scattering enhanced by the surface is found to decrease with increasing dislocation density, as well as the electron-phonon T^5-term. This behaviour can be explained by the interaction between dislocations and size effects. The increase of the electron-electron contribution to the resistivity predicted by the theory is not apparent here, where size effects dominate.

The financial support of the Swiss National Science Foundation is gratefully acknowledged.

References

[1] M Kaveh and N Wiser, J Phys F : Metal Phys 16 795 (1986)
[2] R A Brown, Can J Phys 60 766 (1982)
[3] J A Rowlands and S B Woods, J Phys F : Metal Phys 8 1929 (1978)
[4] T Endo, K Sasaki and T Kino, J Phys F : Metal Phys 15 1963 (1985)
[5] A Bergmann, M Kaveh and N Wiser, Solid State Comm 34 369 (1980)
[6] M Sinvani, A J Greenfield, A Bergmann, M Kaveh and N Wiser, J Phys F : Metal Phys 11 149 (1981)
[7] J van der Maas , R Huguenin and C Rizzuto, Recent Dev in : Cond Matt Phys vol 2, 63, Ed J T Devreese et al, Plenum Publishing Corp, New York 1981
[8] J R Sambles and K C Elsom, J Phys F : Metal Phys 15 161 (1985)
[9] J H J M Ribot , J Bass , H van Kempen , R J M van Vucht and P Wyder, Phys Rev B 23 532 (1981)
[10] J Romero, J van der Maas and R Huguenin, Helv Phys Acta 61 149 (1988)

Helvetica Physica Acta
Vol. 61 (1988)

0018-0238/88/060841-04$1.50+0.20/0

Boundary thermal conductances in superfluid helium deduced from normal phase propagating velocities along superconducting wires.

J. Casas and L. Rinderer
Institut de Physique Expérimentale, Université de Lausanne, CH-1015 Lausanne

Abstract: Joule heat release is responsible for the creation and longitudinal propagation of a normal phase along a superconducting wire. Theoretical calculations of normal propagating velocities versus electrical current introduce a heat transfer coefficient between the wire wall and the helium bath. A boundary thermal conductance coefficient is inferred from the comparison of experimental and theoretical data for a tin wire at different bath temperatures T_b. The deduced boundary conductance is proportional to T_b^n, where n is a constant.

1. Introduction

Propagation of a normal phase along a superconducting wire can occur for currents below the Silsbee critical current, I_0. Joule heat release is responsible for the longitudinal normal phase propagation. The normal zone propagation velocity depends on the circulating current, I_s, and on the heat transfer process. Different theories [1-5] attempt to describe the experimental results depending on the wire (geometry, with or without electrical insulation, multifilamentary, etc) and cooling bath (He-I or He-II) characteristics.

2. Experimental set-up

A bare tin wire is immersed in a saturated He-II bath. The current circulating in the sample is supplied by a fast and stable current pulser [6]. A pulsed local magnetic field nucleates a normal phase along the wire if there is no spontaneous creation of the normal phase [5]. The normal propagation velocity is deduced from the voltage measured between two points as the superconducting phase disappears [5].

3 Theory

As the responsible mechanism of the longitudinal normal phase propagation is the Joule heat generation, the heat equations describing the wire must be solved. The wire is divided into three parts:

1 - The region where the wire section is completely in the normal phase, **N**.
2 - The region where the wire section is completely in the superconducting phase, **S**.
3- The region where the superconducting-normal phase transition occurs, **T**.

The theory developed supposes a uniform temperature for the wire section (small diameter wires) and a critical temperature, T_t (corresponding to the circulating current, I_s), in the transition region, **T**. For the completely superconducting and normal regions the heat equation to be solved is:

$$Q + K\frac{\partial^2\theta(z,t)}{\partial z^2} = C\frac{\partial\theta(z,t)}{\partial t} + H(z,t) \qquad (1)$$

where Q is the Joule heat released per u. vol., θ the temperature difference between the wire wall and the helium bath, z the longitudinal position, t the time, K the thermal conductivity, C the specific heat and H the rate of heat released to the He-II bath per u. vol. For the superconducting region Q evidently vanishes.

Equation (1) is reduced to a one dimensional differential equation using a moving coordinate [7]. The heat exchange term, H(z,t), employed is:

$$H(z,t) = \frac{2\,h}{a}\theta(z,t) \qquad (2)$$

where h is the thermal boundary conductance between the wire wall and the He-II bath and a the wire radius. Equation (1) is easily solved using this simple heat exchange term, H(z,t), with the proper boundary conditions and supposing K and C constants. The thermal exchange coefficient, h, is deduced from the comparison of the experimental and theoretical data.

The last heat equation to be introduced describes the heat fluxes balance in the transition region:

$$V\,L\,\Sigma = \pi\,a^2\,K\left[\left.\frac{\partial\theta(z,t)}{\partial z}\right|_{z\to z_s} - \left.\frac{\partial\theta(z,t)}{\partial z}\right|_{z\to z_n}\right] - \pi\,a^2\,\delta\,H(z,t) \qquad (3)$$

where L is the latent heat absorbed by the superconducting-normal transition [8], Σ the superconducting-normal phases interface area [1], z_s and z_n respectively the **S-T** and **T-N** boundary position and $\delta = |z_s - z_n|$ the **T** region length.

Equation (1) calculates the derivatives introduced in equation (2). Finally equation (3) permits to calculate the normal phase propagating speed, V, versus the circulating current, I_s.

4. Comparison between theoretical and experimental propagating velocities

Measurements were done for a tin wire for different bath temperatures. Table I shows the experimental parameters introduced to solve the theoretical equations. Figure 1 compares the experimental and theoretical data and it can be

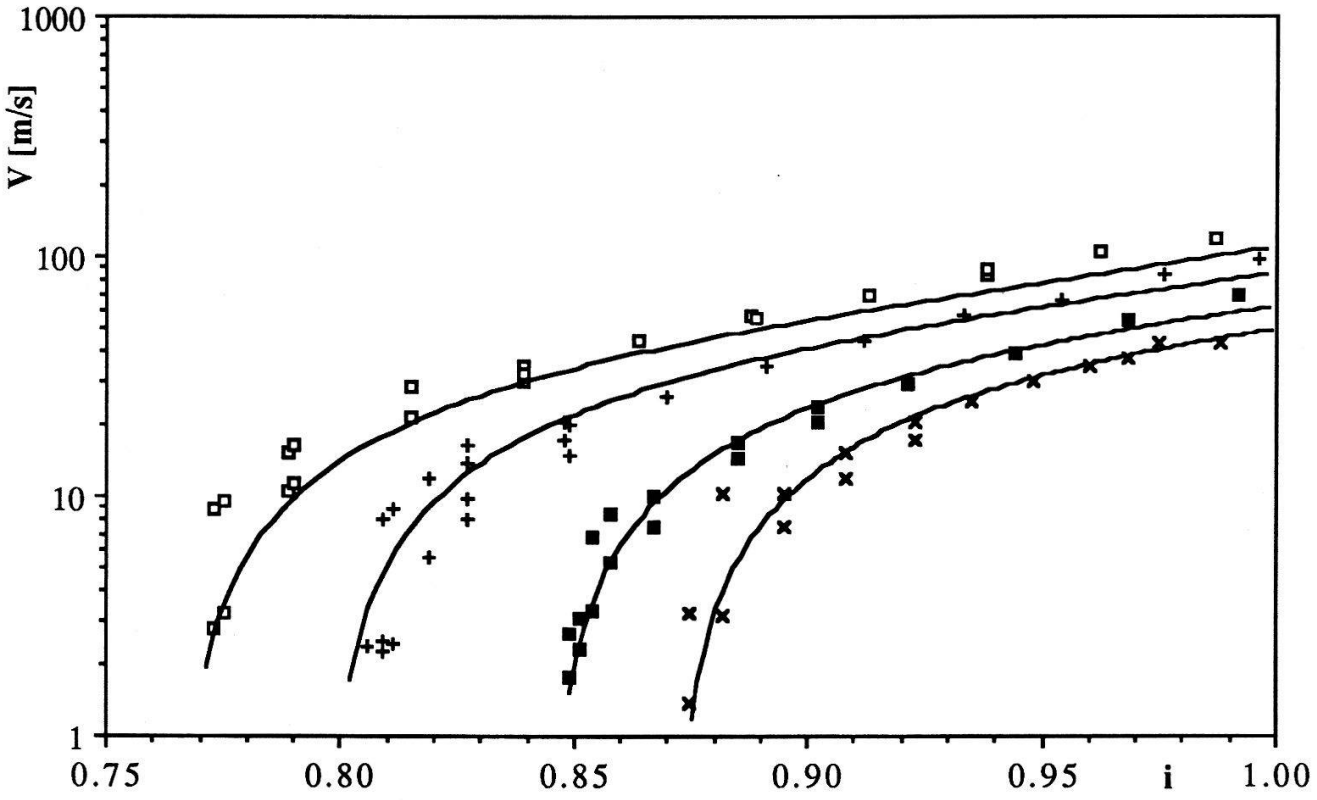

Fig 1 Measured and calculated normal propagating velocities, V, versus reduced current, i = I_s/I_c at different bath temperatures. Open□, 1.27 K; +, 1.54 K; closed□, 1.88 K; x, 2.12 K.

seen that a good agreement is obtained.

Figure 2 shows the deduced boundary thermal conductances, h, versus bath temperature, T_b, and the Kapitza boundary conductances for a tin sample [9].

5. Conclusion

A theory predicting the normal zone propagating velocity, V, dependence on the circulating current has been developed. The deduced boundary conductances

Table I Wire characteristics

Tb (K)	h (W/m^2 K)	I_c (A)$^+$	General data	
1.27	$7.12\ 10^3$	20.2	a (m)	$1.5\ 10^{-4}$
1.54	$9.14\ 10^3$	18.9	ρ (Ω m)	$3.4\ 10^{-9}$
1.88	$1.35\ 10^4$	16.7	C (J/m^3 K)	$43.6\ T_t^3$
2.12	$1.72\ 10^4$	15.1	K(W/m^2 K)	$7.18\ T_t$

$^+$: Critical Silsbee currents at the bath temperature T_b

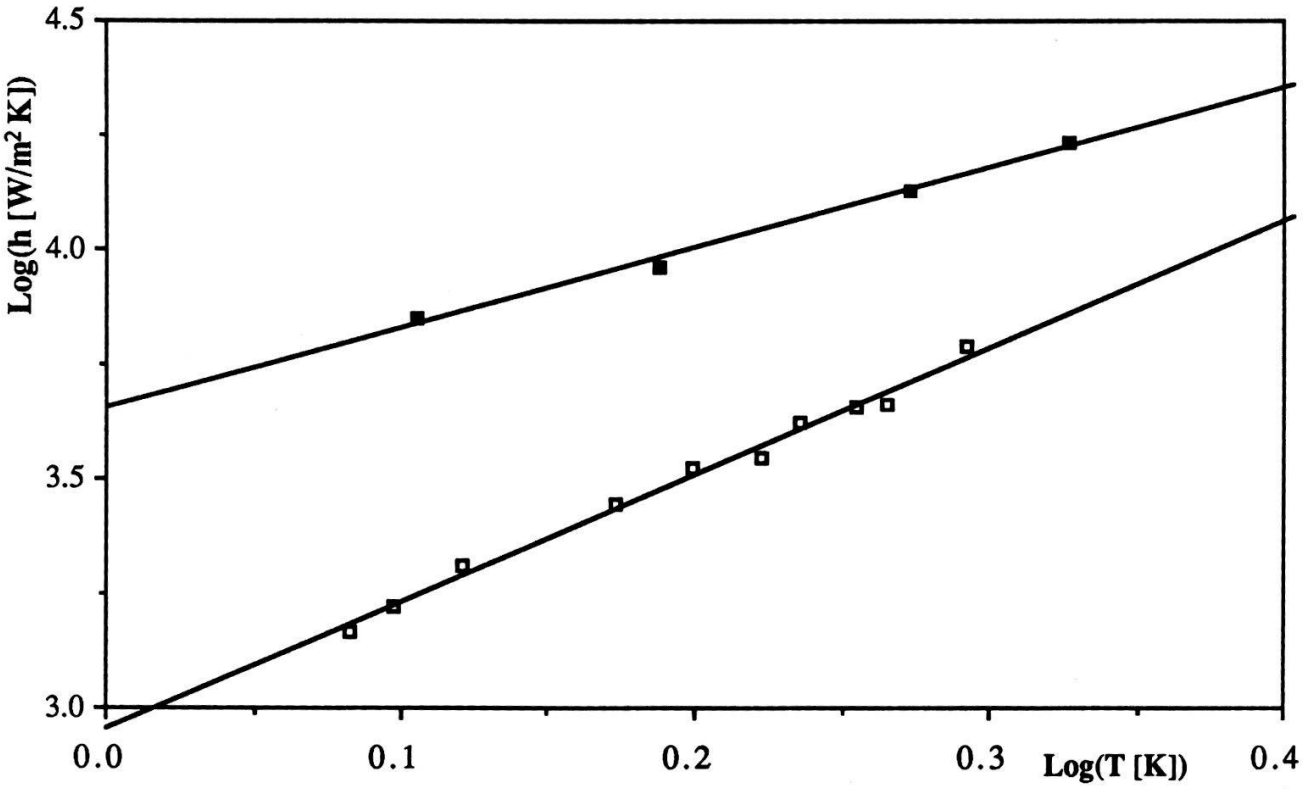

Fig 2 Thermal boundary conductance temperature dependence. Closed □, deduced boundary conductances $h = 4.5\ 10^3\ T^{1.75}$; open□, Kapitza boundary conductance [9] $h = 8.1\ 10^2\ T^{2.9}$.

follow a similar law to the calculated and observed Kapitza boundary conductances. Differences arise as the power transferred through the solid-liquid boundary, in a normal phase propagation process, is extremely high compared to the power levels employed for usual Kapitza resistance measurements [9].

This work was supported by the Swiss National Science Foundation.

6. References

[1] J. Casas and L. Rinderer, IEEE MAG-**23**, 1604 (1987)

[2] Yu. M. Lvovsky and M. O. Lutset, Cryogenics **22**, 581 and 639 (1982)

[3] L. Dresner, IEEE MAG-**19**, 328 (1979)

[4] H. H. J. ten Kate, H. Boschman, L. J. M. van de Klundert and references quoted therein, IEEE MAG-**23**, 1557 (1987)

[5] J. Casas and L. Rinderer, Jap. Appl. Phys. **26** suppl. 26-3,1597 (1987)

[6] J. Casas and J.-F. Loude, Cryogenics **27**, 379 (1987)

[7] E. Posada and L. Rinderer, J. Low Temp. Phys. **21**, 223 (1975)

[8] F. London, Superfluids **1** (Dover NY, 1961)

[9] K. Wey-Yen, Soviet Phys-JETP **15**, 635 (1962)

Helvetica Physica Acta
Vol. 61 (1988)

0018-0238/88/060845-04$1.50+0.20/0

High sensitive and fast photodetectors at 820 nm

M. Zirngibl, R. Sachot, W. Baer, M. Ilegems
Institut de micro- and optoélectronique, EPF Lausanne, 1015 Lausanne

An interdigitated metal-semiconductor-metal photodetector (MSM) with an indium tin oxide (ITO) metallization is shown to exhibit interesting properties in terms of gain and high speed response. ITO, which forms good Schottky contacts on GaAs, is transparent to light at 820 nm and acts as an antireflection layer. The MSM detectors are fabricated on Cr doped substrates by a simple one level lift-off technology to define the interdigitated Schottky barrier contacts. They show high sensitivity (7 A/W), which corresponds to an external gain of 10, high speed (FWHM > 100ps) and low dark current (5 nA or 0.012 mA/cm^2 at 5 V). Measurements of sensitivity as a function of the distance between the Schottky contact regions indicate that the gain is due to avalanche multiplication. This detector could find applications in optical telecommunication and optical readout systems.

Photodetectors are key elements in optical communication systems. Metal-semiconductor-metal detectors (MSM) are promizing candidates because of their simple fabrication and their high speed and gain. Their planar structure is compatible with integration of amplifiers like FET's. Compared to vertical detectors, the capacitance of a MSM is much lower for equal active area, so that high speed can be achieved with MSM's having relatively large areas. The coupling of light into the detector is also simplified. In spite of these advantages, there are few studies about MSM[1-8] and there is still a confusion about the physical origin of their gain.

We report the characteristics of MSM's with indium tin oxide (ITO) metallization and evaluate their speed of response and sensitivity as a function of the layout geometries.

The MSM's are fabricated on Cr-doped GaAs substrates by a conventional lift-

off technology. Their structure is interdigitated with an active area of 200x200 μm^2 (Fig. 1). The distance between fingers L and the finger width d range from 1.8 μm to 16 μm.

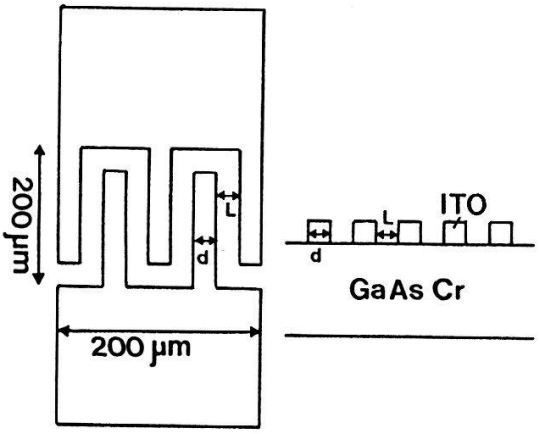

Fig. 1: Top view and cross section of a MSM photodetector. d and L range from 1.77 μm to 15.7 μm.

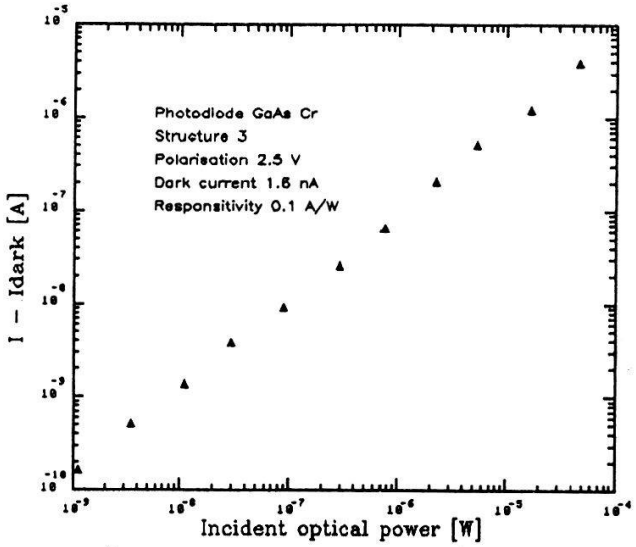

Fig. 2: Photocurrent versus incident optical power.

The ITO Schottky contacts are transparent to light at 820 nm and act as an antireflecting layer. The barrier height of ITO, measured on a n-doped GaAs layer, is 0.85 eV. This means that the dark current (5 nA at 10 V) is mostly governed by hole injection. An aluminium Schottky contact has lower dark current, but it shadows the active surface and decreases the sensitivity. The capacitance of the MSM's is given by the capacitance due to depletion width and the capacitance between the fingers. At high voltage close to punch-through the latter term dominates. Theoretical values[5] and measured values are in good agreement for all structures. For example, the calculated and measured capacitances of structure 1 (see Fig. 3) are 459 fF and 465 fF respectively.

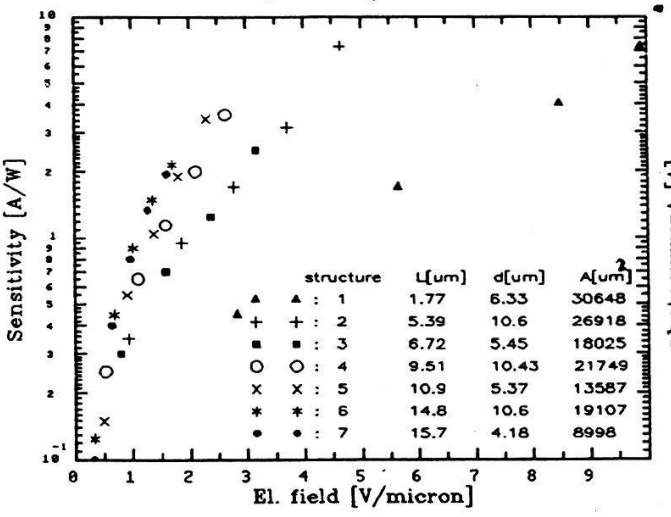

Fig. 3: Sensitivity of different structures versus the el. field.

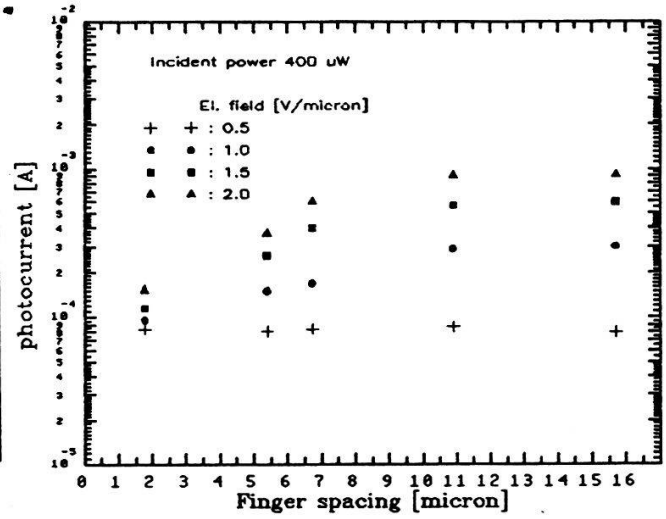

Fig. 4: Photocurrent versus distance between fingers for different el. fields.

Fig. 2 shows the linear dependence of the photocurrent on the incident optical power. Minimum detectable power is of the order of 10 nW. In Fig. 3 and 4 sensitivity and photocurrent of different structures are plotted versus the average value of the horizontal component of the electrical field E and the distance L between the Schottky contacts. The maximum sensitivity value achieved is 7 A/W. To our knowledge, this value is the highest reported for this kind of photodetector. Sensitivity increases with field and distance between fingers but it is independent of contact area. Devices operating with unity external quantum efficency should exhibit a maximum sensitivity of 0.66 A/W. Our devices thus show a gain over most of their operating range, which may be attributed to avalanche multiplication at high fields and/or to photoconductive gain mechanism [1]. Other possible mechanisms, such as Schottky barrier lowering[2,5,6], may be excluded because the gain does not exhibit any clear dependence on the Schottky contact area A.

An increase of gain with distance and field is typical for avalanche multiplication. At 0.5 V/um there is no ionization. Taking into account reflection losses, the photocurrent of 10^{-4} A corresponds to 100% internal quantum efficency at 0.4 mW optical input power. At higher electrical fields, the photocurrent increases with L and saturates above L = 10 μm. If we take a very simple model[10] which assumes an uniform field and equal hole and electron ionization rates, then the photocurrent I is proportional to the multiplication factor $M = 1/(1 - aL)$, where a is the ionization rate. This relation may explain the first part of the curve of Fig. 4 but it can not account for the observed current saturation. Even a more complicated model, including field dependent ionization rates and non uniform carrier generation, does not show current saturation. In Fig. 5 and 6 we plot photo- and dark current vesus L for low incident optical power. In this case, there is a multiplication of current even at 0.5 V/um and saturation is not observed. These curves can be fitted by the relation $I=I_{in}/(1-aL)$, where I_{in} and a are the fit parameters. I_{in}, which represents the primary photocurrent, is higher for 1.0 V/um than for 0.5 V/um. This must be due to a larger depletion width. From these results, we conclude that high current densities decrease the avalanche multiplication. The dark current does not behave in the same manner. Probably it is mostly governed by surface defects. Comparing to ionization rates found in literature[10], avalanche multiplication should not occur at field as low as 2 V/um so that there may be region between the Schottky contacts with higher fields. The ionization and saturation mechanism could also be related to the presence of a free surface.

Fig. 7 shows the response of a MSM (structure 1) to a short laser pulse. The FWHM is of about 250 ps. Taking into account the 240 ps FWHM of the laser, we

estimate a detector response less than 100 ps.

In conclusion, we have fabricated a high sensitive MSM with ITO Schottky contacts. Sensitivity measurements as a function of geometry indicate that the gain is due to avalanche multiplication. Further investigations are necessary to understand this ionization process. Our detector could find applications in optical telecommunication systems and optical readout systems because of its high speed and gain and its simple technology.

[1]C. W. Slayman and L. Figueroa, IEEE Electron device letters 5, 112 (1981)

[2]C. J. Wei, H.-J. Klein, H. Beneking, Electron. Lett. 17, 689 (1981)

[3]M. Ito, O. Wada, K. Nakai, T. Sakurai, IEEE Electron device letters 5, 531 (1984)

[4]H. Schumacher, P. Narozny, Ch Werres, H. Beneking, IEEE Electron device lettres 7, 26 (1986)

[5]M. Ito, O. Wada, IEEE J. Quant. Electron. 7, 1073 (1986)

[6]R. L. Robertson, idem, 1185 (1987)

[7]D. L. Rogers, IEEE Electron device letters 11, 600 (1986)

[8]D. K. W. Lam, R. I. MacDonald, J. P. Noad, B. A. Syrett, Trans. on elect. devices 5, 1057 (1987)

[9]D. K. Donald, S. Y. Wang, T. R. Ranganath, S. A. Newton, W. R. Trutna, Appl. Phys. Lett. 49, 567 (1986)

[10]J. Gowar. Optical Communication Systems, Prentice-Hall

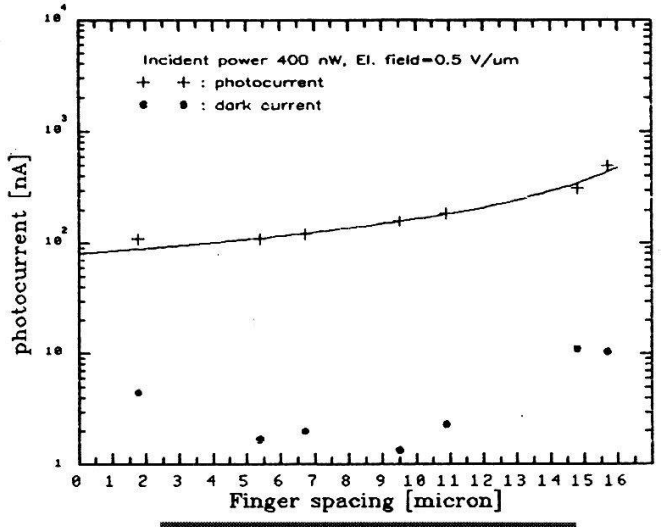

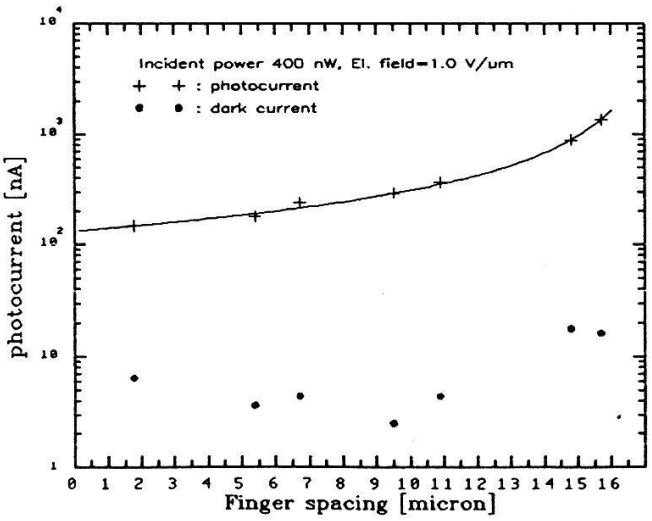

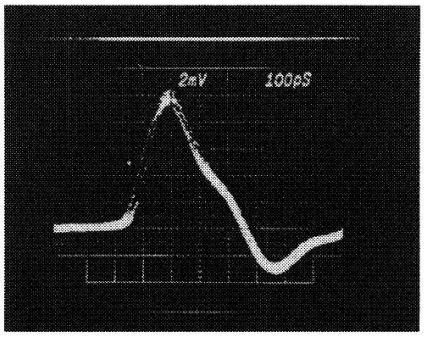

Fig. 5 and 6: Photocurrent and dark current as a function of distance between fingers for low optical incident power at constant field. The solid line represents the relation $I=I_{in}/(1-aL)$ with I_{in}= 80, 132 nA and a=0.052, 0.0575 um^{-1}.

Fig. 7: Response of a MSM structure 1 to an optical pulse of 240 ps FWHM. A bias voltage of 10 V is applied to the detector.

Helvetica Physica Acta
Vol. 61 (1988)
0018-0238/88/060849-04$1.50+0.20/0

Measurement and 1D-simulation of high electron mobility transistors

D. Théron, F. Lasagna, H.J. Bühlmann and M. Ilegems
Institut de micro- et optoélectronique, EPFL-Ecublens 1015 Lausanne

High electron mobility transistors (HEMT) are very promising devices for high frequency amplification and high speed VLSI circuits, because of the higher electronic mobility in the AlGaAs/GaAs heterostructure.

Physical models are used to describe their electrical behaviour and to optimize the structure. In those models a full analytical approach is in general of limited value because it cannot take into account all the relevant device parameters. On the other hand, a two-dimensional simulation of the device requires powerful programming techniques and does not always provide the physical insight necessary for device optimisation. In this contribution, we present a mixed approach to the problem which consists in solving numerically in one dimension the different equations of charge control and transport.

1) The model

The channel of a HEMT consists of a quasi two-dimensional electron gas confined at the interface between AlGaAs and GaAs. To calculate the dependence of the electron sheet density on the gate to channel voltage, a two equation system is used.

First, we solve one-dimensionally the Poisson equation in the AlGaAs layer. If that layer is completely depleted, the electric field F at the n^+AlGaAs/GaAs interface is given by (fig. 1) :

$$F = (1/d)\ (V_G + \Delta E_c + (E_F - E_W)/q - \phi_m + V_{p2}) \qquad (1.1)$$

where:

$$V_{p2} = qN_D\ (d-e)^2\ /2\varepsilon\ , \qquad (1.2)$$

d is the thickness of the AlGaAs layer, e is the thickness of the AlGaAs spacer, ε is the dielectric constant of the GaAs and AlGaAs (assumed to be equal), N_D is the doping level of the AlGaAs layer, ϕ_m is the Schottky barrier height, ΔE_c is the conduction band offset between AlGaAs and GaAs, E_F is the Fermi level at the interface, E_W is the energy of the well bottom.

Neglecting the fixed charges in GaAs and the electric field far from the interface, the electron sheet density is given by:

$$qn_s = \varepsilon F. \qquad (1.3)$$

Equations (1.1) and (1.3) give the dependence of n_s on V_G provided the variation of

E_F-E_W with n_s is known. In general, this dependence is neglected or is linearised [1]. Neglecting $E_F - E_W$, the following expression for the threshold voltage results :

$$V_T = \phi_m - \Delta E_c - V_{p2}. \quad (1.4)$$

We improve this approach by using a second set of equations which describes the evolution of the Fermi level with the electron sheet density : after integrating the Fermi-Dirac function for a two-dimensional system containing only one level at energy E_0, we get :

$$n_s = kT\,(m^*/\pi\hbar^2)\,\ln\,[1 + \exp\,((E_F - E_0)/kT)], \quad (1.5)$$

where m^* is the effective mass of the electrons in the channel.

Moreover, the resolution of Schrödinger equation for a triangular well gives the energy E_0:

$$E_0 - E_W = \gamma_0\,(\varepsilon F/q)^{2/3} = \gamma_0 n_s^{2/3}, \quad (1.6)$$

where γ_0 represents a numerical constant.

All these equations can be solved by dichotomy. The result is given on fig. 2.

In order to obtain the drain current I_D versus drain to source voltage of a HEMT, we use a transport equation which takes into account drift and diffusion current at the same time :

$$j = -n_s \mu\ \text{grad}\ E_{Fn} \quad (1.7)$$

μ : carrier mobility,

and the charge conservation equation which can be written for a stationary system:

$$\text{div}\ j = 0. \quad (1.8)$$

In principle, the first formula is only valid at low gradients. To describe more accurately the saturation, we assume the following relation for the mobility μ :

$$\mu = \mu_0/[1 + \mu_0 |\text{grad}E_W|/qv_s], \quad (1.9)$$

where v_s is the saturation velocity.

Equations (1.7) to (1.9) can be solved numerically using finite differences to obtain the current density j as a function of the potential drop V_{DS} between drain and source.

First, we define the grid of the channel between source and drain, with a step being smaller when going towards the drain. Then we determine the sheet carrier concentration at the beginning of the channel with the charge control model described previously. A field dependent source resistance can be included which creates a potential drop between the source and the first point of the channel.

Knowing the sheet density at the point h, $n_s(h)$, we search it by dichotomy at the point h+1 in order to get as current density the value j_{ref} given by :

$$j_{ref} = n_s(h)\,\mu_o/\{1 + [\mu_o/qv_s][\,|E_W(n_s(h+1)) - E_W(n_s(h+1))|\,]/[y(h+1)-y(h-1)]\,\}$$
$$* \,|E_{Fn}(n_s(h+1)) - E_{Fn}(n_s(h-1))|/[y(h+1)-y(h-1)] \qquad (1.10)$$

Knowing $n_s(h+1)$, we calculate $E_{Fn}(h+1)$ and $E_W(h+1)$ analytically and go to the next step until we get the drain end of the channel. Then the potential drop due to drain resistance can be taken into account in order to get the drain to source voltage.

2) **Results and discussion**

We have used this model to fit measured I_D - V_{DS} and I_D - V_G curves of HEMT with gate lengths of 8, 4 and 2 um. The most important four parameters to be fitted are N_D, d, μ_o and v_s. N_D and d are related through the threshold voltage. μ_o must be determined by drain current at low field (V_{DS} = 10 mV). v_s will influence the saturation current.

Therefore, before starting the simulation, we have to evaluate N_D or d. N_D is a priori most easily obtained because it can be related through epitaxial growth conditions to the doping level of the n^+GaAs cap layer grown on the AlGaAs layer. This level is measured by C-V. On the contrary, d is adjusted by the gate recess during processing and cannot be measured afterwards. It can also vary from one FET to another.

By C-V measurement, we estimate N_D between 5 and 6.10^{18} cm^{-3}. The AlGaAs layer thickness d can be deduced for each FET and the mobility is determined on the 8 um channel length FET. The results are presented on fig. 3.

Some interesting features of the model should be noted :

The mobility obtained by fitting the I_D-V_G curve is rather low for a two-dimensional electron gas. A larger mobility would be obtained if we assume a lower doping level N_D. That seems to indicate that not all the donors in AlGaAs are active, in agreement with other observations [2].

The model yields values for the serie resistance of a few ohm.mm representing the sum of the source to gate and gate to drain access resistances and contact resistance.

The description of current saturation is quite good because velocity saturation effects are included.

In conclusion, we have shown that the model presented here allows a satisfactory description of the static I_D-V_{DS} and I_D-V_{GS} curves over the normal range of operation of the device. For a more complete description, the model should be amended to include spreading of the electron gas in the channel at low carrier density, parallel conduction and gate leakage current.

references

[1] K. Lee et al., IEEE Trans. Electron Devices ED-30, 207 (1983)

[2] B. Vinter, Solid State Commun. 48, 151 (1983).

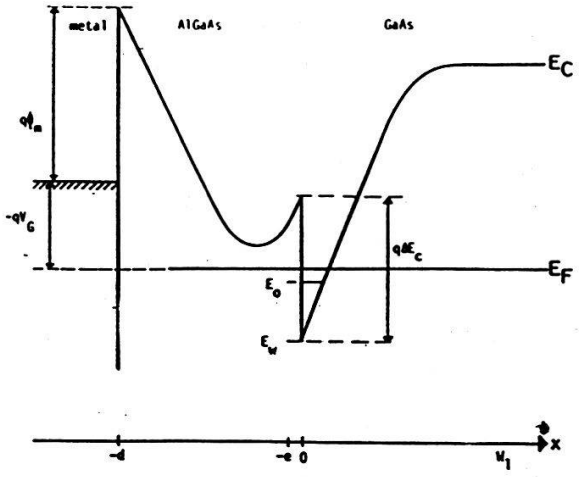

fig. 1 : Band structure of a two-dimensional electron gas with a Schottky gate.

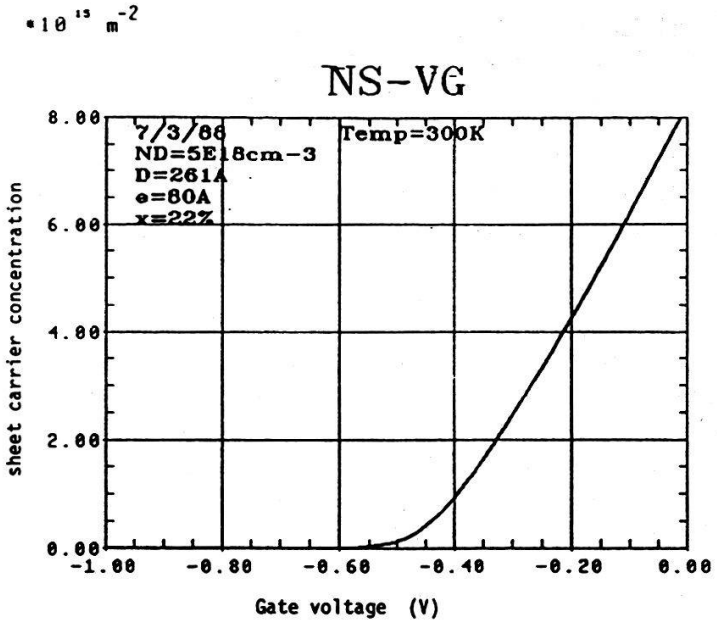

fig. 2 : carrier sheet concentration versus gate voltage.

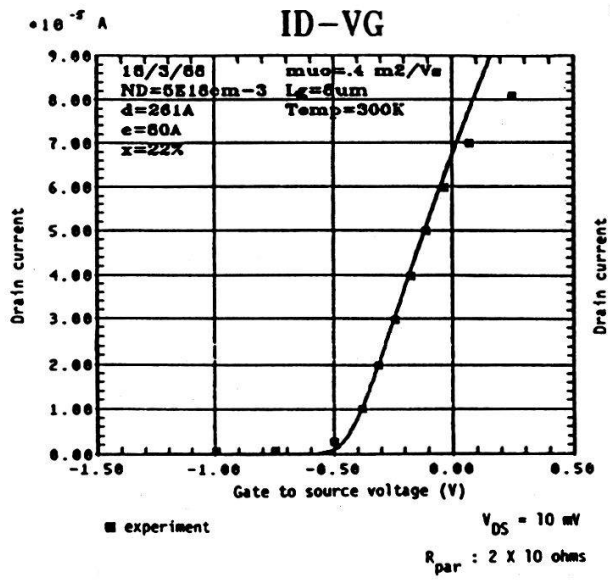

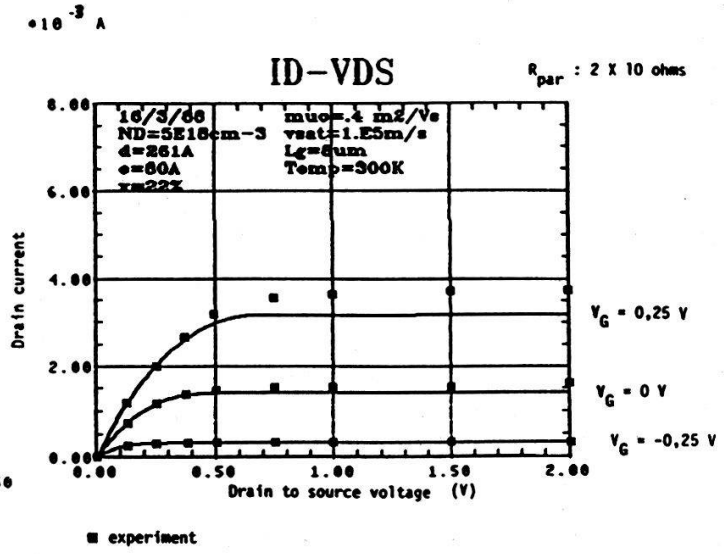

fig.3 : Drain current versus gate to source or drain to source voltage for an 8 μm channel length HEMT.

Helvetica Physica Acta
Vol. 61 (1988)
0018-0238/88/060853-04$1.50+0.20/0

INFLUENCE DE L'ENERGIE DES IONS ET DE LA TEMPERATURE DE L'OBJET LORS DE L'AMINCISSEMENT PAR BOMBARDEMENT IONIQUE DE GAAS

R. Spycher, F. Schmid et P.A. Buffat
EPFL-I2M, Inst. de Microscopie Electronique, CH-1015 Lausanne

Abstract: To provide High Resolution Electron Microscopy (HREM), the observed matter should be a thin film (less than 100 atoms). This way, ion beam milling is usually used for the thinning [1]. The effect of two of its parameters, the accelerating voltage of the ions and the specimen temperature during milling, were studied here for GaAs, in respect with irradiation damage and amorphous surface layer formation.

1. Introduction

Les tailles caractéristiques des circuits électroniques intégrés deviennent de plus en plus petites et se rapprochent des distances ou la nature discrète de la matière (structure à l'échelle de l'atome) intervient et modifie les propriétés utiles pour l'électronique. La microscopie électronique à haute résolution en transmission (HREM) permet d'observer les structures jusqu'au niveau des distances interatomiques. Cependant, pour garantir une observation fidèle, il faut que la partie de l'échantillon observée soit très fine (lame mince) pour éviter que les électrons soient absorbés. Dès que l'on veut obtenir de telles lames, plusieurs problèmes surgissent qui réduisent la qualité de l'image obtenue.

A partir d'un matériau massif (quelques mm^3), la préparation d'une lame mince comporte: un polissage mécanique jusqu'aux environs de 10-20 microns d'épaisseur, puis ensuite différentes méthodes sont possibles: attaque chimique, polissage électrochimique, bombardement ionique,... Dans le cas du bombardement ionique, les problèmes majeurs sont l'amorphisation en surface et l'implantation de défauts dans le cristal (boucles de dislocations ou agglomération de défauts ponctuels). Les dislocations et les défauts ponctuels vont superposer leur contraste à celui du cristal observé et la couche amorphe de surface va faire diffuser les électrons; ces deux phénomènes conduisent à une diminution du contraste déja faible de l'image. L'effet de deux paramètres de cette attaque sont examinés: la tension d'accélération des ions et la température de l'échantillon pendant le bombardement.

Lors d'un amincissement par bombardement ionique, les paramètres suivants interviennent: l'énergie des ions incidents, la température de l'échantillon bombardé, le courant débité par les deux canons et l'angle d'incidence des ions. Plusieurs études sur l'effet de la nature chimique des ions utilisés ont déjà été faites lors de l'amincissement des semiconducteurs tels que InP, CdTe, ZnS, ZnSe où il s'avère que le bombardement avec des ions d'iode ne crée pratiquement aucun défaut visible [2,3]. L'effet de différents ions utilisés (Ar^+, I^+, Xe^+, N^+) sur divers semiconducteurs est déjà abondamment discuté par Chew et Cullis [4]. L'étude de l'effet de l'angle d'incidence lors de l'attaque pour du silicium a été faite par Bulle-Lieuwma [5],

mais dans le cas du GaAs, aucune étude systématique n'a été entreprise sur l'influence des paramètres tels l'énergie des ions et la température de l'échantillon.

2. Méthodes expérimentales

A partir d'un disque de GaAs orienté (110), des petites plaquettes de 10mm de long et de 2.5mm de large sont obtenues par clivage. Plusieurs paires de plaquettes sont ensuite bombardées sur une face avec des ions d'argon avec les conditions suivantes : une installation Gatan model 600 dual ion mill est utilisée, la densité de courant débité est de 0.1 mA par mm^2, l'incidence rasante du faisceau est de 20°; la température de l'échantillon et la tension d'accélération des ions sont elles variables pour chacune des paires de plaquettes.

Pour observer valablement l'effet des conditions du bombardement, il faut que les plaquettes ainsi attaquées soient ensuite traitées rapidement afin d'éviter une oxydation au contact de l'air [6]. Pour observer l'effet de cette première attaque en microscopie électronique à transmission, il faut réaliser une coupe transverse [7] de la région attaquée. Les deux plaquettes identiques sont collées face contre face, introduites dans une tige métallique (alliage inoxydable et non-ferromagnétique Arcap) puis tronçonnées transversalement pour obtenir ensuite des échantillons qui seront amincis par les voies traditionnelles de polissage mécanique puis d'attaque par bombardement ionique avec les conditions standard (densité de courant de 0.2 mA/mm^2, 20° d'incidence rasante, 5 kV et température ambiante).

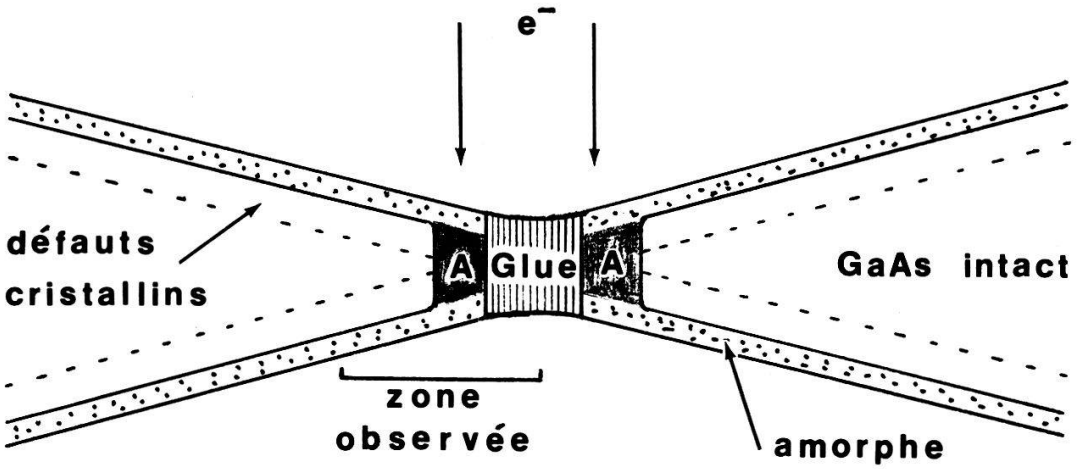

Figure 1: Lame mince obtenue par coupe transverse. **A** indique la couche amorphisée lors de la première attaque

Les observations sont ensuite réalisées sur un microscope Philips EM 430 SuperTwin avec un porte échantillon double tilt et un pouvoir de résolution ponctuelle meilleure que 0.2 nm. Pour limiter les dégâts dus au faisceau des électrons et aux ions dans la colonne du microscope (contamination de surface et

dégâts d'irradiation), les clichés ont dus être obtenus en moins d'une demi-heure d'exposition de l'échantillon au faisceau d'électrons. De chaque couple de conditions température de l'échantillon/tension des ions, deux coupes transverses ont été observées et sur chacune d'elle le maximum de plages minces ou la haute résolution était possible pour distinguer les colonnes d'atomes de la couche amorphe. Deux plaquettes non-bombardées ont de meme été préparées en coupe transverse pour permettre de comparer une surface attaquée avec une surface intacte.

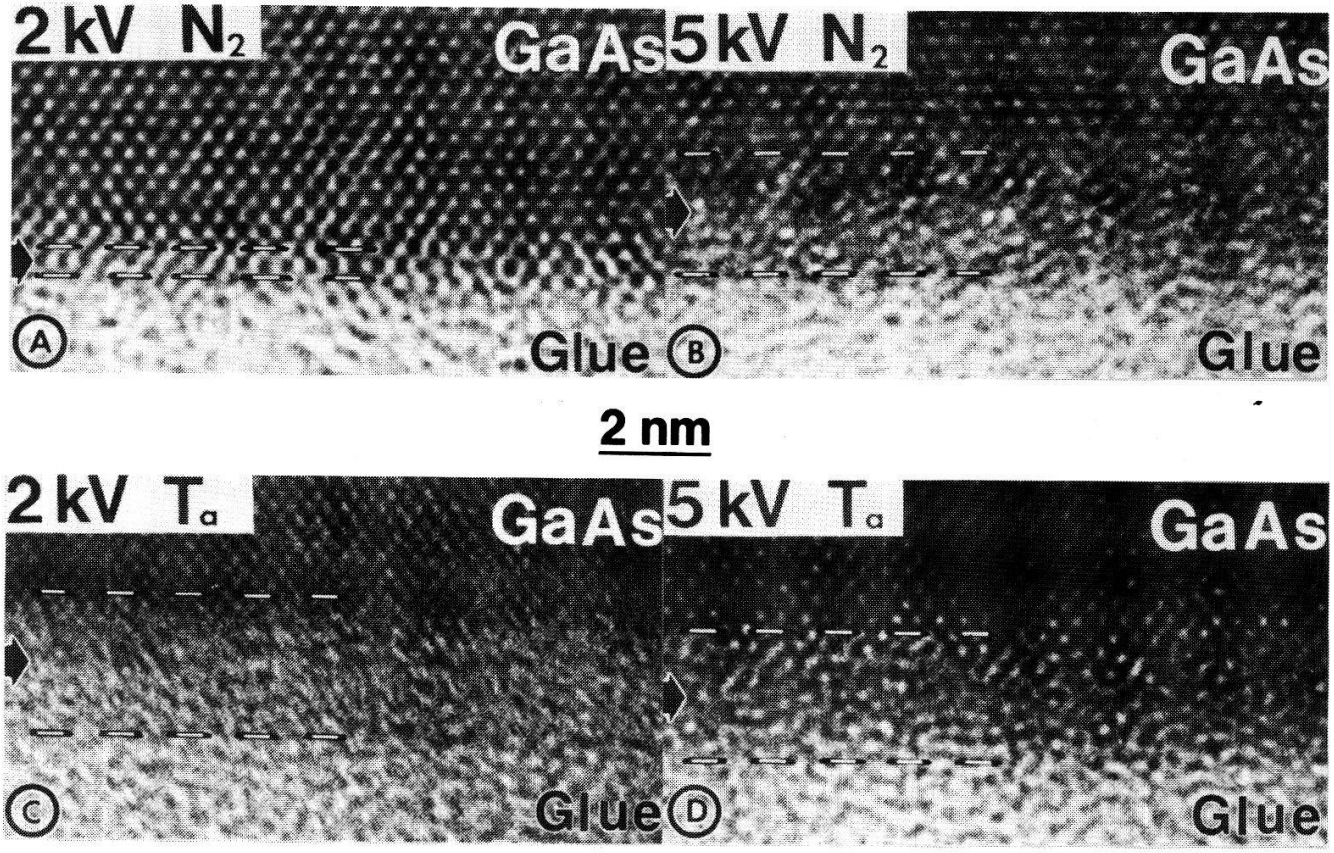

Figure 2: Images Haute Résolution de coupes transverses de surfaces de GaAs attaquées avec les conditions : incidence rasante du faisceau 20°, densité de courant de 0.1 mA/mm^2 et les tension d'accélération des ions et les températures suivantes: A) 2kV / 77°K B) 5kV / 77°K C) 2kV / 300°K D) 5kV / 300°K.

3. Discussion des résultats

Les clichés de la Figure 2. présentent une image haute résolution de la coupe transverse faite pour chacune des conditions de l'attaque par bombardement ionique. Sur chaque cliché, la flèche indique la partie amorphisée en surface de l'échantillon. L'épaisseur de cette couche est la suivante: moins de 0.5 nm pour le cas A), 2.0 nm pour le cas B), 2.3 nm pour le cas C) et 2.2 nm pour le cas D).

Plus la couche d'amorphe en surface est épaisse et plus la diffusion des électrons est importante ainsi que la création d'électrons inélastiques, ces deux phénomènes entrainent une perte de cohérence du faisceau qui diminue le contraste de l'image haute résolution; cette couche amorphe doit donc être la plus mince possible, voire inexistante. Cette condition est réalisée dans le cas de GaAs lorsque l'énergie des ions incidents est faible (2kV) et que l'échantillon bombardé est refroidi à la température de l'azote liquide.

La Figure 3. représente une image haute résolution d'une coupe transverse de cristal parfait de GaAs. Sur cette figure, le réseau est régulier jusqu'à la dernière couche d'atomes avec toutefois un contraste différent sur une couche, dû à la rugosité de la surface (1 à 2 couches d'atomes) qui provoque des variations importantes de l'épaisseur traversée par les électrons et donc des changements de contraste. La comparaison entre la Figure 2. A) et la Figure 3. montre bien que le cristal est quasi intact jusqu'à la surface pour des conditions bien choisies.

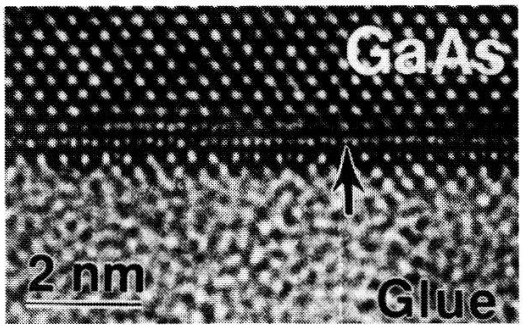

Figure 3: GaAs: cristal parfait.

4. Conclusion

Pour la préparation par bombardement ionique avec des ions d'argon de semiconducteurs destinés à être observés par microscopie à haute résolution, l'attaque peut être faite avec un minimum de dégats au cristal si l'on travaille avec un échantillon le plus froid possible et si l'on diminue l'énergie des ions incidents au maximum, c'est-à-dire dans la mesure où le temps de l'attaque ne devient pas prohibitif, car celui-ci dépend fortement de l'énergie des ions incidents. La couche amorphe en surface peut bien être limitée, mais les défauts cristallins sous la surface restent encore une limitation à l'interprétation. Cette recherche devrait se poursuivre par une quantification de ces défauts et une tentative de mise au point d'une méthode qui permettrait de s'en affranchir. Les remerciement les meilleurs vont à Monsieur B. Garoni pour sa patience lors de divers travaux nécessaire pour ce travail.

5. Références

[1] R. Castaing, Rev. Met. **52**(1955)669.
[2] N.G. Chew and A.G. Cullis, Appl. Phys. Lett., **44**(1983)142.
[3] A.G. Cullis, N.G. Chew and J.L. Hutchison, Ultramicroscopy, **17**(1985)203.
[4] N.G. Chew and A.G. Cullis, Ultramicroscopy, **23**(1987)175.
[5] C.W.T. Bulle-Lieuwma and P.C. Zalm, Surface and Interface Analysis, ECASIA, 1986.
[6] P. Ruterana, Thèse de Docteur ès Sciences, Université de Caen, (1987)pp 3-29 à 3-41.
[7] M.S. Abrahams and C.J. Buiocchi, J. Appl. Phys., **45**(1974)3315.

Helvetica Physica Acta
Vol. 61 (1988)

0018-0238/88/060857-04$1.50+0.20/0

THE SUPERCOOLING OF METAL DROPLETS WITH HIGH MELTING POINT

V. Soares, E. Meyer* and L. Rinderer
Institut de Physique Expérimentale, Université de Lausanne
CH-1015 LAUSANNE, Switzerland

Abstract: Metal droplets of high melting point have been supercooled using the technique of dendritic crystal growth and their limit temperature to the supercooling has been measured by a stereophotocalorimetric method in which photographic density is calibrated against temperature. The results obtained for the maximum supercooling are analysed under the existing models of nucleation.

1. Introduction.

In recent years the nucleation phenomenon has been object of controversies if it is either an isothermal phenomenon or an adiabatic one.

According to classical (isothermal) theory of nucleation the limit temperature to the supercooling of liquids was believed to be equivalent to about $0.82T_M$ where T_M is the absolute melting temperature and related to the onset of a homogeneous nucleation process(1). However, the latest results(2) for this limit temperature are almost twice as small as those indicated by earlier works. A recent adiabatic theory of nucleation predicts the existence of a limit temperature to the supercooling of liquids , in agreement with the latest experimental results to the supercooling of metals with low melting point(3).

We present preliminary measurements of the limit temperature to the supercooling of metal droplets with high melting point produced by the technique of dendritic crystal growth and using a stereophotocalorimetric method in which photographic density is calibrated against temperature. These limit temperature have been analysed using both isothermal and adiabatic theories.

2. Experimental Procedure.

The technique of dendritic crystal growth has been described previously(4). In brief, a metalic wire is supported by electrodes in a vacuum chamber and surrounded by a helium atmosphere at 60KPa. When the wire is overloaded by a high current from a discharge condenser, then it is liquefied and liquid metal droplets are produced and ejected in the space. After this, they turn downwards and are cooled by the helium gas and by radiation. This can be seen by the continuous changing of luminosity on the Figure 1a. The points 1 and 2 are the points when solidification via dendritic growth occurred(4,5).

The experimental determination of the temperature of the metal droplets was made by using a stereophotographic apparatus as that one represented in Figure 1b which can produce two simultaneous photos of the whole phenomenon as is shown in Figure 1a. On each objectif there exists an interference filter which makes the two identical images on the film at two different colors.

Considering the Planck's equation applies here and including in this equation the emissivity of the metal dependent on temperature and wavelength(6), and the coefficient of transmittance of each filter, we calculated the ratio of intensities of radiation from the surface of the metal to each temperature.

From the film, the locus of each droplet was scanned using a photoelectric densitometer and the measured transmittance could be converted to photographic density. Admiting the validity of the Beer's law, which generally has been the case to black-and-white films, the ratio between the densities at two given wavelengths will be equal to the ratio between the intensities of radiation at these same wavelengths at a fixed temperature.

The droplets were photographed on Tech Pan 2415 films through a green and red filters in the stereophotographic apparatus and both of them were attached to a single lens reflex camera. Many preliminary experiments were performed to stablish the optimum photographic conditions.

The procedure above was verified measuring the melting point of the metals and it was found to be not so sensitive to small variations of the emissivity.

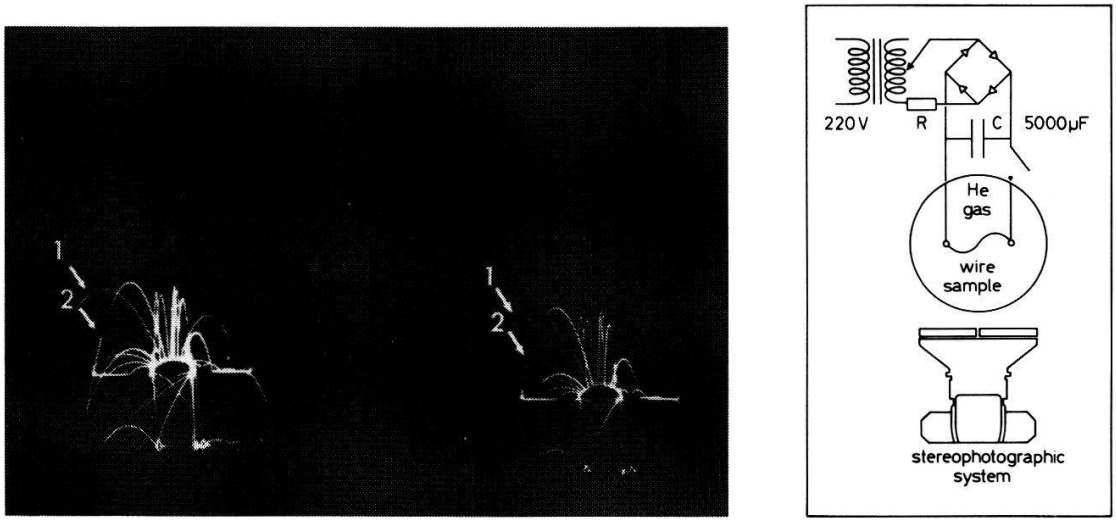

(a) (b)

Figure 1. (a) Time exposure of freely falling molten tantalum droplets, cooling in helium at subatmospheric pressure, photographed by their own luminosity. Liquid-solid transitions are indicated by arrows; (b) Experimental set-up used to produce and photograph the droplets.

3. Results.

If it can be assumed that the supercoolings are produced only by radiation, the ratio of the densities obtained on the films gives a typical surface temperature versus time behavior showed in Figure 2a for molten tantalum droplets. This Figure represents the temperature just before, during, and just after the liquid-solid transition to points like those showed in Figure 1a. On this characteristics we can see at the transition point a jumping of temperature. This sudden brightenning has been observed repeatedly in metals as tantalum, tungsten, molybden and niobium during our experiments.

The limit temperature to the supercooling of these metals has been determined and the ratio of this temperature to the melting temperature of these respective metals, represented in Figure 2b, are in agreement with the values predicted by the adiabatic theory of nucleation. Our results also do indicate the classical limit of $0.82T_M$ should not be regarded as a firm limit. Some authors(7) using the classical theory recalculated a new limit to the supercooling and found a value equal to $0.44T_M$. If this prediction is the correct one all the experimental results obtained until now should be considered as points of heterogeneous nucleation.

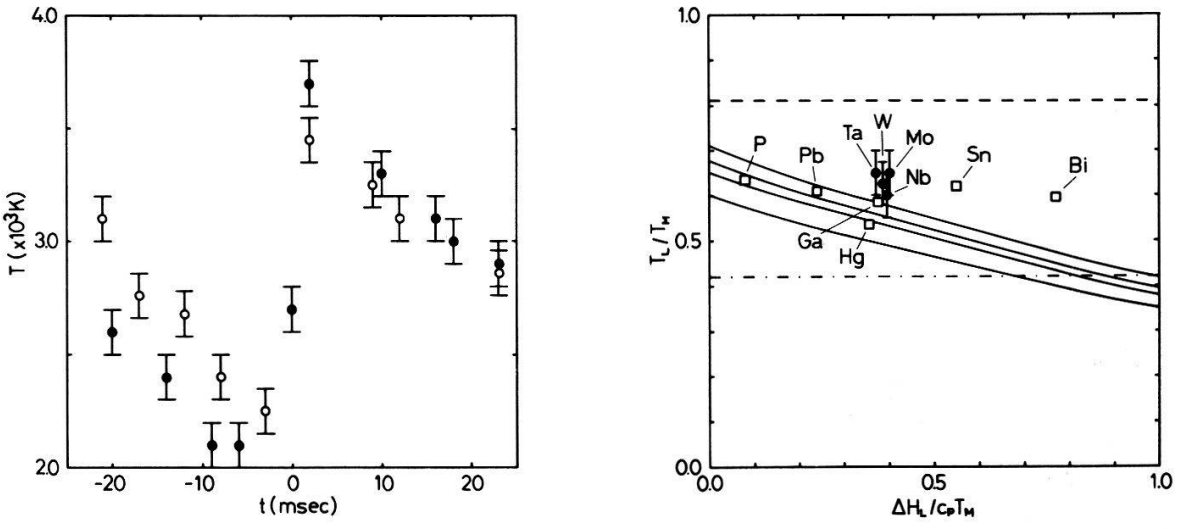

(a) (b)

Figure 2. (a) Surface temperature T vs time for two different molten tantalum droplets. The time scale was normalized to the instant of the jumping in the surface temperature of the droplets; (b) The limit temperature T_L is shown as a function of the dimensioless parameter $\Delta H_L/c_p T_M$, where ΔH_L is the latent heat and c_p is the specific heat of the material at the melting point. Dashed curve is from classical theory of nucleation and chained is also from the classical theory with some modifications. Continuous lines are obtained from adiabatic theory, where the last line represents the true limit to the supercooling of the liquid.

4. Conclusion.

Measurements of limit temperature to the supercooling of metals with high melting point are presented. These measurements suggest the nucleation phenomenon occurs adiabatically instead to be isothermal as predicted by the classical theory. However, doing some modifications on the various parameters of the classical theory one obtains a new lower limit to the supercooling that should indicate all the experimental limits measured until now should be points of heterogeneous nucleation. As yet it has not been possible to decide between the two theories and more experimental and theoretical work is necessary before the complete characterization of the process.

Aknowledgements: The authors thank the institutions Fonds National de la Recherche Scientifique and Conselho Nacional de Desenvolvimento Científico e Tecnológico for the financial support.

5. References.

(1) D. Turnbull, J. App. Phys., 21, 1022 (1950)
(2) J. Perepezko in 'Rapid Solidification Processing - Principles and Technologies', M. Cohen, B. H. Kear, and R. Mehrabian (eds.), Claitor's, LA, 1980
(3) E. Meyer, J. Crystal Growth, 74, 425 (1986); J. Crystal Growth, 76, 525 (1986)
(4) E. Meyer and L. Rinderer, J. Crystal Growth, 28, 199 (1975)
(5) L. S. Nelson, Nature, 207, 741 (1965)
(6) Y. S. Touloukian and D. P. de Witt (eds.), 'Thermophysical Properties of Matter', V.7, IFI/Plenum, NY,1970
(7) H. B. Singh and A. Holz, Solid State Comm., 45, 985 (1983)

*Permanent address: Instituto de Física - UFRJ, RJ-21945, Brazil

Helvetica Physica Acta
Vol. 61 (1988)

0018-0238/88/060861-04$1.50+0.20/0

SYNTHESIS OF Y - Ba - Cu - O THIN FILMS BY RF MAGNETRON SPUTTERING

M. Akinaga*, D. Abukay and L. Rinderer, Institut de Physique Expérimentale, Université de Lausanne, CH-1015 Lausanne-Dorigny, Suisse.

Abstract: We have prepared high-T_c $YBa_2Cu_3O_{7-\delta}$ films by RF magnetron sputtering. The temperature dependence of the electrical resistivity of these films have been measured in detail. The sample deposited onto the cooled substrate showed the I-V characteristics due to superconducting weak link.

1. Introduction

Thin film preparation of high-T_c superconducting ceramics is very important from the standpoint of its application to superconducting electronics. The function of such fabricated film devices as microbridge and so on is based on the superconducting weak link (1). In this paper we would like to report the synthesis of the sample of $YBa_2Cu_3O_{7-\delta}$ and the results due to the superconducting weak link.

2. Sample preparation

Thin films of $YBa_2Cu_3O_{7-\delta}$ were deposited onto the substrates of polished $SrTiO_3$, MgO and sapphire by RF magnetron sputtering. Targets were made by mixing the prescribed amount of powders of Y_2O_3, BaO and CuO, pressing these mixtures into a disk of 60 mm diameter and 5 mm thick, sintering the disk at 945 ^oC for 8 hours in air, recrushing it into powder. We repeated this process two times to get a final target with the composition (Y:Ba:Cu) ~ (1:2:3).

Sputtering was carried out under the conditions: substrate temperature 20 (cooled) ~650 ^oC; Ar gas pressure $2x10^{-3}$ ~ $4x10^{-2}$ Torr. The samples were annealed in a pure oxygen atmosphere or oxygen flow at 700 ~950 ^oC. In Fig. 1 the scanning electron micrographs of thin film surfaces before and after annealing are shown together with the composition analysis by EPMA. It is clear that as-deposited film is amorphous and

---

* On leave from Department of Physics, Fukuoka University of Education, Fukuoka 811-41, Japan.

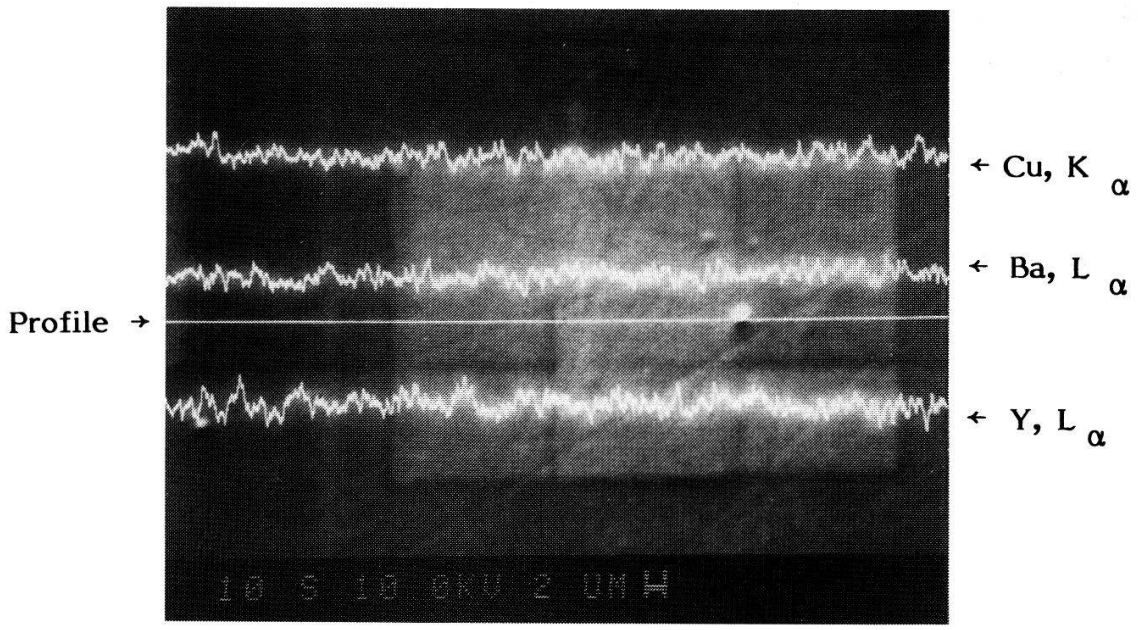

(a)

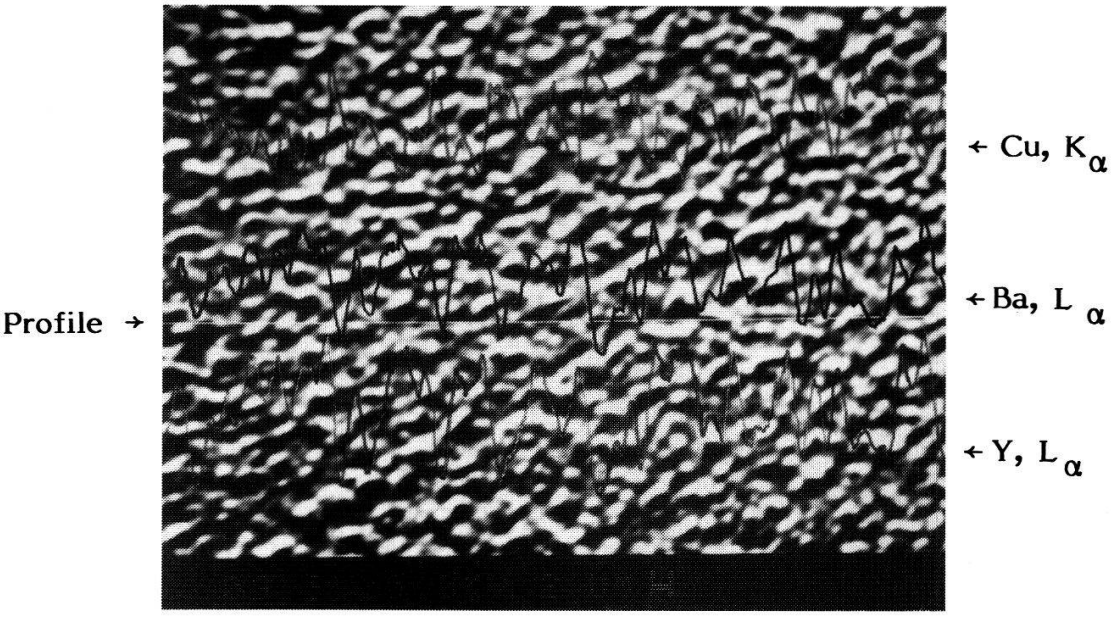

(b)

Fig. 1. The scanning electron micrographs of thin film surfaces together with composition analysis by EPMA. The scale for 2 μm is indicated below the photograph. (a) as-deposited, (b) after annealing.

the compositions are homogeneous, but annealed one contains crystallized grains with periodic compositions.

3. Experimental results

The electrical resistance of many samples were measured by usual four-probe method in detail. The samples deposited onto hot substrates showed the usual temperature dependence as reported (2) and the films epitaxially grown on $SrTiO_3$ substrates showed much better superconductive properties than those on MgO and sapphire substrates.

But the sample deposited onto the water-cooled $SrTiO_3$ substrate showed the interesting results. As shown in Fig. 2, the resistance increases gradually upon cooling from room temperature but at 170~ 180 K (indicated by arrow in the figure) it takes a turn to gradual decreasing before undergoing the conventional transition. It is very different from usual metalic or semiconductive behavior. This behavior of resistance above conventional transition temperature looks qualitatively same, except the absolute value of the characteristic temperature, as one due to superconductive percolation in A-15 Nb_3Ge (3).

We have clearly observed the I-V characteristics due to superconducting weak link

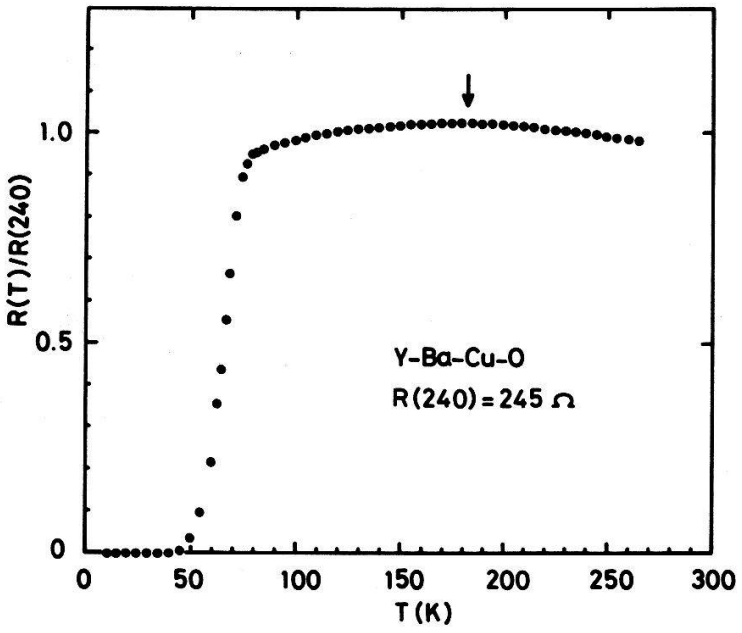

Fig. 2. Temperature dependence of resistance ratio for the sample deposited on a water-cooled $SrTiO_3$ substrate.

in the same sample as in Fig. 2, as shown in Fig. 3, where the excess current holds about 10 mA at T = 40.0 K. We did not artificially make any structures in film where Josephson effect can take place. Then this weak link in the sample is " natural " one. The grain boundary like one shown in Fig. 1 (b) seems to play a dominant role in such a superconducting weak link.

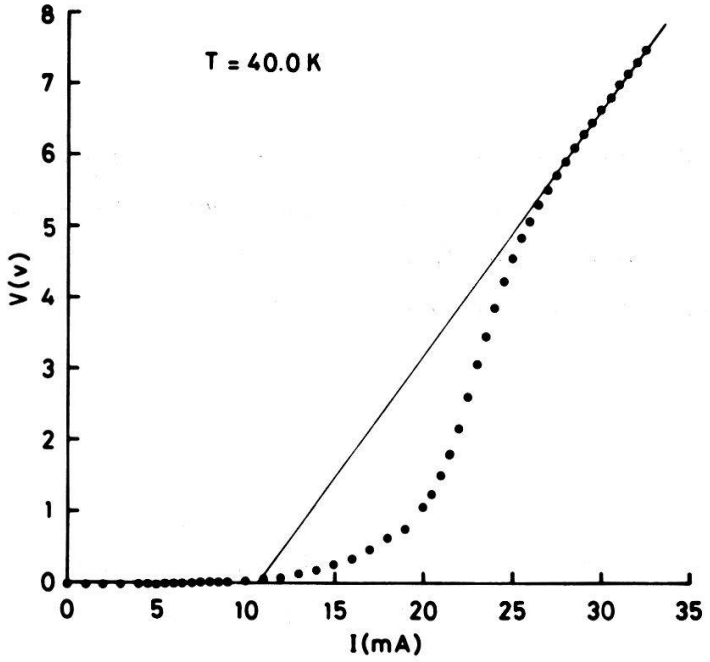

Fig. 3. I-V characteristics of $YBa_2Cu_3O_{7-\delta}$ film at T = 40.0 K. The excess current holds about 10 mA.

Acknowledgement

The authors would like to acknowledge gratefully Prof. T. Aomine's valuable discussions and encouragement. They also express thanks to Mr. G. Burri for his excellent work on the analysis of the samples. They are also indebted to the Fonds National Suisse de la Recherche Scientifique for financial support.

References

(1) K.K. Likharev, Rev. Mod. Phys. 51, 101 (1979).

(2) for example, O. Michikami et al., Jpn. J. Appl. Phys. 26, L1199 (1987).

(3) M. Akinaga, Jpn. J. Appl. Phys. 26, sup. 26-3, 1343 (1987).

Helvetica Physica Acta
Vol. 61 (1988)

0018-0238/88/060865-04$1.50+0.20/0

THE THIN FILMS OF $Y_1Ba_2Cu_3O_{7-\delta}$ IN A MAGNETIC FIELD

D. Abukay, M. Akinaga and L. Rinderer, Institut de Physique Expérimentale
Université de Lausanne, 1015 Dorigny- Lausanne, Switzerland

Abstract: The resistive transitions of the thin films of $Y_1Ba_2Cu_3O_{7-\delta}$ (YBCO) are studied in the presence of a magnetic field, ranging over 0-4.4 kG and in both parallel and perpendicular to the plane of the film. Only in the perpendicular direction a significant effect is observed at a field intensity of 3 kgauss.

1. Introduction

After the discovery of high-T_c superconductivity in the Cu-O perovskites much effort has been concentrated on the understanding of their superconductivity (1). These substances are found in a granular form in which the grains are coupled together by the Josephson tunneling mechanism. This feature is thought to give rise to a superconducting glass state, which is in a close analogy to the spin-glass state (2,3). In this communication, we present our results from a study which is carried out to investigate such a state in the thin films of YBCO.

2. Sample preparation

The thin film samples used in this study are prepared by deposition by rf-magnetron sputtering from a stoichiometric YBCO target. The target was prepared by mixing the powders of Y_2O_3, BaO and CuO in their appropriate proportions in an agate with pestle and then reacting at 900°C for 6 hours in air. After pressing and sintering at 950°C for 10 hours a final heating at 900°C in O_2-flow was added. The sputtering conditions were as following. The target-substrate distance was 38 mm and the background pressure was better than 10^{-6} mbar. During the sputtering the argon pressure was kept at 3-4 x 10^{-2} mbar and the rf-power was 100 watts. A deposition rate of 18 nm/min was achieved on

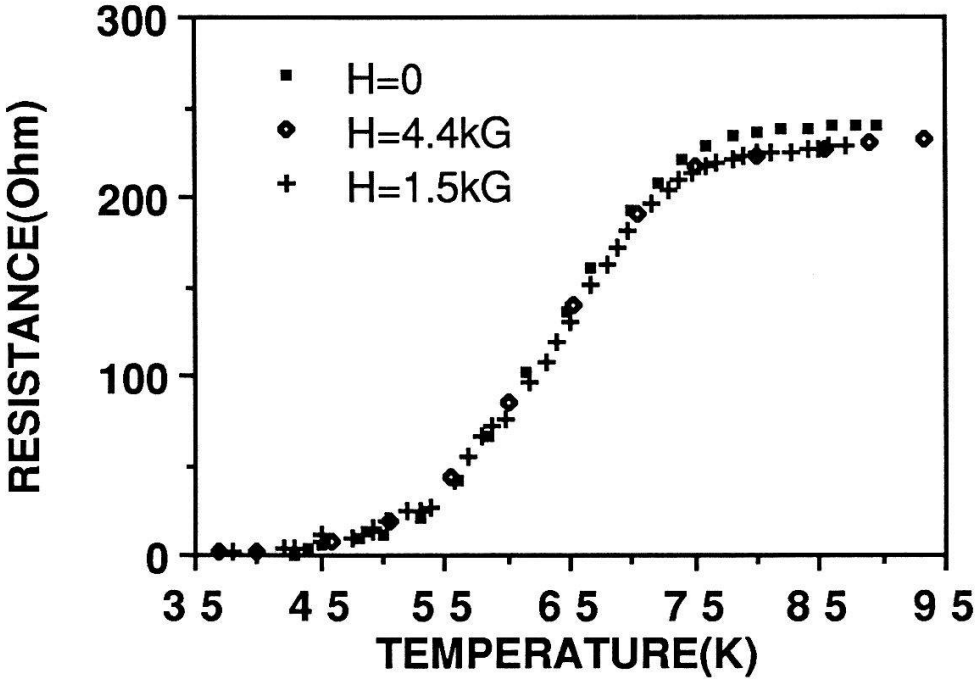

Figure 1. The transition curve of the thin film of YBCO in a magnetic field parallel to the plane of the film and the current.

to the <1 0 0> cut single crystal $SrTiO_3$ substrates. After many trials a temperature range of 800-820°C for the post treatment in O_2-atmospher with a cooling rate of 50°/h is found the most convenient.

3. Experimental results and discussion

The electrical resistance of the thin films were measured by 4-probe dc method. The sample current was 1 mA, corresponding to a current density of about 10 A/cm^2. The temperature was monitored from a carbon-glass thermometer. The direction of the magnetic field was set both in parallel and perpendicular to the plane of the film. In the parallel case the direction of the current was not of importance. The samples were cooled down either under the magnetic field and warmed up without it or both cycled in the presence of the field. In all these cases there found no significant effect of the field on the resistive transition curves. In Fig.1, the results of these measurements are shown up to the field intensity of 4.4 kgauss in the parallel direction. For the perpendicular direction again the resistive transitions were cycled in the presence of the field or without it.Theresults of these measurements are shown in Fig.2. It is clear from these

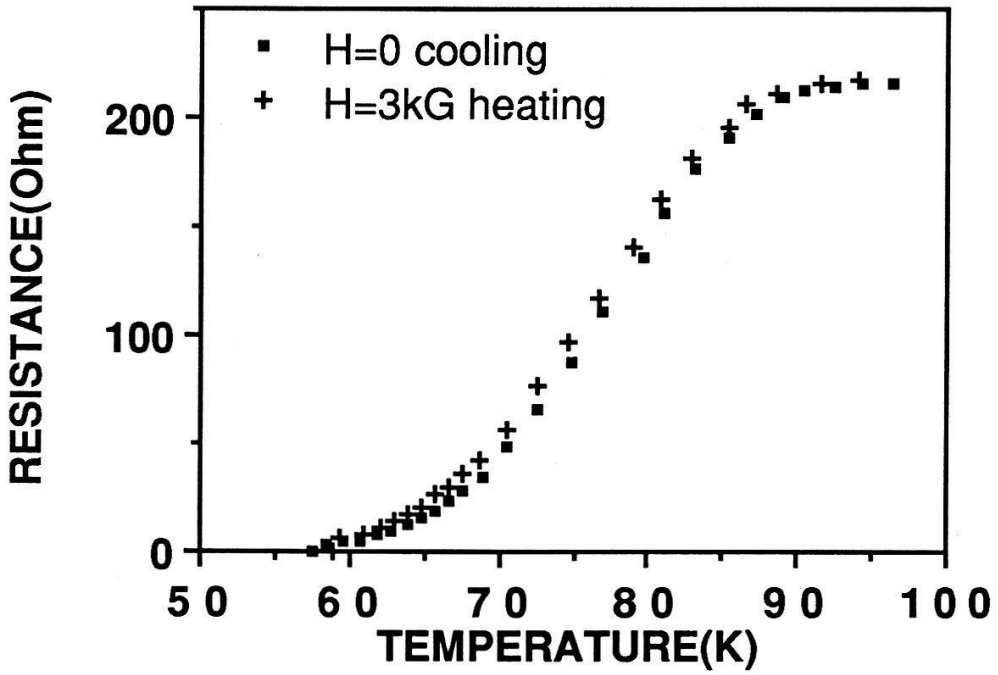

Figure 2. The resistive transition curves of the thin film sample cooled down without a magnetic field and heated up in the presence of a magnetic field of 3kgauss.

results that the effect of low magnetic fields is negligible or very small, even at a high value like 4.4 kgauss. We have also found no hysteretic behavior on these curves or any flux trap cases either, which are observable on the bulk samples. There, the superconducting grains are coupled into closed loops and these support screening currents in response to an external field. The supercurrent loops are analogous to the magnetic moments in a spin-glass. One of the essential features of this state is the difference in field-cooled and zero-field-cooled responses. In our work we have found no indication of any such responses at all. But, contrary to all, we have found no effect on the transition curves in the field direction parallel to the films and a slight shift in the transition curves only at 3 kgauss and perpendicular to the sample plane. A magnetic field acts in two ways on the conduction electrons. It changes their motion by forcing them into cyclotron orbits and it acts on their spin via the electron magnetic moment. The experiences with the classical superconductors have shown that both effects are unfavourable to the formation of Cooper pairs and hence superconductivity. In most samples it is the effect of the magnetic field on the electron orbits which supresses superconductivity. However, if the coherence length, ξ_0, can be made smaller and the electron

mean free path, l , is reduced sufficiently then the effect of the magnetic field via its influence on the electron motion can be made very small. One of the striking difference between the classical superconductors and the new ones is that the very short coherence length is found in the later ones, which is at the order of a lattice constant of their unit cell. This may provide a possible explanation why we have such a small effect of the magnetic field on these samples.

4. Conclusion

We have studied the resistive transition of the thin films of YBCO on $SrTiO_3$ substrates in the presence of a magnetic field with the expectation of finding any superconducting glass state behavior at low fields. We have observed no indication to such a glassy state and we, contrary to our expectation, have found a very small effect on the resistive transitions of samples. We think that it is a manifestation of an extreemly small correlation length of these new superconducting materials which makes them a completely new system to view.

Aknowledgements

The authors are thankful to Mr. G. Burri for his great help in microprobe analysis and to the Fonds National Suisse de la Recherche Scientifique for the financial support.

5. References

(1). J. G. Bednorz and K. A. Müller, Z. Phys. B 64, 189 (1986)

(2). K. A. Müller, M. Takashige and J. G. Bednorz, Phys. Rev. Lett. 58 , 1143 (1987)

(3) C. Ebner and A. Stroud, Phys. Rev. B 31 , 165 (1985)

Helvetica Physica Acta
Vol. 61 (1988)

0018-0238/88/060869-04$1.50+0.20/0

Spektroskopische Charakterisierung von Gleichgewichtsabweichungen in einem induktiv gekoppelten Plasma

S. Nowak und J.A.M. van der Mullen*

Technische Universität Eindhoven, Fakultät Physik, NL-5600 MB Eindhoven
**Physikinstitut der Universität, Pérolles, CH - 1700 Freiburg*

Abstract: In einem induktiv gekoppelten Plasma wurden Elektronendichte und -temperatur bestimmt. Dazu wurden zwei unabhängige spektroskopische Verfahren benützt: Die Starkeffektverbreiterung der Hβ-Linie sowie die absolute Emission von hochangeregten Argonzuständen. Durch den Vergleich der mit diesen zwei Methoden erhaltenen Resultate konnten die Abweichungen vom lokalen thermischen Gleichgewicht charakterisiert werden.

1. Einleitung

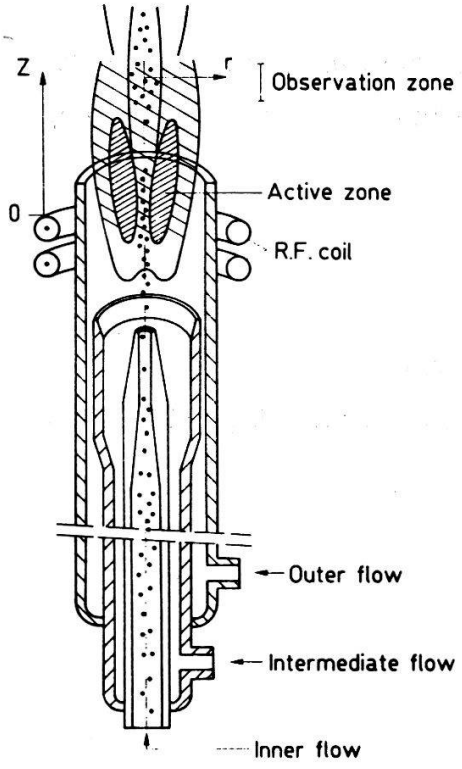

Fig. 1: Schema des ICP

Das induktiv gekoppelte Plasma oder ICP (Inductively Coupled Plasma) ist eine Anregungsquelle, welche für die spektrochemische Analyse von Spurenelementen zunehmend zum Einsatz gelangt. Das Plasma (Fig. 1) wird durch eine Hochfrequenzspule in einer atmosphärischen Argonströmung erzeugt. Die zu untersuchende Probe in Lösung wird als Nebel in das Plasma gesprüht.

Eine vieldiskutierte Frage ist, inwiefern sich das ICP als nahe beim lokalen thermischen Gleichgewicht oder LTE (Local Thermal Equilibrium) beschreiben lässt. In den 70er Jahren herrschte die allgemeine Ansicht, dass sich das ICP weit weg von LTE befinde. 1983 hingegen wurde von Raaijmakers et al. [1] vorgeschlagen, dass die Abweichungen von LTE in einem ICP sehr beschränkt sind.

Zur Ueberprüfung dieser Behauptung wurden die Elektronendichte n_e und die Elektronentemperatur T_e mit zwei unabhängigen spektroskopischen Methoden bestimmt. Die Elektronendichte wurde mit Hilfe der Starkeffektverbreiterung der Hβ-Linie bestimmt [2]. Absolutmessungen von hochangeregten Argon-Neutrallinien führen mit der Annahme, dass die Abweichungen von LTE beschränkt sind, zu einer Aussage über n_e und T_e. Dazu wird von den gemessenen Absolutintensitäten in einem Boltzmann-Plot nach einer fiktiven Besetzungsdichte $\eta_\infty = n_\infty/g_\infty$ bei der Ionisierungsenergie I_1 extrapoliert. Für diese Energie liefert die Saha-Gleichung unter Annahme von Quasineutralität:

$$\eta_\infty^s = \frac{n_e^2}{2g_+} \frac{h^3}{(2\ \pi\ m\ k\ T)^{3/2}} \qquad (1)$$

Da das ICP bei atmosphärischem Druck arbeitet, kann aufgrund des Grundgesetzes der kinetischen Gastheorie die Zustandsdichte n_1 bestimmt werden:

$$P = n_1\ k\ T_g = b_1\ n_1^s\ k\ T_g \qquad (2)$$

wobei T_g die Gastemperatur und $b_1 = n_1/n_1^s$ die Abweichung von der Saha-Besetzung n_1^s beschreibt. Durch Kombination von (1) und (2) sowie der Saha-Gleichung erhält man unter der Annahme $T_e = T_g$:

$$\frac{I_1}{k\ T_e} = \ln\left(\frac{P}{k\ T_e\ \eta_\infty^s}\right) - \ln\ b_1 \qquad (3)$$

Die Gleichungen (3) und (1) liefern für einen gemessenen Wert $\eta_\infty = \eta_\infty^s$ für verschiedene Werte von b1 die Parameter ne und Te.

Da die Starkeffektverbreiterung einen modellunabhängigen Wert der Elektronendichte liefert, können durch Vergleich der beiden Messmethoden die Abweichungen von LTE, ausgedrückt durch b_1, charakterisiert werden. Für $0.1 \leq b_1 \leq 10$ wird ein Plasma als nahe bei LTE definiert. Erste Resultate dieser Vergleichsmessungen [3] bestätigten die zuvor gemachte Annahme. Ausführliche Messungen für unterschiedliche Bedingungen [4] werden hier vorgestellt.

2. Experiment

Die Messungen wurden an einen ICP mit einer Arbeitsfrequenz von 100 MHz (Philips, Eindhoven) durchgeführt. Es wurden Gasflussraten von 12 l/min (aussen) und 0.6 l/min (Mitte) verwendet. Der zentrale Gasfluss wurde zwi-

schen 0.2 und 0.8 l/min variiert, die RF-Leistung betrug 0.8 und 1.5 kW. Die Messungen wurden zwischen 5 und 21 mm über der RF-Spule durchgeführt. Weitere Einzelheiten des experimentellen Aufbaus sind in [3] aufgeführt.

3. Resultate

Fig. 2 zeigt das radiale Profil der Elektronendichte bei z = 5 mm für unterschiedliche Werte der zentralen Gasflussrate ϕ_C. Dabei bedeuten die ausgezogenen Linien die Werte, welche mit den absoluten Ar-Intensitäten bestimmt wurden (für b_1 = 10 (oberste), 1, 0.1 (unterste)). Die aus der Hβ-Linie bestimmten Werte sind durch die unterbrochenen Linien bezeichnet. Wie dieser Figur zu entnehmen ist, kann das Plasma im Randgebiet ($|r| \cong 4$mm) als ionisierend ($b_1 \cong 10$) betrachtet werden. Im axialen Bereich ($r \cong \pm 0$mm) verändert sich das Plasma mit zunehmender Gasflussrate von ionisierend nach sehr dicht bei LTE ($b_1 \cong 1$).

Fig. 3 zeigt die entsprechenden Ergebnisse bei z = 15 mm. Bei niedriger zentraler Gasflussrate kann das Plasma als rekombinierend bezeichnet werden ($b_1 \cong 0.1$). Mit zunehmender Gasflussrate erscheinen die mit der Hβ-Methode bestimmten Werte in Randgebiet systematisch höher als jene mit der Ar-Methode. Dies würde zum Schluss führen, dass das Plasma in diesem Bereich mit zunehmender Gasflussrate wieder stark ionisierend wird. Physikalisch erscheint dies allerdings wenig plausibel, da es nicht ersichtlich ist, woher die für die zunehmende Ionisation notwendige Energie herkommen kann. Es stellt sich deshalb die Frage, ob die zur Benützung der Ar-Methode gemachten Annahmen noch erfüllt sind.

Die in Fig. 2 und 3 dargestellten Ergebnisse sind typisch für die weiteren gemessenen Bedingungen. Bei niedriger zentraler Gasflussrate kann das ICP als nahe bei LTE charakterisiert werden. Mit zunehmendem Gasfluss werden die Abweichungen von LTE ausgeprägter und die Bedingung $0.1 \leq b_1 \leq 10$ kann nicht mehr als erfüllt betrachtet werden. Bei höherer RF-Leistung kann man dieselbe Feststellung bei höherer Gasflussrate machen [4].

4. Schlussfolgerungen

Die zentrale Gasflussrate hat für das Anregungsgleichgewicht eines ICP's eine Schlüsselrolle. Bei niedrigen Werten dieser Variable kann das Plasma als nahe bei LTE bezeichnet werden. Mit zunehmendem Gasfluss müssen zur Erklärung der Ergebnisse grössere Abweichungen von LTE angenommen werden.

Diese Arbeit im Programm der Stiftung FOM (Utrecht) wurde durch die Niederländische Technologie Stiftung (STW) und den Schweiz. Nationalfonds unterstützt.

[1] I.J.M.M. Raaijmakers, P.W.J.M. Boumans, B. van der Sijde and D.C. Schram, Spectrochim. Acta 38B, 697 (1983)

[2] B.L. Caughlin and M.W. Blades, Spectrochim. Acta 39B, 1583 (1984)

[3] J.A.M. van der Mullen, S. Nowak, A.C.A.P. van Lammeren, D.C. Schram and B. van der Sijde, Spectrochim. Acta 42B (im Druck)

[4] S. Nowak, J.A.M. van der Mullen and D.C. Schram, zur Veröffentlichung angenommen in Spectrochim. Acta B

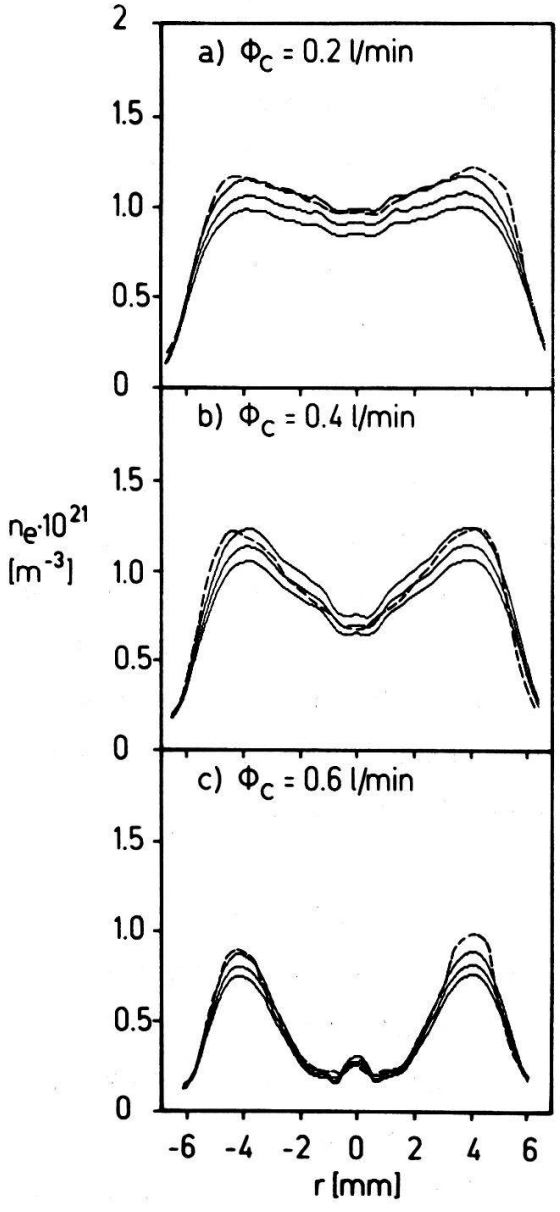

Fig. 2: n_e - Profil, z = 5 mm

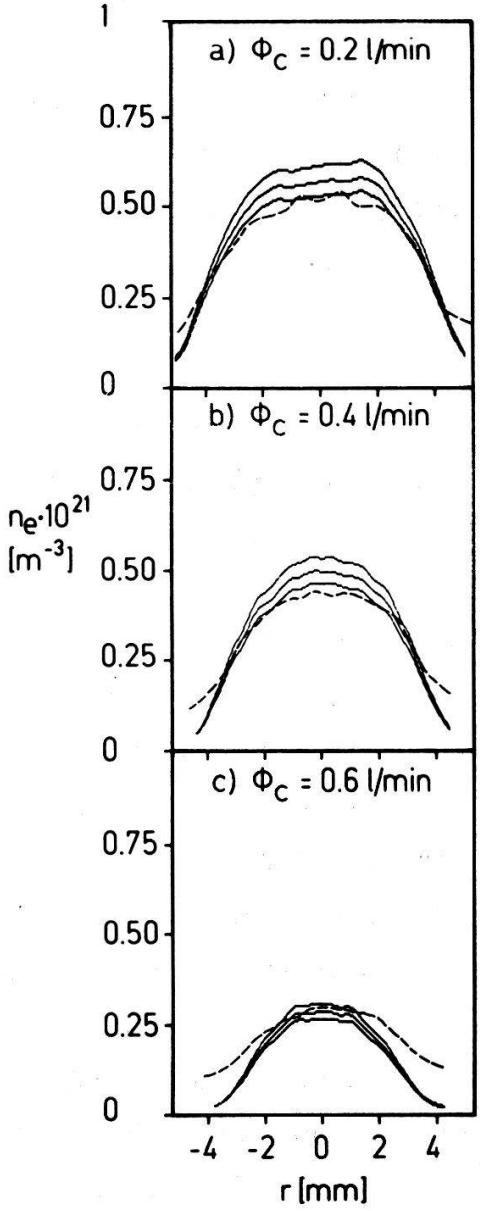

Fig. 3: n_e - Profil, z = 15 mm

Helvetica Physica Acta
Vol. 61 (1988)
0018-0238/88/060873-04$1.50+0.20/0

Epitaktische BaF_2-SrF_2-CaF_2 Stapel auf Si(111) und Si(100)

S. Blunier, H. Zogg, H. Weibel, AFIF, ETH Hönggerberg, CH-8093 Zürich

Stapel aus epitaktischem CaF_2, SrF_2 und BaF_2 wurden mittels Molekularstrahlepitaxie (MBE) auf Si(111) und, zum ersten Mal, auf Si(100) gewachsen. Durch schnelle Ausheizzyklen (RTA, rapid thermal anneal) während des Wachstums wird ihre Qualität erheblich verbessert.

Auf Si(111) wachsen die Fluoride trotz total 14% Gitterfehlpassung zweidimensional. Die RHEED-Bilder zeigen zudem scharfe Streaks und ausgeprägte Kikuchy-Bänder.

Auf Si(100) wachsen die Schichten ohne RTA dreidimensional mit (100) Orientierung. Mit geeigneten RTA-Zyklen kann man zudem erreichen, dass die Orientierung nach (111) wechselt.

Diese Schichtstapel werden als Puffer für das epitaktische Wachstum von II-VI und IV-VI Verbindungshalbleitern verwendet.

Können Verbindungshalbleiter epitaktisch auf Si aufgebracht werden, eröffnen sich neue Möglichkeiten für vollständig monolithische elektronische Bauteile. Diese können die unterschiedlichen elektronischen Eigenschaften der verschiedenen Halbleiter kombinieren. Die meisten Verbindungshalbleiter können jedoch wegen zu grosser Unterschiede in den Gitterkonstanten (z.B. 19% für CdTe auf Si) nicht direkt als epitaktische Schicht auf Si abgeschieden werden. Mit Gruppe II-a Fluorid Zwischenschichten kann das Gitter von Si (a=0.543nm) über CaF_2 (a=0.546nm), SrF_2 (a=0.579nm) bis zu BaF_2 (a=0.620nm) um 14,2% aufgeweitet werden

Die Fluoride wurden mittels MBE auf Si-Wafer aufgewachsen. Die nach der Methode von Shiraki (1) gereinigten Wafer sind nach dem Reinigungsprozess mit einer dünnen Oxydschicht bedeckt. Durch kurzes Aufheizen (ca. 3 Min. bei 900°C) im Ultrahochvakuum (UHV) wird das Oxyd entfernt. Das Auger-Spektrum zeigt eine bis auf minime Mengen Kohlenstoff (<0.01 Monolagen) saubere Oberfläche. Bei Si(111) Wafern sieht man im RHEED-Bild die 7x7 Oberflächenrekonstruktion und bei Si(100) die 2x1 Rekonstruktion.

Wachstum auf Si(111)

Bei Probentemperaturen um 750°C werden ca. 2nm CaF_2 mit einer Rate von 0,01nm/sec aufgedampft. Das RHEED-Bild besteht bei zweidimensionalem Wachstum aus Strichen (Streaks), bei dreidimensionalem Wachstum aus Punkten und bei polykristallinem Wachstum aus Ringen. Durch kurzes Aufheizen des Wafers auf ca. 1000°C (RTA) kann erreicht werden, dass die Oberfläche einkristallin wird und das CaF_2 zweidimensional weiterwächst.

Nachdem die CaF_2-Schicht die gewünschte Dicke von ca. 10nm erreicht hat, kann durch einen weiteren RTA-Schritt das RHEED-Bild verbessert werden. Die Streaks werden schmaler und die Kikuchy-Bänder deutlicher erkennbar. Die Streaks werden von an der Oberfläche (zweidimensionales Gitter) elastisch gestreuten Elektronen erzeugt. Werden sie intensiver und schmaler, so heisst das, dass die Kristallstruktur der Oberfläche besser wird. Da die Kikuchy-Bänder von inelastischer Streuung der Elektronen am dreidimensionalen Gitter hervorgerufen werden, bedeutet ihre Verbesserung im RHEED-Bild, dass die Schicht in den obersten Atomlagen (bis zur Eindringtiefe der Elektronen) in ihrer Atomstruktur verbessert wird. Wir fanden, dass geeignete RTA-Zyklen das RHEED-Bild bei allen Fluoriden verbessern.

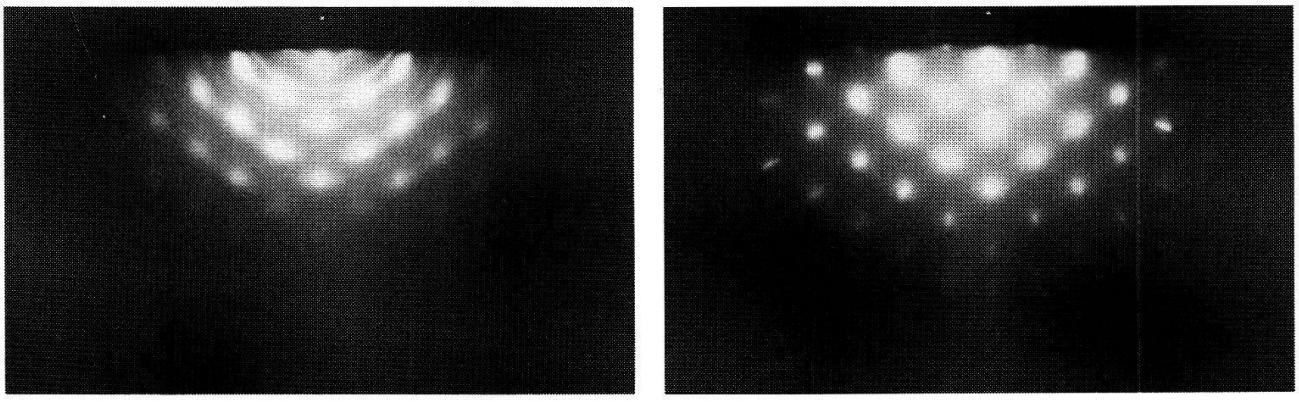

a) b)

Figur 1: RHEED-Bild einer 10nm dicken CaF_2-Schicht auf Si(100), a) vor RTA b) nach RTA (ca. 5sec/1000°C)

Die BaF_2-Schichten wurden bei Substrattemperaturen zwischen 420°C und 850°C mit Wachstumsraten von 0,08nm/sec bis 0,45nm/sec auf die mit CaF_2 beschichteten Si-Wafer aufgedampft. Mit einem Röntgendiffraktometer wurden die Gitterkonstanten der BaF_2 Schichten bestimmt. Daraus lassen sich die mechanischen Spannungen ermitteln. Bei den Systemen Si(111)-CaF_2(111)-BaF_2(111)

wurde schon früher (2) festgestellt, dass die Spannungen in den BaF_2-Schichten bei Raumtemperatur fast vollständig relaxiert sind. Dies gilt auch für BaF_2-Schichten, welche mittels einer CaF_2-SrF_2 Zwischenschicht auf das Si-Substrat aufgedampft wurden. Die RTA-Zyklen haben auf diese Spannungsrelaxation keinen Einfluss.

Die Oberflächen der BaF_2-Schichten, welche ohne RTA hergestellt wurden, zeigen im Rasterelektronenmikroskop (REM) keinerlei Struktur. Bei Schichten, welche RTA-Zyklen in späteren Wachstumsstadien unterworfen waren, zeigt sich im REM eine leichte Aufrauhung der Oberfläche.

Die BaF_2-Schichten wurden mit Rutherford Backscattering Spektroskopie (RBS) untersucht. Dabei wurden 2 MeV He-Ionen parallel zur [111] -Achse und ausserhalb einer ausgezeichneten Kristallachse auf die Schicht geschossen. Werden die He-Ionen parallel zur [111] -Richtung eingeschossen, so wird die Ausbeute der rückgestgestreuten Ionen durch den Channeling-Effekt kleiner gegenüber beliebiger Einschussrichtung. Diese minimale Ausbeute (χ_{min}) beträgt in unseren Proben 4%. Sie ist nahezu so tief wie bei (111)-Channeling von massiven Einkristallen.

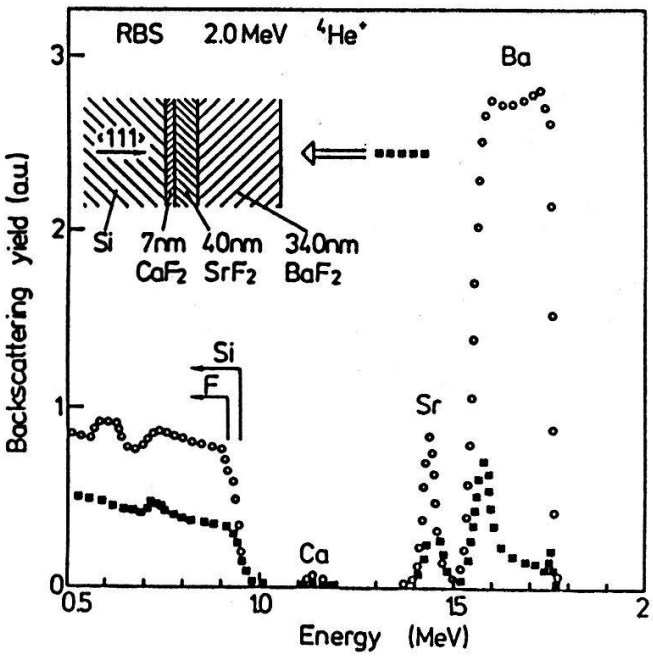

Fig 2: RBS-Spektrum einer Si(111)-CaF_2-SrF_2-BaF_2-Probe

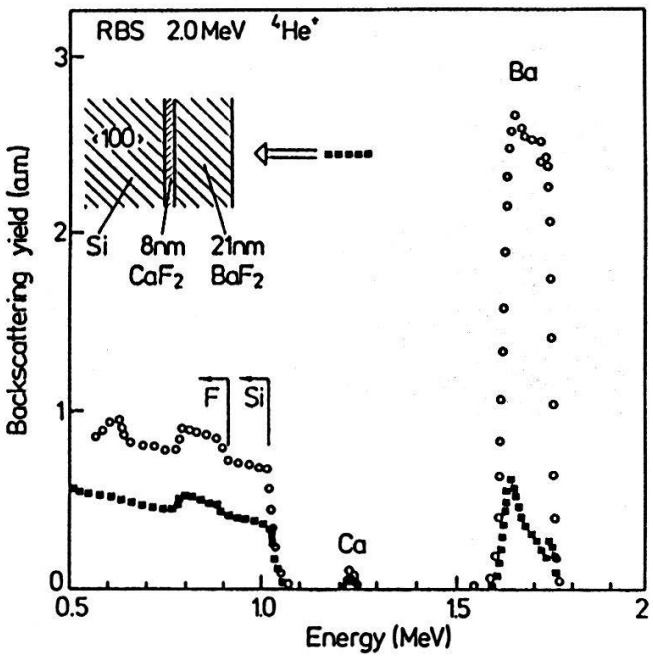

Fig 3: RBS-Spektrum einer Si(100)-CaF_2-BaF_2 Probe

Wachstum auf Si(100)

Bei einer Substrattemperatur von ca. 600°C wächst CaF_2 dreidimensional auf die Si(100) Fläche auf. Die Wachstumskeime bilden dabei dreieckige Pyramiden, deren Flächen (111)-Ebenen sind. Dies wird dadurch erklärt, dass die Oberflächenenergie der (111)-Ebenen (500erg/cm^2) kleiner ist als diejenige der (100)-Ebenen (530erg/cm^2) (3,4,5). Das dreidimensionale Wachstum führt zu Punkten im RHEED-Bild (Vergleiche Fig. 1a).

Nach dem Wachstum von ca. 10nm CaF_2 wird bei gleicher Substrattemperatur BaF_2 aufgewachsen. Nach wenigen Atomlagen führt dann ein RTA dazu, dass ausser den Punkten im RHEED-Bild Streaks sichtbar werden. Diese verschwinden aber bei zunehmender Schichtdicke wieder. Alle (100)-Schichten zeigen schon im Lichtmikroskop Strukturen und ihr χ_{min} liegt bei 10%. Interessant ist die Tatsache, dass auch hier die thermischen Spannungen bei Raumtemperatur in den BaF_2-Schichten relaxiert sind.

Wird bei einer CaF_2-Schichtdicke von wenigen Atomlagen (ca. 3nm) ein RTA durchgeführt, so zeigen sich im RHEED-Bild zusätzliche Punkte. Diese bleiben auch beim Weiterwachsen sichtbar und können noch nicht sicher interpretiert werden. Das darauffolgende Wachstum der BaF_2-Schicht kann durch geeignete RTA-Zyklen so gesteuert werden, dass eine homogene Schicht mit (111) Orientierung aufwächst. Diese BaF_2-Schicht zeigt im Elektronenchanneling mit dem REM eine 12-fache Symmetrie. Die BaF_2-Schicht besteht aus Domänen, die jeweils um 30 Grad senkrecht zur (111)-Oberfläche gegeneinander verdreht sind. Die Qualität dieser Schichten ist nicht besonders gut. Ihre Oberfläche ist rauh und ihr χ_{min} beträgt 30%.

Die Arbeit wurde vom schweizerischen Nationalfonds und von der Gruppe für Rüstungsdienste finanziell unterstützt.

Referenzen:

[1] A. Ishizaka and Y. Shiraki, J. Electrochem. Soc., 133, 666, (1986)
[2] H. Zogg, Appl. Phys. Lett. 49, 933, (1986)
[3] J.J. Gilman, J. Appl. Phys. 31, 2208, (1960)
[4] P.F. Becher and S.W. Freimann, J. Appl. Phys. 49, 3779, (1981)
[5] L.J. Schowalter et all., J. Appl. Phys. 58, 302, (1985)

Helvetica Physica Acta
Vol. 61 (1988)
0018-0238/88/060877-04$1.50+0.20/0

OPERATING PRINCIPLES OF MAGNETOTRANSISTORS

A. Nathan*, K. Maenaka**, W. Allegretto*, H.P. Baltes*, and T. Nakamura**
*University of Alberta, Edmonton, Alberta, Canada, T6G 2G7
**Toyohashi University of Technology, Tempaku-cho, Toyohashi, 440 Japan

Abstract: Numerical modeling and Hall-probe measurements in integrated magnetotransistor (MT) structures show that the Hall field along the base-emitter junction is too small to produce appreciable emitter injection modulation. Carrier deflection seems to be the preferable operating principle for linear MT.

1. Introduction

The well-known models of Hall voltage (electric potential gradient) and Lorentz deflection (current line or carrier deflection) describe the carrier transport patterns in very long and very short extrinsic semiconductor slab geometries, respectively. Both models serve as valuable heuristic tools in the design of integrated MT [1]. But in view of the complexity of bipolar action under magnetic field, the application of any such simple, intuitive model to MT operation can only be hypothetical and has to be checked by solving the carrier transport equations with adequate material (processing) parameters and boundary and operating conditions. In favourable cases the resulting carrier transport patterns may resemble those of the one or the other simple model, whose validity would then be verified.

In this contribution we summarize results of numerical modeling and experiments designed to provide information on a possible Hall voltage in the base region in the dual-collector MT structure shown in Fig. 1 (top). A Hall voltage along the emitter-base junction is believed [1] to cause a spatial modulation or asymmetry of the emitter injection,

which would explain the observed current imbalance in dual collector MT exposed to a magnetic field. We find that the Hall field in question is too small to substantiate the validity of the asymmetric injection model. This result as well as our previous findings [2-5] lead us to rule out emitter injection modulation as an operating principle of linear MT in favour of carrier deflection.

2. Numerical Modeling

We model the carrier transport in the base region of the MT as shown in Fig 1. (bottom). The silicon dioxide layer on the device surface is consistent with fabrication technology, while the "artificial" oxide at the device side and bottom walls is meant to replace the base-collector p-n junction. Poisson's equation and the continuity equations are as usual, while the current density **J** in the current transport equations is augmented by the term μ * **J** x **B** with μ* denoting the Hall mobility and **B** the magnetic induction. The system of partial differential equations is solved with realistic physical parameter models and subject to the appropriate Dirichlet and Neumann boundary conditions. The presence of the magnetic field, however, could lead to a significant Hall field at the device's insulating boundaries. Thus the standard boundary condition of zero normal component of the electric potential gradient may be invalid. The introduction of the oxide layer allows to avoid imposing this standard condition at the silicon/oxide interface, where the actual boundary condition on the electric potential is treated an an unknown instead. The normal component of the electric potential gradient is assumed to vanish only at the oxide's (remote) outer edge.

Figure 2 shows the resulting equipotential lines (top) and minority carrier (electron) density flow lines (bottom) in the vicinity of the emitter for B = 2 tesla and realistic operating conditions. The equipotential lines appear to be

symmetric around the emitter base junction indicating that there is no significant Hall potential gradient. Indeed, high resolution computation (±0.5 μV stopping criterion) was needed in order to find the minute Hall voltage at all. There is also no asymmetry in the injected emitter current at the metallurgical emitter base junction. But the magnetic field does affect the distribution of the current density in a way reminiscent of carrier deflection.

3. Hall probe measurement

The MT sample shown in Fig. 1 includes two Hall probes of minimal size placed close to the emitter-base junction. These probes allow to pick up the Hall voltage that supposedly builds up along the junction. The Hall voltage thus observed turned out to be ten times smaller than the value predicted for the emitter efficiency modulation model, in confirmation of the numerical modeling results and previous measurements [4,5].

4. References

[1] H.P. Baltes and R. Popovic, Proc. IEEE 74, 1107 (1986).

[2] A. Nathan, W. Allegretto, W.B. Joerg, and H.P. Baltes, Transducers '87, IEE Japan, Tokyo, 519 (1987).

[3] W. Allegretto, A. Nathan, and H.P. Baltes, Proc. NASECODE V, Boole Press, Dublin, 87 (1987).

[4] K. Maenaka, T. Ohsakama, M. Ishida, and T. Nakamura, Sensors and Actuators 13 (1988) in press.

[5] A. Nathan, W. Allegretto, and H.P. Baltes, Sensors and Materials 1 (1988) in press.

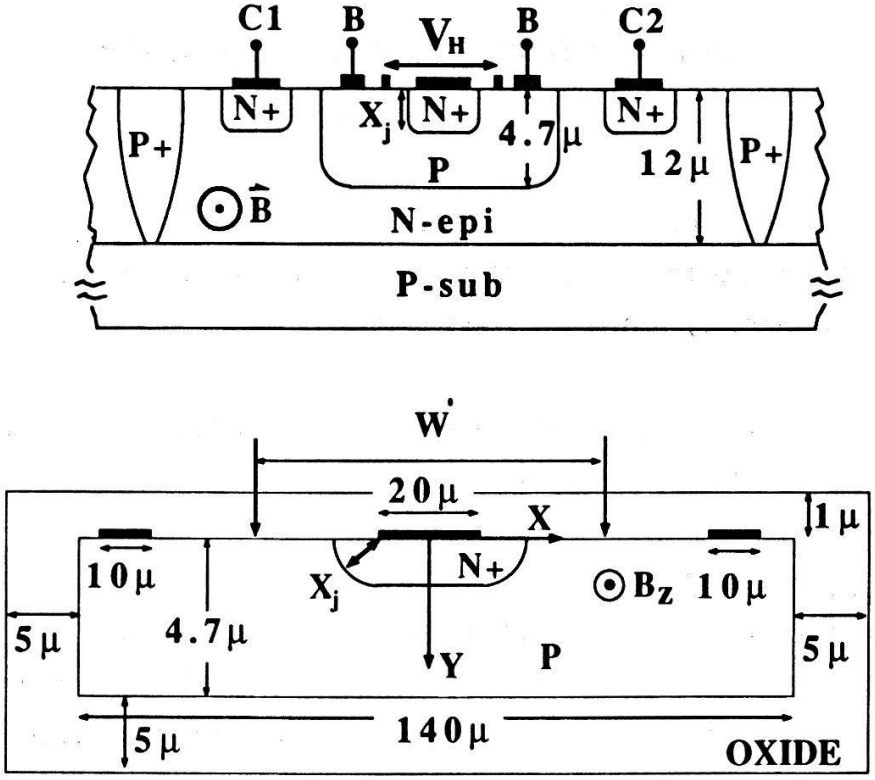

Fig. 1: MT cross section (top). Modeling geometry (bottom)

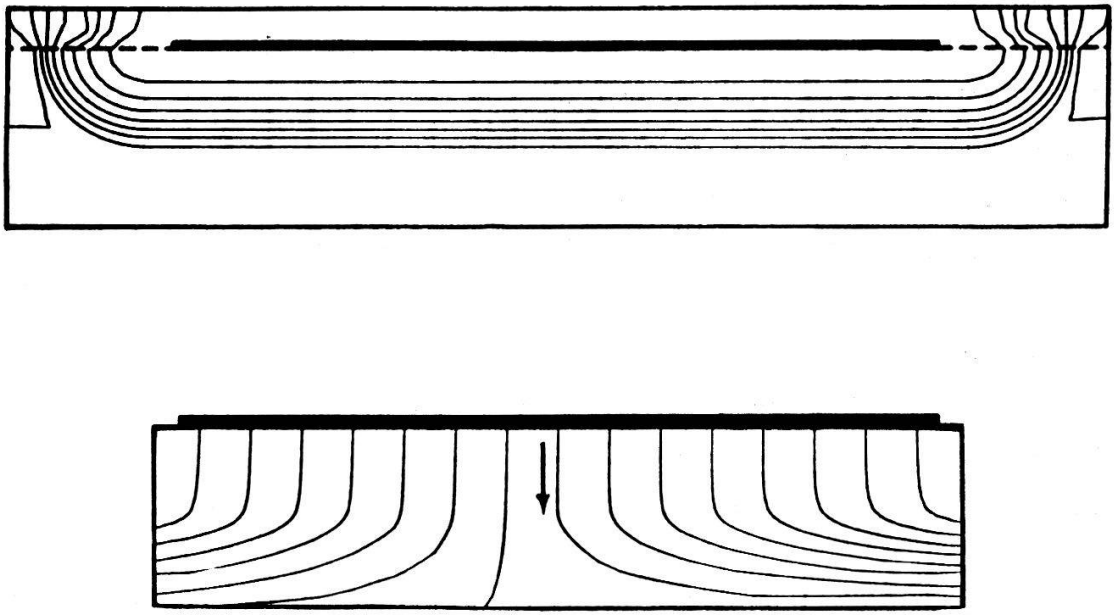

Fig. 2: Equipotential lines (top). Electron flow lines (bottom)

Helvetica Physica Acta
Vol. 61 (1988)
0018-0238/88/060881-04$1.50+0.20/0

USE OF STANDARD CMOS POLYSILICON FOR MICROSENSORS

M. Parameswaran and H.P. Baltes
Alberta Microelectronic Centre, University of Alberta, Edmonton, Alberta, Canada, T6G 2C2

Abstract: Two applications of polysilicon in micro-transducer design are presented.

1. Humidity sensor

We designed and fabricated a humidity-controlled multivibrator in 5 micron double-poly CMOS technology. A sensitivity of 25 Hz/%RH is obtained without using any water absorbing layer. The timing capacitor of the multivibrator is a pair of interdigitated polysilicon electrodes forming a lateral capacitance structure (Fig. 1). Compatibility of the sensor structure with CMOS process technology [1] is achieved by modification of the standard layout methods. A set of contact cuts and pad openings are used to expose the region between the electrodes to ambient air (Fig. 1). Impedance measurements between 10 and 500 kHz show that the sensor element is capacitive. Its capacitance is a function of the relative humidity of the ambient air.

2. Microbridge

Polysilicon-based micromechanical structures are currently fabricated using phosphosilicate glass (PSG) as a sacrificial layer and buffered oxide etch (BOE) as etching solution. We made microbridge structures by using a standard CMOS process [1] with minimal postprocessing (field oxide etch) by intentional design rule violations. A large contact cut and a pad opening are placed above the poly

layer where the bridge is required. Photoresist is applied and an opening is made over the pad-opening area. The resulting structure and the subsequent field oxide etching steps are shown in Fig. 2. BOE undercuts the polysilicon by removing the field oxide below it. Thus the bridge structure shown in Fig. 2 is formed. The bridge is relieved of stress thanks to a high-temperature annealing step innate in the process. Sensor applications of the microbridge are in progress.

[1] CMOS technology is offered to Canadian Universities by Northern Telecom Canada Inc., Ottawa, through the Canadian Microelectronic Corporation, Kingston, Ontario.

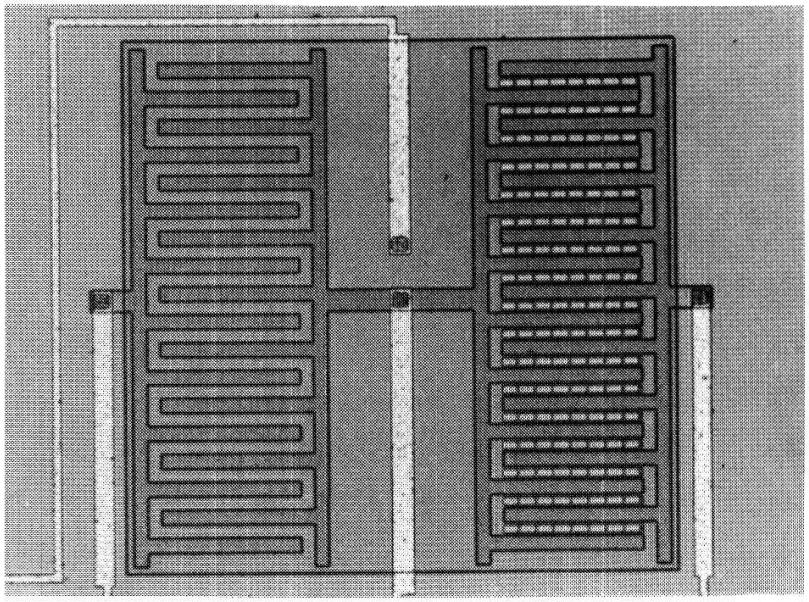

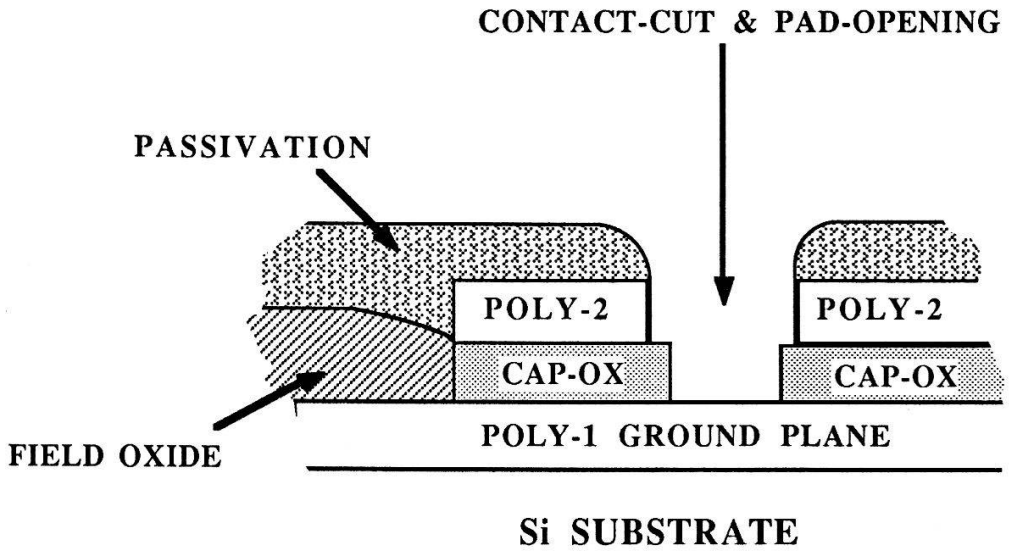

FIGURE 1: Humidity sensor. Top: micrograph of lateral reference and sensor capacitors. Bottom: cross section of sensor capacitor.

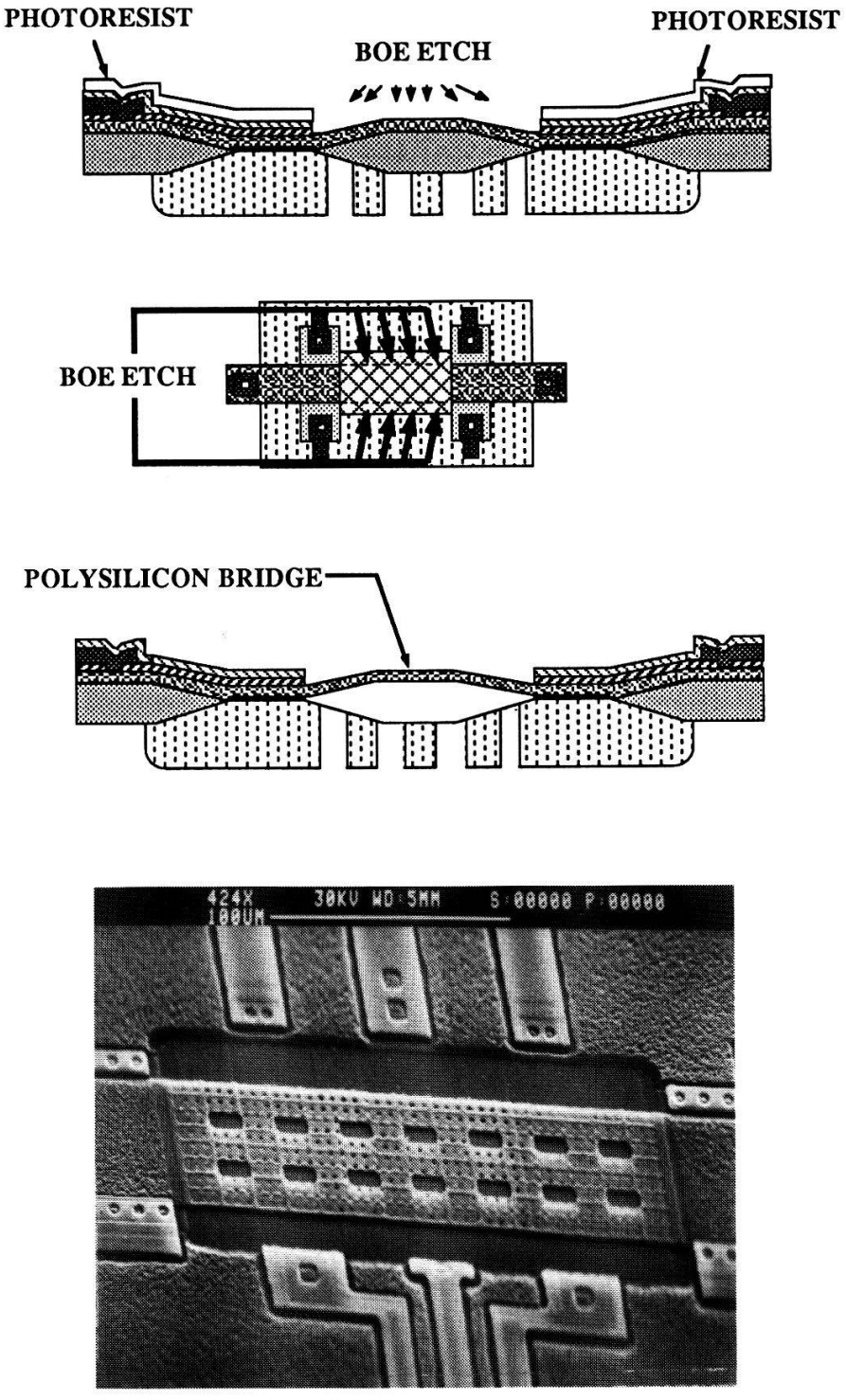

FIGURE 2: Polysilicon microbridge. Top: postprocessing step. Bottom: micrograph of 47 by 180 micron bridge structure.

Helvetica Physica Acta
Vol. 61 (1988)

0018-0238/88/060885-04$1.50+0.20/0

MEASUREMENT OF SMALL TEMPERATURE VARIATIONS IN GAS BY ULTRASONICS.

O.Oehler, J.Wieland and S.Friedrich, Institute for Quantum Electronics, ETH Hönggerberg, CH-8093 Zürich, Switzerland

Abstract: A device is presented which allows the measurement of small temperature variations in a gas. The measurement is based on the temperature dependence of the tuning of an ultrasonic resonator.

1. Introduction

The measurement of gas temperatures usually is achieved by solid state thermosensors, like thermocouples, semiconducting sensors or thermoresistive elements. The use of such devices suffers from the bad thermal conductivity of gases. This results in a long time constant. Direct methods for measuring gas temperatures use temperature-dependent properties of gases like the thermal expansion (gas thermometer). The thermosensor described here is based on the temperature dependence of the velocity of sound. From its considerably large temperature coefficient (dv/dT = 0.59 m/s K in air at 300 K) a high sensitivity of the temperature measurement was expected. Temperature-induced variations of the velocity of sound can be determined accurately by measuring the change in tuning of an acoustical resonator.

2. Experiment

Two identical ultrasonic transducers (1) were arranged oppositely as given in Fig. 1. One of these transducers was excited by a voltage controlled oscillator at a frequency of 220 kHz and a typical peak-to-peak voltage of 18 V, the other one was operated as a receiver. The transducers were positioned in a sealed metal tube at an adjustable distance of 1 cm. The medium in this cell was exchangeable through gas inlets. The signal from the receiver was processed by an amplitude demodulator - a diode rectifier or a lock-in amplifier (2). Its low frequency output either was fed to a second lock-in amplifier, its reference being taken from the light source modulator, or a digital storage oscilloscope was used together with an addi-

tional preamplifier allowing large-range offset adjustment. In the first case accurate rms-values of the temperature effect were measured, and in the latter case the time evolution of the gas temperature was obtained.

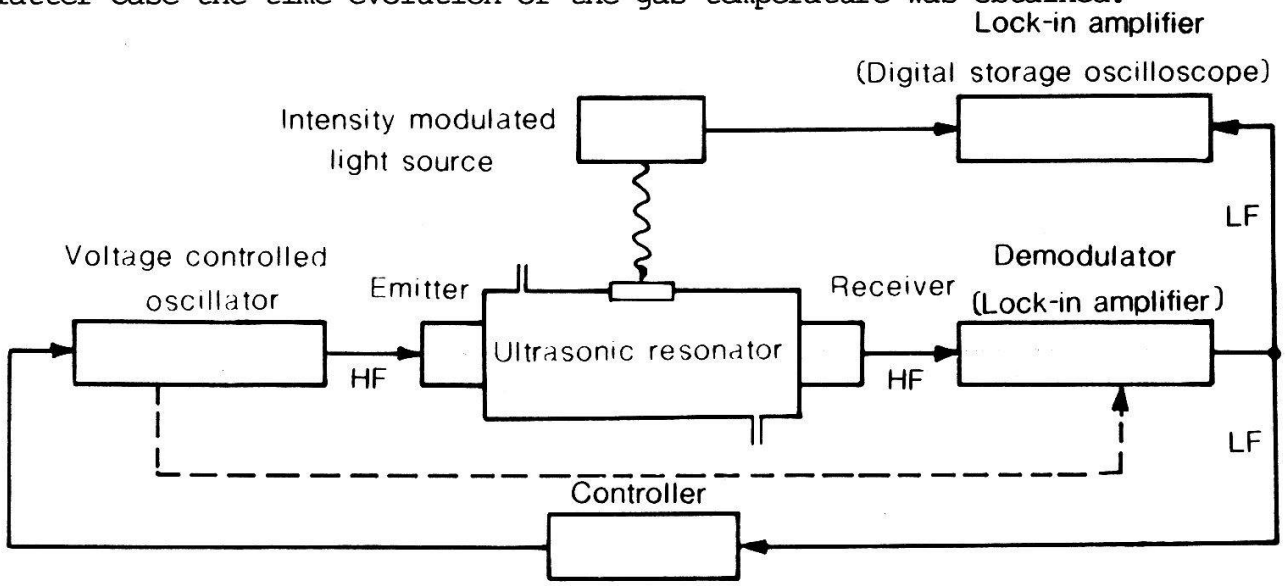

Fig 1 Layout of the thermosensor

Small temperature variations of the gas enclosed in the ultrasonic resonator were produced by absorption of infrared light. The radiation from an intensity-modulated source entered the resonator cavity through a sapphire window. This light source was composed of a tungsten filament enclosed in a glass bulb with an attached sapphire window (3). It was operated at a typical power of 7.8 W and was modulated by a mechanical chopper. Its switching signal was used as a reference for controlling the second lock-in amplifier.

On varying the distance between the two ultrasonic transducers, resonances as given in Fig 2 were observed at the receiver.

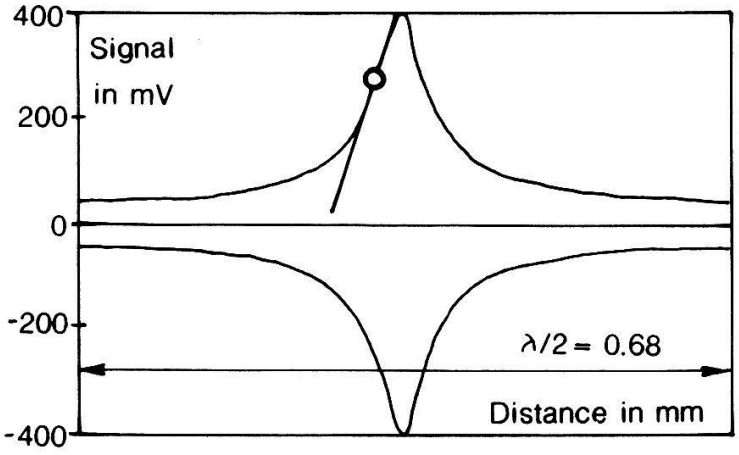

Fig 2 Ultrasonic 12th harmonic, operating point and derivative dU/dl

It was noted that the magnitude and the shape of these resonances depend strongly on the parallelism of the surfaces of the transducers. Even a tilt angle between the transducer surfaces of 1 degree produced a signal attenuation on resonance of the order of 30 %.

The derivative dU/dl is nearly constant over a considerable range of the resonance curve. The resonator was operated in this linear range as shown in Fig 2. Corresponding curves for lower harmonics show larger derivatives. Therefore an operation of the resonator at low harmonics would be advisable at first sight. But since the shift $\Delta l = (dv/dt)\cdot\Delta t$ is proportional to the length l_o of the resonator, the sensitivity of the velocity of sound to temperature dv/dT is nearly independent of the length l_o of the resonator (Fig 3)

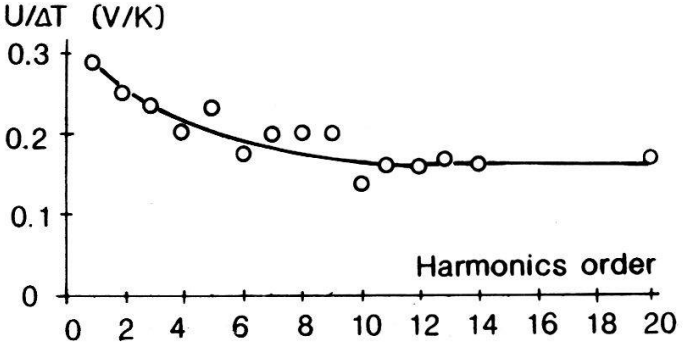

Fig 3 Dependence of the sensitivity dv/dT on the lenght l_o of the resonator.

3. Results

The described measurement allows a nearly pressure independent determination of the temperature of a gas. This so-called photothermic experiment is complementary to photoacoustics where the pressure signal related to the light absorption is measured. This follows from the formula describing the velocity of sound c: (4)

$$c = \sqrt{\varkappa \cdot p/\varrho}\,, \qquad \text{where } \varkappa = c_p/c_v \text{ (in air } \varkappa = 1.4).$$

For an ideal gas the density ϱ is proportional to the pressure p; therefore c becomes independent of the pressure:

$$c = \sqrt{\varkappa \cdot (p_o/\varrho_o)\cdot(1 + \gamma \cdot T)}\,, \quad \gamma = 1/273.15\ K^{-1} \text{ in air}$$

In Fig. 4 the results for a periodic optical excitation of air in the ultrasonic resonator is given. The temperature calibration was obtained from the measured voltage ΔU, the derivative dU/dl from Fig 2 and from literature values of the temperature dependence of the velocity of sound (dv/dT).
According to

$$\Delta T = \{v_o/(l_o \cdot (dU/dl) \cdot (dv/dT))\} \cdot \Delta U$$

the temperature calibration, as given in Fig 4, was determined.
For checking the calibration ΔT was calculated according to:

$$\Delta T = P \cdot \Delta t/(c_v \cdot \varrho \cdot V),$$

where Δt : illumination period,
c_v: specific heat of the gas
V : volume of the illuminated gas

From the calculated light input of $P = 5\ 10^{-5}$ W a value of $\Delta T = 3.9$ mK was obtained. This result is in good agreement with the temperature scale given in Fig 4.

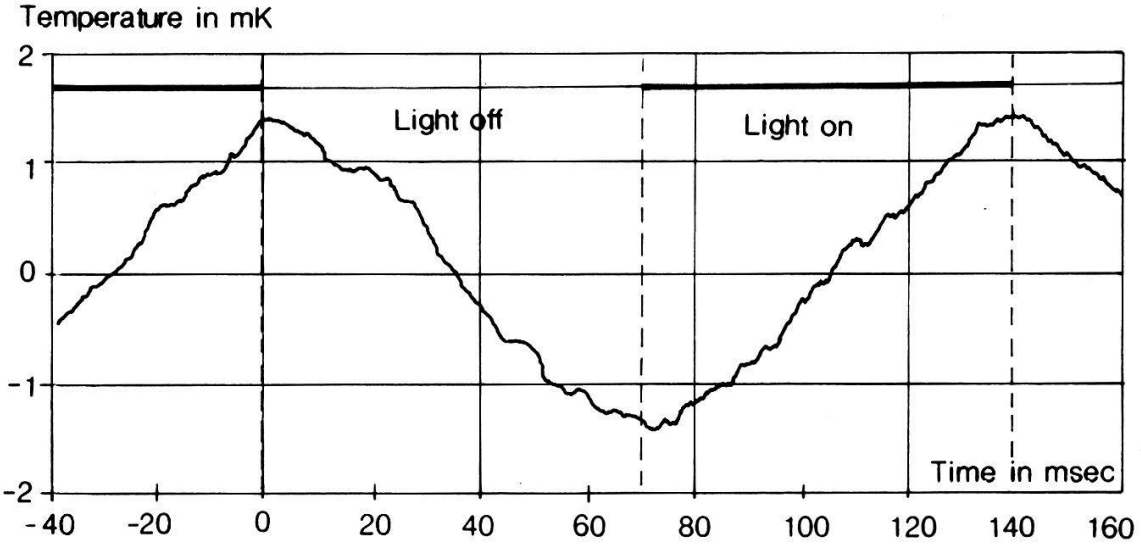

Fig 4 Time evolution of the gas temperature on periodic optical excitation.

From Fig 4 it follows that changes in the gas temperature of the order of mK can be determined easily. The shape of the given curve was obtained for 32 accumulations. This represents a time constant of 4.5 sec. From inspection of Fig 4 a peak-to-peak value of the noise of 0.15 mK can be estimated. At a signal accumulation time of 10 sec a signal/noise-ratio of 1 would occur at temperature variations of 0.1 mK.

4. Literature.

(1) Ultrasonic transducer model E-188/220, Massa Products Corp., Hingham, Mass 02043, USA.

(2) Lock-in analyzer, Princeton Applied Research, model 5204. This instrument is specified for a maximum frequency of 100 kHz. Nevertheless it was operated at the required frequency of 220 kHz after appropriate calibration.

(3) Aritron Instrumente AG, CH 8123 Ebmatingen, Switzerland.

(4) E.Grimsehl, Lehrbuch der Physik, Bd. 1, Teubner, 1977.

Helvetica Physica Acta
Vol. 61 (1988)

0018-0238/88/060889-04$1.50+0.20/0

MITTLERES MENSCH-MAXIMALALTER t_{max}=103.2J, UND TOD IN PHYSIKALISCHER SICHT

M. Kredl(*) und J.T. Muheim, Univ.(*) und ETHZ, Hönggerberg, 8093 Zürich

Auszug: Es ist nicht erlaubt, vom Individualmaximalalter (115J?) auf die ganze Menschheit zu schliessen. t_{max} lässt sich mehrfach quantenphysikalisch exakt ableiten. Am anschaulichsten erfolgt dies aus der Struktur des H-Atoms. Tod tritt dann ein, wenn der zeitlich bedingte Durchlauf des Lyman-Hauptserien-Lebensdauerkontinuums (r-Zweig der s-r-QS!) an der Seriengrenze auf die 1. infinitesimale Zeitlücke (="verbotene Zone") stösst. Das minimale Zeitelement von $\{t\}$ entspricht der molekularen Elementarzeit $t_{min}=\tau_2$ in der Zygotbildung bzw. Nabelschnurdurchtrennung bei der Geburt. In 4. Rezessionsordnung erscheint das Heim-Aeon vom Radius Λ^* als Bild des H-Atoms. Chakras sind Quantenstrukturen der 1. Stufe, und entsprechen den Elektronenschalen bzw. Perioden des PS der O. Stufe. Für die Anteile der typischen Alterskrankheiten -Alterskrebs, Alzheimer etc. - ist für t_{max} ca. 100% Häufigkeit zu erwarten.

1. Verschiedene Methoden der Altersbestimmung

a) H-Lebensdauerkontinuum (Fig.1 und 2). Der Zusammenhang zwischen der Lebensdauer τ des H-Atom-Zustands und dem Lebenszeitelement t der Lebenszeitmenge $\{t\}$ ist extrem einfach, da die zur einzelnen t-Rezession gehörende Rahmen-WW $\alpha_t(\tau)$ in einfacher Weise mit dem Radius der jeweiligen Fleckatomzelle A (A im F-Bereich der 1. Stufe, Fig.2) verknüpft ist. Dieser Radius $\lambda\!\!\!^{-}_C=ct$ widerspiegelt einerseits die Eigenzeit τ, und ist anderseits ein "Persönlichkeitsradius", d.h. ein Comptonradius $\lambda\!\!\!^{-}_C=\hbar/m_\tau c$. Die Comptonmasse $m_\tau=\hbar/\tau c^2$ geht quadratisch in die Rahmen-WW $\alpha_t(\tau)=(m_\tau/m_o)^2$ ein. Hierbei ist $m_o=\zeta_f m_p=\sqrt{\pi}m_p\tilde{=}m_\Omega$ - die ladungsäquivalente Masse der Ur(O)- oder Einheits-WW, $\alpha_o=1$.
Der zur t-Rezession gehörende Bohrradius enthält nun seinerseits die Rahmen-WW und ist gleich dem quantisch abgeregten Hubble-Rand: $a_t(\tau)=\lambda\!\!\!^{-}_e/\alpha_t(\tau)=ct/e$. Die quantische Abregung bewirkt eine Verkürzung des "radialen" Hubble-Rands ct um die Eulerzahl e. Mit $\lambda\!\!\!^{-}_e=\hbar/m_e c$ folgt nach t aufgelöst:

$$t = \frac{e\lambda\!\!\!^{-}_e}{c\alpha_t(\tau)} = \frac{e}{c}\left(\frac{\hbar}{m_e c}\right)\left(\frac{m_o}{m_\tau}\right)^2 = \frac{e\, m_o^2 c^2}{m_e \hbar}\,\tau^2 = \text{const.}\,\tau^2,$$

wo mit e=2.7182, m_o=2.9809x10^{-27}kg, c=2.9979x10^{8}ms^{-1}, m_e=0.91095x10^{-30}kg, $\hbar$= 1.0545x10^{-34}Js für const.=2.259x10^{28} s^{-1} folgt.

Randwerte: (i) Das minimale Lebenszeitelement t_{min} wird bestimmt durch die kürzeste Lebensdauer τ_{min} des im Lyman-Kontinuum maximal angeregten Elektron-Proton-Zustands $E(\tau_{min})$. Diese ist aber gerade gleich der Eigen- oder Lokalisierbarkeitszeit des Elektrons: $\tau_{min}=\lambda\!\!\!^{-}_e/c$, wo $\lambda\!\!\!^{-}_e=\hbar/m_e c=3.8615x10^{-13}$m der Elektron-Compton- bzw. -Lokalisierbarkeitsradius ist. Grund: eine echte Elektron-Proton-Beziehung im Kontinuumszustand ist nur so lange gewährleistet, als beide Partner sich als Individuen erkennen. Wird durch eine zu grosse Anregung der Eigenbereich enger als der Ruhemassen-Comptonbereich, so verliert das Teilchen die Beziehungsfähigkeit. Bei τ_{min} ist dies für das Elektron der Fall. Es ist τ_{min} =1.288x10^{-21}s. Daraus folgt für $t_{min}=const.\tau_{min}^2$=3.749x10^{-14}s. t_{min} ist angenähert gleich der durch die Unschärferelation gegebenen Grenzzeit für Molekül(ionen)-Formation: τ_{opt}/ζ_f^{*6}=2.928x10^{-14}s [1]. Experimentell wurde τ_2=(3-3.5)x10^{-14}s gefunden. N.B.: τ_{min} in dieser Arbeit hat nicht die gleiche Bedeutung wie τ_{min} in [1]. $t_{min}=\tau_2$ entspricht formal erstens der Bildungszeit des ersten Zygotmoleküls von Samenzelle und Eizelle, und zweitens, unter komplexen Abbildungsverhältnissen, der Durchtrennzeit der letzten molekularen Bindung bei der Nabelschnurdurchtrennung.

(ii) Das maximale Lebenszeitelement t_{max} des in die universale Rezession eingebetteten Lebens ergibt sich aus dem Faktum, dass wegen des durch die t/t_{akt}-Synchronisation bedingten Durchlaufs der unwillkürlichen Kundalini-Perturbation durch dasτ-Spektrum nach der Zeit t_{max} die Lyman-Seriengrenze erreicht wird. Diese Grenze entspricht dem niedrigstangeregten Kontinuumszustand. τ ist hier maximal und gleichzeitig Kontinuumsgrenzwert, denn anschliessend folgt die erste infinitesimale Zeitlücke im diskreten Teil des r-Zweigs. Sie signalisiert ein physikalisches Verbot. Gleichzeitig ist diese Grenze identisch mit der Hauptfixstelle der s-r-Abbildung im Phasenraum, also Koinzidenzstelle für die Seriengrenzen von r- und s-Zweig der Lyman-Hauptserie. Im Hertz-Bohr-Bild ergibt sich für τ_{max}: $\tau_{max}=\tau_{w',ool}=(3\varepsilon_o c m_e/2\pi e_s^2)\lambda_{ool}^2$, wo nach dem Balmer-Gesetz $\lambda_{ool}^{-1}=R_y(1/1^2 - 1/oo^2) = Ry$ gilt, und die Rydbergkonstante $R_y=m_e\alpha_s^2 c/2h$=1.0967x10^{7}m^{-1} beträgt. Oder umgeformt folgt für die Grenzlebensdauer:

$\tau_{max}=3h/\pi\alpha_s^5 m_e c^2 = 3.735\times10^{-10}$s, worin $\alpha_s=e_s^2/2\varepsilon_o hc=7.297\times10^{-3}$ die Sommerfeld-Feinstrukturkonstante ist. In die t/τ-Relation eingesetzt, folgt dann:
$t_{max}=3.152\times10^{9}$s=99.90J ≅ 100J.

Ergebnis: Durch eine Art Autoradiesthesiephänomen setzt sich das Leben mit dem quasikontinuierlichen Zeitelement auf den universalen Zeitpfeil $t_{akt}=12.64\times10^{9}$J und schreitet mit ihm monoton fort. Diese Resonanz bewirkt eine rein zeitliche, universal-expansionsbedingte, dem Willen nicht unterworfene Kundalini-Perturbation. Sie läuft im diskreten Teil des H-Niveauschemas von unten nach oben, also von niedrigerer zu höherer Anregung. Nach der Zeit t_{max} wird das höchstangeregte Chakra - das Scheitelchakra $r_{7.Ch}$ - erreicht, was den Tod einleitet. Dieses höchste Chakra widerspiegelt dimensionsmässig die Seriengrenze, denn es gilt $r_{7.Ch}=c\tau_{w,rool}=c\tau_{w,sool}=r_{w,ool}=s_{w,ool}=0.112$lm. Der psychischen Reifezeit $t_r=t(\tau_{w,s2l})=10$J entspricht in g-Rezession 100Br.J=3.1×10^{14}J der Brahma-Lebenszeitenergiestruktur. Fig.2 zeigt in vereinfachter Darstellung die 5 Stufen (0.-4.) der Fleckatom(A in F)/Hubble-Rand-Schachtelung, in welcher sukzessive chemisches Atom (0.), Chakra-Atom (1.), Lebenszeit-Atom (2.), eschatologischer Fleck (3., nicht Fleckatom!) als Bildbereichsgrenzen des Heim-Aeons $\Lambda^*=1.345\times10^{110}$Lj auftreten. Λ^* selbst markiert eine Grenze zwischen einem Wachstums- und einem Stationär-Bereich.

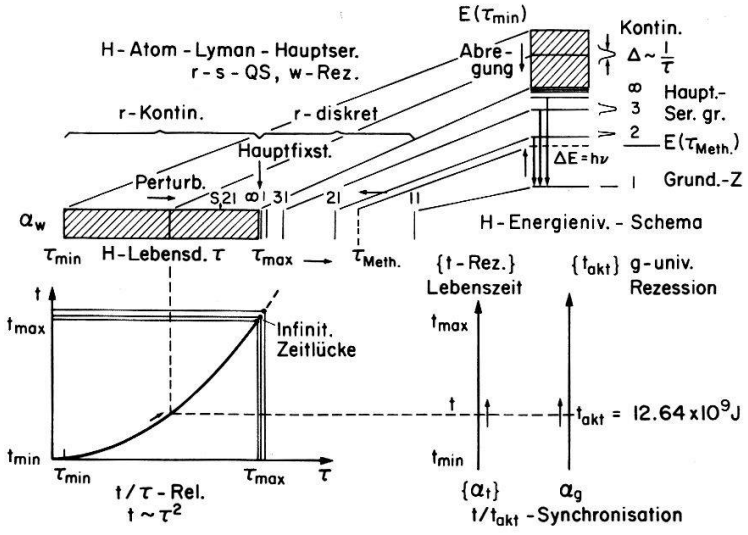

Fig.1 H-Lebensdauer (τ)-Lebenszeit (t)-Schema

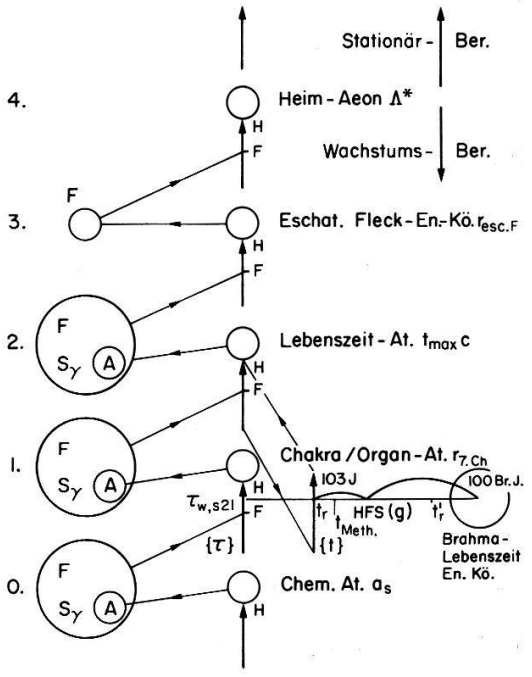

Fig. 2 Schema Fleckatom / Hubble-Rand-Schachtelung

b) Aura-Methode. Eine wesentlich anspruchsvollere Methode zur Bestimmung von t_{max} setzt die Kenntnis der universellen Aura-Quantenstruktur voraus, für die eine Art angeregter psychischer Urradius $L_{(-\infty),v\to c}=\pi r_{(-\infty),v\to c}$ existiert. Der angeregte physische Urradius beträgt $r_{Aura,SZ,v\to c}=eR_o$. t_{max} erscheint nun als ein Bild der Hubble-Zeit $t_{g,\underline{H},as}$ des gravitativen (asymmetrischen) Einzeluniversums (=Teil eines Paars UU), wobei die g-Hubble-Zeit im Verhältnis von psychischem zu physischem Urradius verkürzt wird. $t_{max}=t_{g,H,as}(L_{(-\infty)v\to c}/r_{Aura,SZ,v\to c})=t_{g,H,as}(\pi r_{(-\infty),v\to c}/eR_o)$. Mit $t_{g,H,as}=H_g^{-1}=5.884\times10^{17}$s, $r_{(-\infty),v\to c}=1.304\times10^{-14}$m, $R_o=2.746\times10^{-6}$m, folgt für $t_{max}=3.229\times10^{9}$s=102.3J. Optische Kommunikation hört am radialen Hubble-Rand auf, da hier die Rotverschiebung $z\to\infty$ geht. Die Lebenszeitsphäre vom maximalen Zeitradius t_{max} erscheint so als das psychische Bild zur physischen, g-universalen Lichtwelt, deren Zeitradius gleich der radialen Hubble-Zeit ist.

c) Lebensalteratom. t_{max} ist auch angenähert gleich der 6-fachen Lichtlaufzeit durch das superschwache Bohratom vom Radius $a_b=ct=\lambda\!\!\!^{-}_e/\alpha_b=17.2Lj: t_{max}=6a_b/c$. Der Grund dafür ist der, dass $6a_b$ bis auf den Faktor π/e gleich ist dem Fleckradius jener Rezession (F=o), für welche der intrinsische Fleck vom Radius $r_{F=o,F}$ mit dem abbildungsmässigen Urradius $R_{F=o,o}$ koinzidiert. Die Abbildung auf das Innere der nichtsingulären Ursphäre in i-Rezession, $R_{i,o}=(\alpha_g/\alpha_i)xR_o$ führt zu einem physikalischen Verbot. Dies wirkt sich auch auf die Lebensdauer begrenzend aus. Es ist danach $t_{max}=6a_b/c=6x17.2J=103.2J=3.256\times10^{9}$s.

2. Das Methusalemalter $t_{Meth}=const.\tau_{Meth}^2$ als Tunneleffekt

Damit τ_{Meth} physikalisch realisiert werden kann, ist (i) zu fordern, dass mindestens ein Energieniveau des H-Lyman-Kontinuums (Fig.1) eine so grosse Linienbreite besitzt, dass an der Stelle von $E(\tau_{Meth})$ eine von Null verschiedene Ordinate resultiert. Dies ist für $E(\tau_{min})$ der Fall. (ii) Aus Flussquantisierungs-und Oberflächenspannungsgründen stehen τ_{Meth} und τ_{max} wie beim Kreiszylinderatom im dynamisch stabilen Paar-Mode im Verhältnis $\pi:\tau_{Meth}=\pi\tau_{max}$. Somit wird $t_{Meth}=\pi^2 t_{max}=9.869x99.9=986J$. Das Individualalter des biblischen Methusalem beträgt 969J. Eine andere Methode besteht in der Rückabbildung von $t'_r=$ 10Br.J. (=Brahma-Reifezeit) in g-Rezession. Dies führt auf $t_{Meth}=973J$ (Fig.2).

Literatur

[1] J.T. Muheim, Helv. Phys. Acta 60, 332 (1987).

Helvetica Physica Acta
Vol. 61 (1988)

0018-0238/88/060893-04$1.50+0.20/0

CELLULAR AUTOMATA APPROACH TO NONEQUILIBRIUM CORRELATION FUNCTIONS IN A FLUID

Bastien Chopard * and Michel Droz *
Department of Theoretical Physics
University of Geneva
CH-1211 Geneva 4, Switzerland

Abstract: *Cellular automaton simulations of a simple lattice-gas model with temperature have been performed to compute the spatial correlation functions in a fluid submitted to an external temperature gradient. Numerical results show a quite good qualitative agreement with the predictions of the fluctuating hydrodynamics.*

1.Introduction.

Cellular automata (C.A.) provide an interesting approach to many problems in statistical mechanics. In particular, they are well appropriate to simulate lattice-gas dynamics, where a large number of interacting particles evolve in a discrete space and time. If the interactions between the particles are chosen to conserve mass, momentum and energy, we obtain a simple model for a fluid. Such models have been proposed in order to solve the Navier-Stokes equation [1]. Moreover, a two-speed model on a square lattice has been introduce [2], and proves to reproduce the thermal properties of a fluid at rest.

The question we shall address in this paper is to calculate the spatial correlation functions in a two-dimensional fluid submitted to a temperature gradient. This problem is a difficult one, since it concerns a nonequilibrium system. Indeed, in nonequilibrium statistical mechanics, there is no general frame which provides a tractable approach to such problems. The most common way of calculating correlation functions in a fluid is the generalised fluctuating hydrodynamics of Landau-Lifchitz [3], where one adds random fluxes to the thermo-hydrodynamic equations. Unfortunately, even for simple nonequilibrium cases, one is confronted with great mathematical difficulties and one must appeal to drastic approximations. For this reason, numerical methods are often the most successfull approach [4].

Our purpose in this paper is to show that cellular automata simulations of the two-speed HPP model [2] can also be helpfull for computing these correlation functions . Here, we shall restrict ourself to the density-density, temperature-temperature and density-temperature spatial correlation function in a stationary state.

* Supported by the Swiss National Scientific Foundation

After a brief review of the model in section 2, we present the theoretical form of the *equilibrium* correlation functions, and the results of the numerical simulations for both the equilibrium and nonequilibrium cases.

2. The model

The model consists in fast an slow particles moving on a square lattice. The fast ones travel along the diagonals of the lattice, while the slow ones move along the horizontal and vertical lines. Therefore, the kinetic energy of the fast particles is twice the kinetic energy of the slow ones. The particles interact in such a way that mass energy and momentum are conserved during a collision [2].

On a macroscopic scale, the particle density $\rho(\vec{r},t)$ and velocity field $\vec{u}(\vec{r},t)$ are obtain through the usual definitions of kinetic theory. The temperature $T(\vec{r},t)$ is defined through the mean kinetic energy per particle. It can be shown [2], that this model is descibed by a set of thermo-hydrodynamic equations. For a stationary state with a vanishing macroscopic velocity, these equations reduce to:

$$\nabla p = 0 \qquad \mathrm{div}\vec{J}_Q = 0$$

where $p = k\rho T$ is pressure and $\vec{J}_Q = -\kappa(p,T)\nabla T$ is the heat current. (See reference [2], for more details).

3. Numerical results for the equilibrium and nonequilibrium correlations

Our model has been implemented on a cellular automata machine (CAM-6). We imposed an external temperature gradient by simulating a cold and a hot plate by choosing particular boundary conditions at respectively $z = 0$ and $z = L$. (y and z are the coordinates of the lattice plane.) Thus, we produce temperature gradient along the z-direction. To measure the correlation functions, we divided the area of the system into strips, parallel to the y-axes. The density of particle $\rho(z)$ in a strip at heigt z is obtained by counting the total number of particles into it. In the same way, the temperature $T(z)$ is given by the total kinetic energy, divided by the total number of particles of the strip. These two quantities are time dependent and, in a sationary state, they fluctuate around their mean values. The spatial correlation functions were obtained by averaging over time the products $\rho(z)\rho(z')$, $T(z)T(z')$ and $\rho(z)T(z')$, and then by substracting the respective products of the averages:

$$C_{\rho\rho}(z,z') \equiv < \rho(z,t)\rho(z',t) > - < \rho(z,t) >< \rho(z',t) >$$

$$C_{TT}(z,z') \equiv < T(z,t)T(z',t) > - < T(z,t) >< T(z',t) >$$

$$C_{\rho T}(z,z') \equiv < \rho(z,t)T(z',t) > - < \rho(z,t) >< T(z',t) >$$

The generic form of these correlations is

$$C = \frac{1}{V} f(z)\delta_{z,z'} - g(z,z')$$

where V is the area of the strip.

For the simulations, the strip at height z' is kept fixed at $z' = \frac{L}{2}$ and we measured the correlations for five values of z between 0 and L. For $z = z'$, the temperature-temperature and the density-density correlations both show a pronounced peak, whose height depends of the area of the strips. By varying the area of the strips we can calculate $g(z,z')$ which exibits the long range correlations characteristic of a nonequilibrium system [3,4].

The functions $g(z, \frac{L}{2})$ are shown on the next page, for both an equilibrium (e.i. without the cold and the hot plates) and a nonequilibrium situation. The results of the numerical simulations are marked with a square for the equilibrium and with a circle for the nonequilibrium. These values are compared with theoretical predictions. At equilibrium, a microcanonical hypothesis for the lattice-gas model allows to solve the problem exactly [5]. The functions $g(z,z')$ then express the finite size effects. The horizontal dot lines show the theoretical values of g.

For the nonequilibrium case, we plotted the prediction of the fluctuating hydrodynamics (dashed curves). Although these nonequilibrium calculations did not take into accout the particularity of the lattice-gas model, their predictions agree qualitatively well with the C.A. simulations.

The details of these theoretical derivations will be given elsewhere [5].

4. References

[1] U. Frish, D. d'Humière, B. Hasslacher, P. Lallemand, Y. Pomeau and J.-P. Rivet, in "Modern Approach to Large Non-linear Systems" to appear in J. Stat. Phys.(1987).

[2] B. Chopard and M. Droz, Phys. Lett. A126, 476, (1988).

[3] J. M. Rubi, in "Recent Developements in Nonequilibrium Thermodynamics" , Lecture Notes in Physics, Vol. 253, Springer 1986.

[4] A. L. Garcia, M. Malek Mansour, G. C. Lie, and E. Clementi, Journal of Stat. Phys. 47, 29, (1987).

[4] B. Chopard and M. Droz, in preparation.

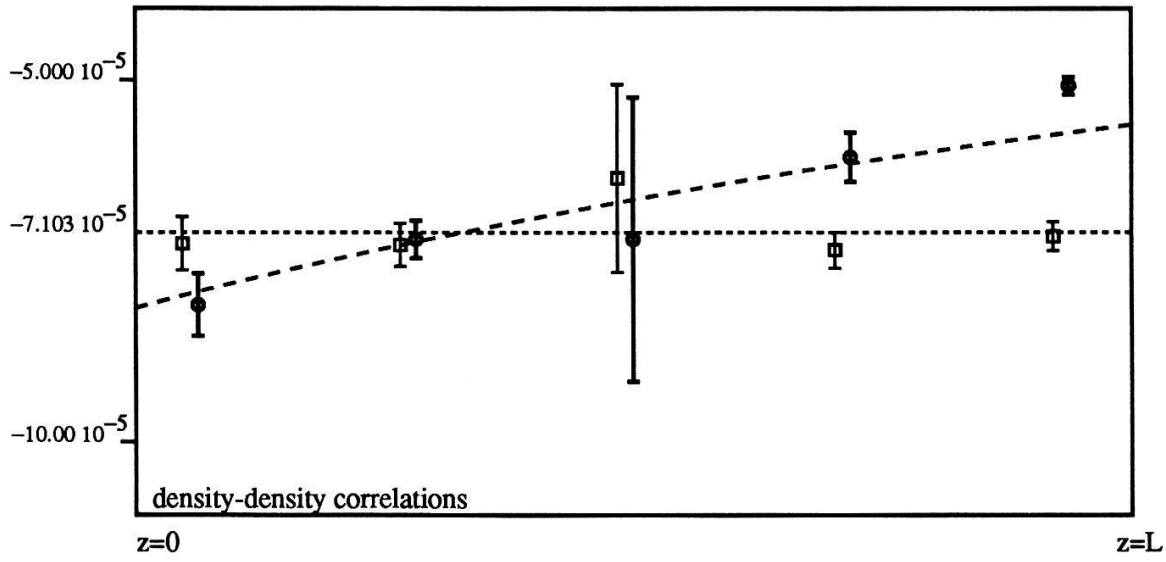
−5.000 10−5
−7.103 10−5
−10.00 10−5
density-density correlations
z=0
z=L

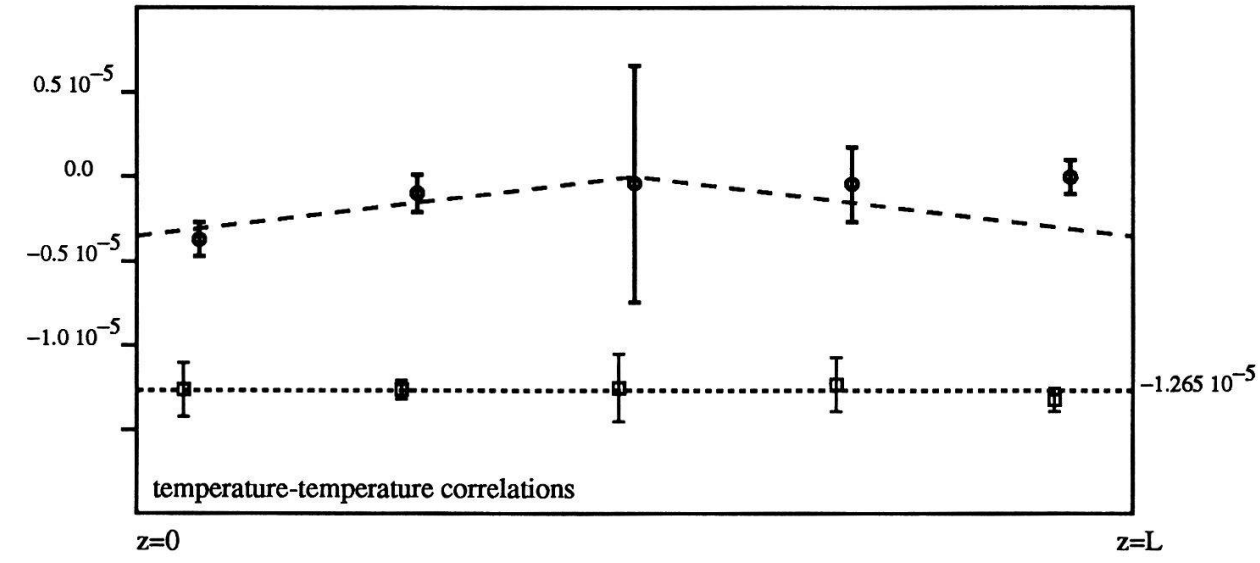
0.5 10−5
0.0
−0.5 10−5
−1.0 10−5
−1.265 10−5
temperature-temperature correlations
z=0
z=L

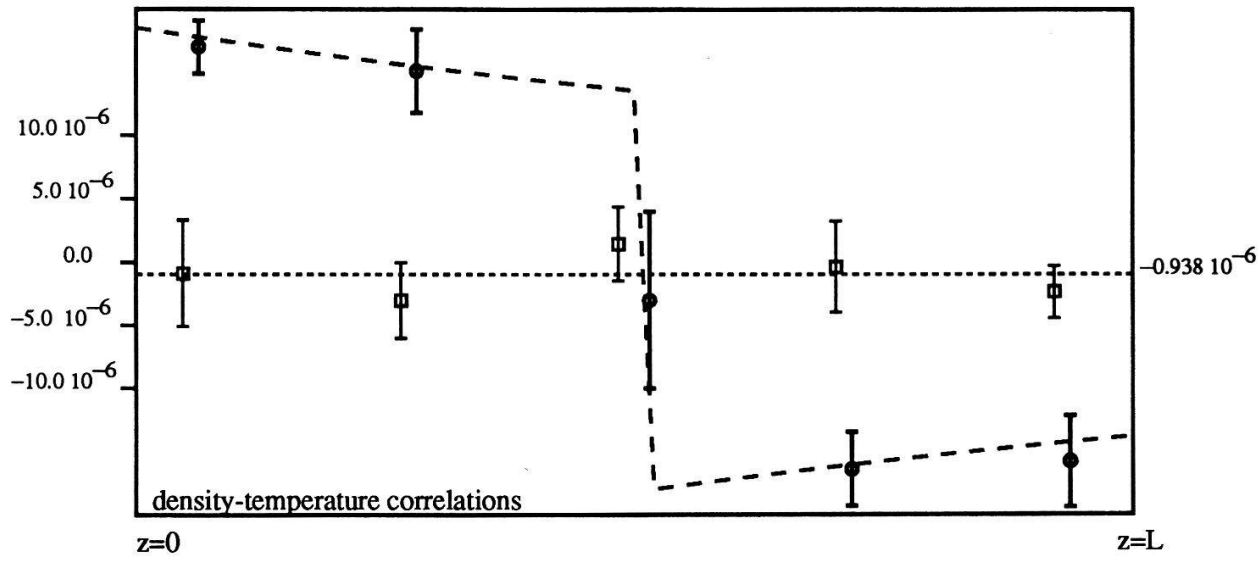
10.0 10−6
5.0 10−6
0.0
−5.0 10−6
−10.0 10−6
−0.938 10−6
density-temperature correlations
z=0
z=L

Helvetica Physica Acta
Vol. 61 (1988)
0018-0238/88/060897-04$1.50+0.20/0

Resonant Stimulation of Nonlinear Damped Oscillators by Poincaré Maps

A. Hübler
Institut für Theoretische Physik und Synergetik, Universität Stuttgart,
D-7000 Stuttgart 80

R. Georgii, M. Kuchler, W. Stelzl, E. Lüscher
Physikdepartment E13, Technische Universität München, D-8046 Garching

Abstract: A new method for resonant stimulation of nonlinear damped oscillators by nonlinear entrainment is presented. Appropriate driving forces are calculated with Poincaré maps. Without using any feedback, these resonant driving forces are in phase with the velocity of the oscillator and cause a huge energy transfer.

1. Introduction

Physical systems with a marked nonlinearity and chaotic solutions can be found in various fields of physics/1/. In general the corresponding differential equations are not integrable/2/. If the dynamics is composed of a smooth oscillation and a comparatively slow modulation of the amplitude of this oscillation, the essential properties of the dynamics can be described by maps, e.g. Poincaré maps and stroboscopic maps/3/. These maps can be much simpler than the differential equation, can easily be solved numerically, and are mathematically well examined/4/. Recently methods have been presented to calculate these maps numerically/5/ and analytically/6/. The aim of this paper is to show, that those maps can be used to stimulate nonlinear oscillators resonantly.
It has been shown analytically /7/ and experimentally/8/ that nonlinear oscillators can be stimulated resonantly by nonlinear entrainment. New experiments with the experimental set up of /8/ show, that a resonant stimulation of the nonlinear oscillator is even possible if a rough approximation of the ideal driving force/7/ is used /9/. This rough approximation is constructed by a smooth interpolation between the extrema of the ideal driving force. The extrema of the driving force can be calculated with a special Poincaré map. The time between the extrema is the recurrence time of the Poincaré map.

2. Resonant stimulation of nonlinear oscillators

As a physical system we consider a damped nonlinear oscillator of the following type:

$$\ddot{y} + \eta_1 \dot{y} + K_1(y) = F(t) \tag{1}$$

where y is the amplitude, η_1 a friction constant, K_1 is a nonlinear force and F(t) represents an external perturbation. We assume that the experimentalist has the following simplified/10/ model of the unperturbed system:

$$\ddot{z} + \eta_1 \dot{z} + K_2(z) = 0 \tag{2}$$

In order to calculate a resonant driving force F(t), the following differential equation has to be numerically integrated:

$$\ddot{x} + \eta_2 \dot{x} + K_2(x) = 0 \tag{3}$$

According to /7/ the perturbation

$$F(t) = -2 \eta_2 \dot{x} \tag{4}$$

is resonant for $\eta_2 = -\eta_1$, i.e. (3) results from (2) by a reflection of time, and for $K_2 = K_1$, i.e. the model is exact. Since y(t)=x(t) is a special solution of (1),

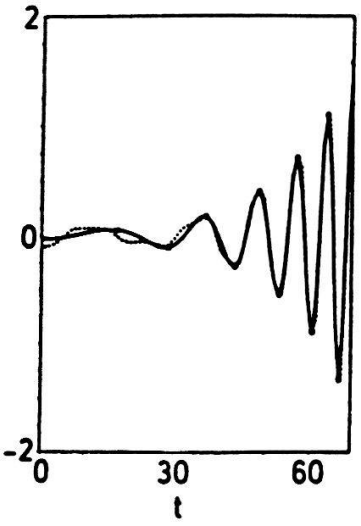

Table 1 Coefficients $c_{1,i}$ and $c_{2,i}$

i	$c_{1,i}$	$c_{2,i}$
0	-0.01	1.2
1	0.53	-0.52
2	0.71	-0.018
3	-0.71	-0.040
4	0.35	-0.016
5	-0.06	-0.002

Fig.1 Resonant stimulation of the oscillator $\ddot{y} + 0.1 \dot{y} + y^3 = 0$ with an approximation F'(t) of the resonant driving force F(t). Plotted is $\dot{y}(t)$ (dotted line) and F'(t)/0.2 (straight line). The energy transfer is large, because $\dot{y}(t)$ and F'(t) are in phase. F'(t) is calculated by a numerical spline interpolating between the extremas of F(t). The extremas are calculated by an backward iteration of the Poincaré map $P_{\dot{y}}$. The Poincaré map $P_{\dot{y}}$ and the recurrence time T are numerically approximated with
$P_{\dot{y}} : \dot{y}_{n+1} = (-1)^n \sum_{i=1}^{5} c_{1,i} |\dot{y}_n|^i$, $T_n = \exp(\sum_{i=1}^{5} c_{2,i} (\log|\dot{y}_n|)^i)$. The coefficients $c_{1,i}$ and $c_{2,i}$ are listed in table 1.

(3) is called aim differential equation. When the dynamics of the unperturbed experimental system y(t) and the dynamics of the aim equation x(t) are represented in a phase space/3/ the corresponding trajectories have the same geometry. If the dynamics of the unperturbed experimental system is composed of a smooth oscillation and a comparatively slow modulation of the amplitude of this oscillation, the resonant driving force F(t) has the same property, because of (4). In this case, the dynamics of the unperturbed experimental system, aim differental equation, and the resonant driving force can be approximated by an interpolation scheme based on the extrema $\dot{y}_n$, $\dot{x}_n$, and F_n of the velocity $\dot{y}(t)$, $\dot{x}(t)$, and the driving force F(t). The extrema $\dot{y}_n$, $\dot{x}_n$, and F_n are calculated by the Poincaré maps $P_{\dot{y}}$, $P_{\dot{x}}$ and P_F. The time between the extrema is the recurrence time $T(\dot{y}_n)$. The Poincaré map of the extrema of the resonant driving force P_F is proportional (4) to the backward iteration of $P_{\dot{y}}$, if $P_{\dot{y}}$ is invertible. Otherwise P_F can be calculated from $P_{\dot{x}}$ using (4). There are some analytical and numerical methodes to estimate $P_{\dot{x}}$, $P_{\dot{y}}$, and T/5,6/(fig.1).

The resonant driving process is stable, if

$$\ddot{\varepsilon} + \eta_1 \dot{\varepsilon} + \frac{dK_1}{dy}\Big|_{x(t)} \varepsilon = F'(t) - F(t) \qquad (5)$$

is asymptotically stable, where F'(t) is the approximated resonant driving force and $\varepsilon = y(t) - x(t) \approx 0$.

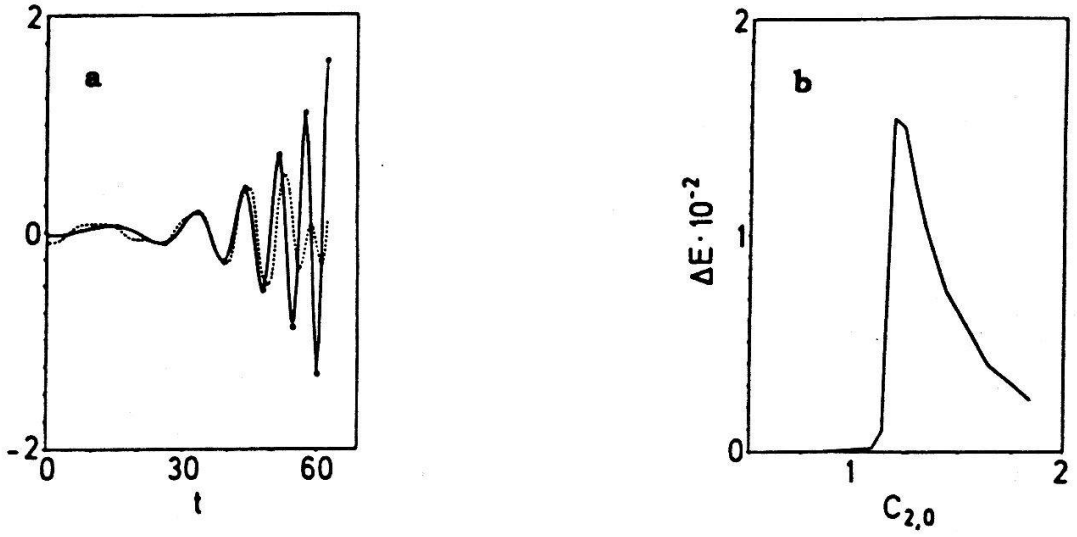

Fig.2 Estimation of a Poincaré map by resonance spectroscopy. (a): If the parameter $c_{2,0}$ of the Poincaré map (Tab.1) is equal to 1.0 no resonant stimulation of the system $\ddot{y} + 0.1\,\dot{y} + y^3 = 0$ is possible. Plotted is $\dot{y}(t)$ (dotted line), $\dot{y}_n$ (o) and F'(t)/0.2 (straight line). $\dot{y}(t)$ and F'(t) are out of phase. (b): The energy ΔE of the same oscillator after ten oscillations of the driving force is largest if $c_{2,0}$ has the value of table 1. The numerical simulations show, that only for this parameter value the resonance condition $\dot{y}(t) \sim F'(t)$ is satisfied.

3. Resonance Spectroscopy with Poincaré maps

If the paramters of the model or the parameters of the Poincaré map P_y are wrong, generally no resonant stimulation is possible/7/. The Poincaré map can be estimated by a systematic variation of the parameters(fig.2).

4. Conclusion

The generalisation of the above techniques to systems of differential equations, and partial differential equations is straightforward/8,11,12/, and its application to controlling/8,11,12/ Navier-Stokes flows or certain equations of biology might have important consequences.

We like to thank H.Haken, W. Kroy, W.Altmann, O. Wohofsky, P.Meinke, H.Hayd, M.Maurer, and Ch. Berding for continuous support.

References

/1/ H.L.Swinney, Physica **7D**, 3(1983)

/2/ G.Eilenberger, in Nichtlineare Dynamik in kondensierter Materie, ed. G.Eilenberger, H. Müller-Krumbhaar (KFA-Jülich, D-Jülich, 1985)

/3/ J.Guckenheimer, P. Holmes, Nonlinear Oscillations, Dynamical Systems and Bifurcating Vector Fields (Springer, New York 1983), chapt. 4, J.P.Eckmann, D.Ruelle, Rev.Mod.Phys. **57**, 617(1985)

/4/ P.Collet, J.P.Eckmann, Iterated Maps of the Interval as Dynamical Systems(Birkhäuser, Boston 1980)

/5/ W.Eberl, M.Kuchler, A.Hübler, E.Lüscher, M.Maurer, P.Meinke, Z.f.Physik B**68**, 253(1987), M.Kuchler, W.Eberl, A.Hübler, E.Lüscher, H.P.A. **61**, 232(1988)

/6/ R.Wackerbauer, W.Eberl, A.Hübler, E.Lüscher, H.P.A. **61**, 236(1988)

/7/ G.Reiser, A.Hübler, E.Lüscher, Z.f.Naturforsch. **42a**, 803(1987)

/8/ C.Wagner, W.Stelzel, A.Hübler, E.Lüscher, H.P.A. **61**, 228(1988)

/9/ R.Goergii, W.Stelzel, A.Hübler, E.Lüscher, Symposium Synergetik, Tagungsband der DPG Jahrestagung 1988 in Karlsruhe

/10/ H.Haken, Synergetics, An Introduction (Springer, Berlin 1983) chapt.7

/11/ A.Hübler, Beschreibung und Steuerung nichtlinearer Systeme, Promotionsschrift, Physikdepartment der Technischen Universität München, 1987, Kapitel 2

/12/ J.Merten, B.Wohlmuth, A.Hübler, E.Lüscher, H.P.A. **61**, 88(1988)

Helvetica Physica Acta
Vol. 61 (1988)

0018-0238/88/060901-04$1.50+0.20/0

Creation-annihilation operators for the Hydrogen atom and related potentials

H.R. Jauslin, Dept. Physique Théorique, Université de Genève,
CH-1211 Genève 4, Switzerland

Abstract: Using ideas of supersymmetric quantum mechanics we construct creation and annihilation operators for a class of Schrödinger operators. This allows to determine the eigenvalues and eigenfunctions by algebraic methods, in analogy to the well-known procedure for the harmonic oscillator.

1) We consider the radial Schrödinger operator

$$H = -\frac{1}{r}\,\frac{d^2}{dr^2}\,r + V_-(r) \tag{1}$$

which we assume has a ground-state with eigenvalue E_0, that one can represent as $\varphi_0(r) \equiv 1/r\,\exp(-W)$. We denote its eigenvalues by E_n. From supersymmetric quantum mechanics one knows[1,2] that one can represent $H_- \doteq H - E_0$ as

$$H_- = A^\dagger A \tag{2}$$

with

$$\begin{aligned} A &= \varphi_0\,\frac{d}{dr}\,\varphi_0^{-1} \equiv \frac{1}{r}\,\frac{d}{dr}\,r + W' \\ A^\dagger &= -\varphi_0^{-1}\frac{1}{r^2}\,\frac{d}{dr}\,r^2\,\varphi_0 \equiv -\frac{1}{r}\,\frac{d}{dr}\,r + W' \end{aligned} \tag{3}$$

where primes denote derivatives. Notice that $A^\dagger$ is the adjoint of A with respect to the scalar product corresponding to the radial equation: $\langle\varphi,\psi\rangle \doteq \int_0^\infty dr\,r^2\varphi^*(r)\psi(r)$. For the calculation it is enough to note that $(\frac{d}{dr})^\dagger \neq -\frac{d}{dr}$ but $(\frac{1}{r}\frac{d}{dr}r)^\dagger = -\frac{1}{r}\frac{d}{dr}r$. We remark that the lowest eigenvalue is equal to zero by construction. One sees from (3) that the explicit factorization (2) is equivalent to the knowledge of the ground-state of the model.

The main ingredient of supersymmetric quantum mechanics is to define a new operator by $H_+ \doteq AA^\dagger$ (Darboux-Crum transformation). H_+ is called the supersymmetric partner of H_-. H_- and H_+ can be written as

$$H_\mp = -\frac{1}{r}\,\frac{d^2}{dr^2}\,r + (W')^2 \mp W'' \tag{4}$$

The spectrum of H_+ is equal to the one of H_- but without the lowest eigenvalue ($= 0$). The normalized n^{th} eigenfunction $\varphi_{(+),n}$ of H_+ is related to $\varphi_{(-),n+1}$, the $(n+1)^{st}$ one of H_- by

$$\begin{aligned} \varphi_{(-),n+1} &= (E_{n+1} - E_0)^{-1/2}\,A^\dagger\,\varphi_{(+),n} \\ \varphi_{(+),n} &= (E_{n+1} - E_0)^{-1/2}\,A\,\varphi_{(-),n+1} \end{aligned} \tag{5}$$

We remark that $\varphi_{(-),n+1}$ and $\varphi_{(+),n}$ correspond both to the eigenvalue E_{n+1}. (The notation differs from Ref.[2].)

2) We define now a special class of operators: Consider a family of operators $H_-(\alpha)$ depending on s parameters $\alpha \equiv (\alpha_1, \ldots, \alpha_s)$, such that the partners $H_+(\alpha)$ are of the same form but for different parameters $\alpha^{(1)}$:

$$H_+(\alpha) = H_-(\alpha^{(1)}) + c(\alpha^{(1)}) \tag{6}$$

where $c(\alpha^{(1)})$ is a constant and $\alpha^{(1)}$ depends in some well-defined way on α: $\alpha^{(1)} = f(\alpha)$. This class includes among many others[3,4] the radial operator of the Hydrogen atom.

3) We construct the following sequence of operators[3]:

$$H^{(n)} \doteq H_-(\alpha^{(n)}) + \sum_{k=0}^{n} c(\alpha^{(k)}) \tag{7}$$

where $\alpha^{(n)} \doteq f(\alpha^{(n-1)}) = f^n(\alpha) \equiv f \circ \ldots \circ f\ (\alpha)$; $\alpha^{(0)} = \alpha$ and $c(\alpha^{(0)}) = E_0$. We remark that

$$\begin{aligned} H^{(n+1)} &= H_-(\alpha^{(n+1)}) + c(\alpha^{(n+1)}) + \sum_{k=0}^{n} c(\alpha^{(k)}) \\ &= H_+(\alpha^{(n)}) + \sum_{k=0}^{n} c(\alpha^{(k)}) \end{aligned} \tag{8}$$

which implies that the spectrum of $H^{(n+1)}$ is the same as the one of $H^{(n)}$ but without the lowest eigenvalue. By iteration we obtain that: 0th eigenvalue of $H^{(n+1)}$ = 1st eigenvalue of $H^{(n)} = \ldots =$ (n+1)st eigenvalue of $H^{(0)} \equiv H$. Since the lowest eigenvalue of $H_-(\alpha^{(j)})$ is always zero, this implies[3]

$$E_n = \sum_{k=0}^{n} c(\alpha^{(k)}) \tag{9}$$

4) For the calculation of the eigenfunctions we proceed as follows: Let $\varphi^{(\alpha)}_{(-),n}$ and $\varphi^{(\alpha)}_{(+),n}$ be the normalized eigenfunctions of $H_-(\alpha)$ and $H_+(\alpha)$ respectively. Relation (6) implies

$$\varphi^{(\alpha)}_{(+),n} = \varphi^{(f(\alpha))}_{(-),n} \tag{10}$$

which combined with (5) gives

$$\begin{aligned} \varphi^{(\alpha)}_{(-),n+1} &= (E_{n+1} - E_0)^{-1/2} A^{\dagger}_{\alpha}\ \varphi^{(\alpha)}_{(+),n} \\ &= (E_{n+1} - E_0)^{-1/2} A^{\dagger}_{\alpha}\ \varphi^{(f(\alpha))}_{(-),n} \end{aligned} \tag{11}$$

If we define an isometric operator U by its action on the basis vectors:

$$U\varphi^{(\alpha)}_{(-),n} \doteq \varphi^{(f(\alpha))}_{(-),n} \tag{12}$$

we can rewrite (11) as

$$\varphi^{(\alpha)}_{(-),n+1} = (E_{n+1} - E_0)^{-1/2} A^\dagger_\alpha U \; \varphi^{(\alpha)}_{(-),n} \tag{13}$$

and therefore

$$\varphi^{(\alpha)}_{(-),n} = \nu_n \left(A^\dagger_\alpha U\right)^n \varphi^{(\alpha)}_{(-),0} \tag{14}$$

where $\nu_n = \prod_{k=1}^n (E_k - E_0)^{-1/2}$ is the normalization. This expression defines the creation operator $a^\dagger$ for the original problem. The annihilation operator a is constructed along the same arguments:

$$a^\dagger \equiv A^\dagger_\alpha U \quad , \qquad a \equiv U^{-1} A_\alpha \tag{15}$$

For the explicit calculation of the eigenfunctions we can rewrite (14) as

$$\begin{aligned} \varphi^{(\alpha)}_{(-),n} &= \nu_n \; A^\dagger_\alpha U \ldots A^\dagger_\alpha U \varphi^{(\alpha)}_{(-),0} \\ &= \nu_n A^\dagger_\alpha A^\dagger_{f(\alpha)} A^\dagger_{f^2(\alpha)} \cdots A^\dagger_{f^{n-1}(\alpha)} \varphi^{(f^n(\alpha))}_{(-),0} \end{aligned} \tag{16}$$

This formula shows that the knowledge of the ground-state $\varphi^{(f^n(\alpha))}_{(-),0}$ for the family of parameters $f^n(\alpha)$, $n = 0, 1, \ldots$ suffices to determine all eigenfunctions.

Application to the Hydrogen atom

We can apply now the preceding method to the radial operator for the Hydrogen atom:

$$H = -\frac{1}{r}\frac{d^2}{dr^2} r + \frac{l(l+1)}{r^2} - \frac{2\gamma}{r} \qquad\qquad l = 0, 1, \ldots \tag{17}$$

1) We first verify by insertion that H can be factorized as (2),(3) with

$$\begin{aligned} E_0 &= -\gamma^2/(l+1)^2 \\ W' &= \frac{\gamma}{l+1} - \frac{l+1}{r} \end{aligned} \tag{18}$$

We identify l with α. Eq. (18) is equivalent to the statement that the ground-state is

$$\varphi^{(l)}_{(-),0} = \frac{1}{r}\, e^{-W} = \left(\frac{2\gamma}{l+1}\right)^{l+3/2} ([2l+2]!)^{-1/2} \; r^l \, e^{-\gamma r/(l+1)} \tag{19}$$

2) We verify that H belongs to the class defined by (6):

$$\begin{aligned} H_+(l) &= -\frac{1}{r}\frac{d^2}{dr^2}r + \frac{(l+1)(l+2)}{r^2} - \frac{2\gamma}{r} + \frac{\gamma^2}{(l+1)^2} \\ &= H_-(l+1) - \frac{\gamma^2}{(l+2)^2} + \frac{\gamma^2}{(l+1)^2} \end{aligned} \tag{20}$$

We identify $\alpha^{(1)} \equiv f(\alpha) = l+1$, i.e. $\alpha^{(k)} = l+k$; and thus

$$\begin{aligned} c(\alpha^{(1)}) &= -\frac{\gamma^2}{(l+2)^2} + \frac{\gamma^2}{(l+1)^2} = -\frac{\gamma^2}{(\alpha^{(1)}+1)^2} + \frac{\gamma^2}{(\alpha^{(1)})^2} \\ \text{and} \qquad c(\alpha^{(k)}) &= -\frac{\gamma^2}{(l+k+1)^2} + \frac{\gamma^2}{(l+k)^2} \end{aligned} \tag{21}$$

3) Inserted into (9) we obtain the eigenvalues

$$E_n = \sum_{k=0}^{n} c(\alpha^{(k)}) = -\frac{\gamma^2}{(l+n+1)^2} \tag{22}$$

4) The eigenfunctions are given by Eq.(16) with

$$\begin{aligned} \varphi_{(-),0}^{(f^n(\alpha))} &= \left(\frac{2\gamma}{l+n+1}\right)^{l+n+3/2} ([2l+2n+2]!)^{-1/2} \; r^{l+n} \; \mathrm{e}^{-\gamma r/(l+n+1)} \\ A^{\dagger}_{fj(l)} &= -\frac{1}{r}\,\frac{d}{dr}\,r + \frac{\gamma}{l+j+1} - \frac{l+j+1}{r} \end{aligned} \tag{23}$$

One can verify that this leads to the usual expressions involving Laguerre polynomials.

References:

[1] P.A.Deift, Duke Math. J. **45** (1978) 267.
[2] H.R. Jauslin, J. Phys. **A 21** (1988) to be published.
[3] L.E. Gendenshtein, JETP Lett. **38** (1983) 356.
[4] L. Infeld, T.E. Hull, Rev. Mod. Phys. **23** (1951) 21.